Study on Failure Mechanisms of Tufted Composite Laminates under Tensile Loading

by

Sobhan ESMAEILI MARZDASHTI

THESIS PRESENTED TO ÉCOLE DE
TECHNOLOGIE SUPÉRIEURE IN PARTIAL FULFILLMENT OF THE
REQUIREMENTS FOR THE DEGREE OF MASTER IN MECHANICAL
ENGINEERING
M.A.Sc.

MONTREAL, AUG 31st, 2023

ÉCOLE DE TECHNOLOGIE SUPÉRIEURE
UNIVERSITÉ DU QUÉBEC

BOARD OF EXAMINERS

THIS THESIS HAS BEEN EVALUATED

BY THE FOLLOWING BOARD OF EXAMINERS

Professor Simon Joncas, Thesis Supervisor
System Engineering Department, École de technologie supérieure

Professor Martine Dubé, President of the Board of Examiners
Mechanical Engineering Department, École de technologie supérieure

Professor Philippe Causse, Member of the jury
System Engineering Department, École de technologie supérieure

THIS THESIS WAS PRESENTED AND DEFENDED

IN THE PRESENCE OF A BOARD OF EXAMINERS AND PUBLIC

ON AUGUST 15th, 2023

AT ÉCOLE DE TECHNOLOGIE SUPÉRIEURE

ACKNOWLEDGMENT

Étude sur les mécanismes de défaillance des stratifiés composites touffetés sous chargement en traction

Sobhan ESMAEILI MARZDASHTI

RESUME

Les matériaux composites en polymère renforcé de fibres (FRP) multicouches sont connus pour leur excellente rigidité et résistance dans le plan, mais ils présentent une faiblesse en matière de délamination, en particulier dans des conditions de charge de traction transversale. Pour remédier à ce problème, des techniques de renforcement dans l'épaisseur des composites par des touffes peuvent être utilisées pour améliorer la résistance à la délamination des composites multicouches. Les techniques de touffetage ont gagné en popularité parmi les ingénieurs en raison de leur capacité à améliorer à la fois les propriétés dans le plan et hors plan à un coût inférieur par rapport à d'autres techniques de renforcement en travers (TTR). L'objectif initial de cette étude est la production de stratifiés tuftés, en tenant compte de différentes géométries de touffetage et de séquences de stratifiés avec un film de décollement complet placé dans la couche intermédiaire des stratifiés. Pour analyser l'impact des boucles de touffetage sur le comportement des stratifiés sous tension, deux types de stratifiés sont fabriqués : des stratifiés sans boucles et des stratifiés avec boucles contenant une seule touffe. Les stratifiés sans boucles sont créés en fraisant les stratifiés avec boucles. De plus, cette étude utilise deux séquences de stratifiés quasi-isotropes et orthotropes pour étudier comment le stratifié préformé affecte le mécanisme de défaillance des stratifiés touffetés exposés à une charge hors plan. Pour acquérir une compréhension plus approfondie des modes de rupture présentés dans les laminés touffetés avec différentes géométries de touffes et séquences de stratification, la technique de CT-scan est utilisée de manière progressive pendant la sollicitation en traction. Cette technique met en évidence une observation et une analyse détaillées des dommages internes et des modes de défaillance des stratifiés à différents déplacements de traction.

Après avoir analysé les courbes de force-séparation et les surfaces de rupture, il a été constaté que, pour des séquences constantes, la géométrie de touffe sans boucle échoue en raison de l'arrachement des touffes et possède une énergie de rupture plus élevée par rapport à la géométrie standard (avec boucle). Néanmoins, les stratifiés avec boucles démontrent une charge ultime plus élevée que ceux sans boucle. Selon les courbes de force-séparation, la touffe présente un comportement plus fragile dans le stratifié quasi-isotrope que dans le stratifié orthotrope. Indépendamment de la géométrie de la touffe, le passage des séquences de stratification orthotropes à quasi-isotropes entraîne une augmentation de 60% de la charge ultime et une réduction de 62% de l'énergie de rupture. L'analyse CT-scan indique que les modes de défaillance primaires pendant le régime linéaire sont le déliantage inter-fibre et la rupture de l'interface. Cependant, pendant le régime plastique, la défaillance de l'interface, la rupture de touffe, la défaillance de touffe et l'arrachement sont observés. La quantité de résine entourant une touffe peut avoir un impact considérable sur ses propriétés sous charge de traction. S'il y a une quantité limitée de résine entourant la touffe et que la touffe est fermement collée au stratifié, alors une défaillance de la touffe au niveau du plan médian est susceptible

VIII

de se produire. À l'inverse, une plus grande quantité de résine entourant la touffe tend à favoriser l'arrachement des fibres qui composent la touffe. Enfin, un outil de modélisation microscopique de dommages en 3D fiable a été développé dans Abaqus pour prédire les modes de défaillance des composites orthotropes touffetés. Les critères de dommage Hashin pour la touffe et la réponse élastoplastique de l'interface au renfort sont intégrés dans la modélisation en utilisant l'outil de plasticité d'Abaqus et la méthode du champ défini par l'utilisateur (USDFLD). Malgré un problème de convergence qui empêche l'analyse non linéaire d'atteindre une défaillance complète, il a été observé que les propriétés des matériaux sélectionnés et les outils utilisés ont démontré une grande efficacité pour simuler de façon précise le comportement d'un composite touffeté lors de la phase initiale d'un test de traction.

Mots clés : Touffetage, Stratifiés composites touffetés, Mécanismes de défaillance, Analyse CT-scan, Modélisation par éléments finis (MEF)

Study on Failure Mechanisms of Tufted Composite Laminates Under Tensile Loading

Sobhan ESMAEILI MARZDASHTI

ABSTRACT

Layered fiber reinforced polymer (FRP) composite materials are known for their excellent in-plane stiffness and strength, but they have a weakness in delamination, particularly when exposed to transverse loading. To address this issue, through-thickness reinforcement (TTR) techniques can be utilized to enhance the delamination resistance of layered composites. Tufting techniques have gained popularity among engineers due to their ability to improve out-of-plane properties at a lower cost compared to other through-thickness reinforcement (TTR) techniques. The initial focus of this study is on the production of tufted laminates, considering different tufting geometries and laminate sequences with a full release film placed in the mid-layer of laminates. To analyze the impact of tufting loops on the behavior of laminates under transvers loading, two types of laminates are manufactured: loop-less and with-loop laminates that contain a single tuft. The loop-less laminates are created by milling down the surface of laminates. Additionally, this study employs two laminate sequences (quasi-isotropic and orthotropic) to investigate how preform layering affects the failure mechanisms of tufted laminates exposed to transverse loading. To gain a deeper understanding of the failure modes present within tufted laminates of varying tufting geometries and laminate sequences, the CT-scan technique is utilized incrementally during pure tensile transvers loading. This technique highlights detailed observation and analysis of the internal damage and failure modes of laminates at different tensile displacements.

Upon analyzing the force-separation curves and fracture surfaces, it is found that for either laminate sequence, the loop-less tufting geometry fails due to tuft pull-out and possesses higher fracture energy in comparison to the standard tuft (with-loop) geometry. Nonetheless, with-loop tuft laminates demonstrate a higher ultimate load than loop-less ones. According to the force-separation curves, the tuft exhibits a more brittle behavior in the quasi-isotropic laminate than in the orthotropic one. For both tufting geometries, switching the laminate sequences from orthotropic to quasi-isotropic leads to a 60% rise in the ultimate load and a 62% reduction in fracture energy. CT-scan analysis indicates that the primary failure modes during the linear regime are inter-fiber and interface debonding. However, during the plastic regime, interface failure, tuft rupturing, and pullout are observed. The quantity of resin surrounding a tuft can greatly impact its properties under tensile loading. Since there is a limited quantity of resin surrounding the tuft and the tuft is in contact with laminate, then tuft failure at the mid-plane is likely to occur. Conversely, a larger amount of resin surrounding the tuft tends to promote fiber pull-out instead. Lastly, a reliable 3D damage micro modelling tool has been developed in Abaqus for predicting the failure modes of orthotropic with-loop tufted laminates. The Hashin damage criteria for the tuft and elastoplastic respond for the tuft interface are incorporated into the model using Abacus plasticity tool and the user-defined field (USDFLD) method. Despite a convergence issue preventing the model to reach full failure, it has been observed that the selected material properties and tools have demonstrated high effectiveness

X

in accurately simulating the behavior of a tufted laminate during the initial stage of a tensile test.

LIST OF TABLES

LIST OF FIGURES

Page

LIST OF ABREVIATIONS

CNC	Computer Numerical Control
CT	Computed Tomography Scan
C3D8R	Eight-Node Brick Element with Reduced Integration
DCB	Double Cantilever Beam
ERR	Energy Release Rate
FEM	Finite Element Method
GFRP	Glass Fiber Reinforced Polymer
LLSS	Interlaminar Shear Strength
KSL	Keilmann Sondermaschinenbau Gmbh
Loop-Less	Tufting Loop Cut-off
MCC	Modified Compliance Calibration
M-ortho	Milled Down Tufted Orthotropic Laminate
M-iso	Milled Down Tufted Quasi-Isotropic Laminate
S-ortho	Standard Tufted Orthotropic Laminate
S-iso	Standard Tufted Quasi-Isotropic Laminate
SDV	State Dependent Variable
TTR	Through the Thickness Reinforcement
USDFLD	User Defined Field
PMMA	Polymethyl Methacrylate
With-Loop	Tufted Laminate with Loop
5SQ	5mm Squared

XX

5SQM	Milled-Down 5mm Squared
4SQ	4mm Squared
4SQM	Milled-Down 4mm Squared
5ST	5mm Staggered
5STM	Milled-Down 5mm Staggered

INTRODUCTION

0.1 General introduction of composite materials

Composite materials were developed in the mid-20th century, thanks to advancements in materials science and manufacturing techniques. The main users of composites are the aerospace, defense, automotive and construction industries. This is due to their numerous advantageous features, such as being lightweight, having high strength and stiffness, good resistance to fatigue and corrosion. Additionally, using composite materials can have positive outcomes by facilitating the production of parts with complex shapes while minimizing the need for numerous components. As a result, this can lead to cost reductions compared to using traditional metal materials

Moreover, composite materials can be manufactured using sustainable and environmentally friendly processes, making them an eco-friendlier option than conventional materials [Soung Van, 2009]. Besides, the ability to mold composites into complex shapes allows for greater design freedom, which is especially important in different industries. Composites are typically composed of different materials known as constituent materials. These constituent materials fall into two main categories: matrix or binder, and reinforcement. Both types are necessary to create a composite material. The matrix material serves to surround and support the reinforcement, which plays a significant role in improving the mechanical and physical properties. Designers have the flexibility to choose the most suitable combination of matrix and reinforcement materials for specific applications.

0.2 Through the thickness reinforcement (TTR) composite laminates

Behind all of the benefits that composite materials can bring for different industries, they are also known for their low resistance, reliability, and strength through the thickness when subjected to special loadings such as impact and out-of-plane loadings. To enhance the ability of composite materials to withstand these loads, researchers are actively exploring the

development of 3D preforms. The TTR preforms consist of interconnected reinforcement enhancing the strength and stiffness of a material in the thickness direction. TTR techniques can improve the resistance of composite materials to a variety of stresses, making them more dependable and efficient for a wide range of applications. Ongoing advancements in materials science and manufacturing processes have led to the development of more advanced TTR techniques such as Z-pinning, stitching, tufting and 3D weaving, which are continuously being improved and studied for a range of applications across various industries.

0.2.1   3D Weaving

3D weaving is a well-established and widely adopted technique for manufacturing composite materials with enhanced mechanical properties and design flexibility. 3D fabrics consist of multiple 2D layers that are connected together using binder threads in the Z direction. While this is a common way of creating 3D fabrics, there have been several studies that have focused on exploring the classification and shape of these woven structures (Chen, Taylor, & Tsai, 2011; Bilisik, 2011). Different weaving architectures have also been developed to determine the best interlacing and orientation of the yarns within the structure, as well as the weaving pattern, to optimize the strength and performance of 3D fabrics.

The different types of 3D fabric architectures include 3D orthogonal weave, 3D layer-to-layer interlock weave, and 3D through-thickness angle interlock are illustrated in Figure 0.1. These architectures are used to add strength and durability to composite materials in different ways. One advantage of this process is that it allows for flexibility in controlling the number of binder yarns in the fiber architectures, making it possible to create fabrics with varying properties for different applications (Ansar, Xinwei, & Chouwei, 2011). The use of 3D woven techniques in composite materials has some drawbacks. Firstly, it is a complex and expensive process that requires specialized equipment and skilled labor. Secondly, the mechanical properties of 3D woven composites can be more variable compared to other manufacturing techniques due to the intricate weave pattern, which may makes it difficult to predict their performance under certain conditions. Finally, the design flexibility of 3D woven composites may be limited because the weave pattern can constrain the shape and size of the final product.
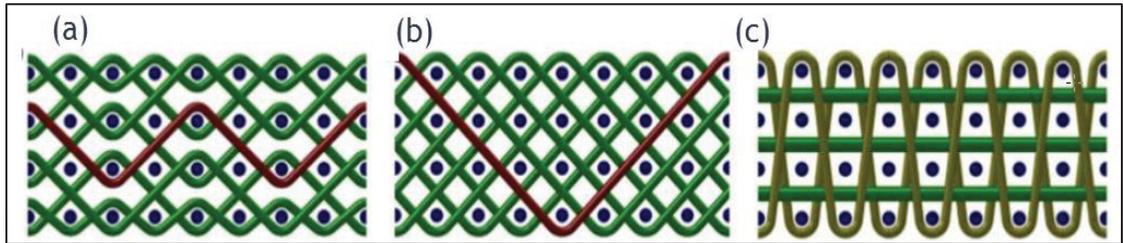
Figure 0.1 3D woven architectures: (a) layer-to-layer angle interlock, (b) through-the-thickness angle interlock, (c) orthogonal interlock taken from Gnaba et al. (2017)

0.2.2   Z-pinning

Z-pinning technology involves the insertion of rigid rods, commonly known as "pins," in the Z-direction. These pins are typically made of materials with high stiffness and strength, such as carbon, titanium, or steel, and range in diameter from 0.2 to 1mm (Mouritz, 2007). Figure 0.2 demonstrates the process of reinforcement, which involves inserting pins through the thickness of the material (Mouritz, 2007). This technique is commonly recognized as a dependable and uncomplicated mean of reinforcing both dry and prepreg composite materials. To insert the pins, a foam material containing the Z-pins is first placed above the preform or prepreg. The Z-pins are then inserted through the thickness of the preform by using an ultrasonic hammer to sweep the upper face of the foam, which holds the pins securely in place during the process. The location of the pins is determined based on the specific application and requirements of the composite material in different industries.

Z-pinning technique enhances the damage tolerance and impact resistance of composite materials by boosting the delamination toughness and joint strength (Cartié, Troulis, & Partridge, 2006). This is achieved through the insertion of stiff and straight pins that reinforce the composite structure and prevent crack propagation between the layers. However, using oversized pins can result in resin-rich pockets and bubbles in the laminates, which can lower the in-plane strength and stiffness properties (Mouritz, 2007; Tong, Mouritz, & Bannister, 2002). When using the Z-pinning technique, it is crucial to carefully consider the size of the pins and their insertion positions. Furthermore, this process is known to add complexity and

increase production costs due to the need for additional equipment and labor to insert the pins into the composite structure resulting in higher production costs.
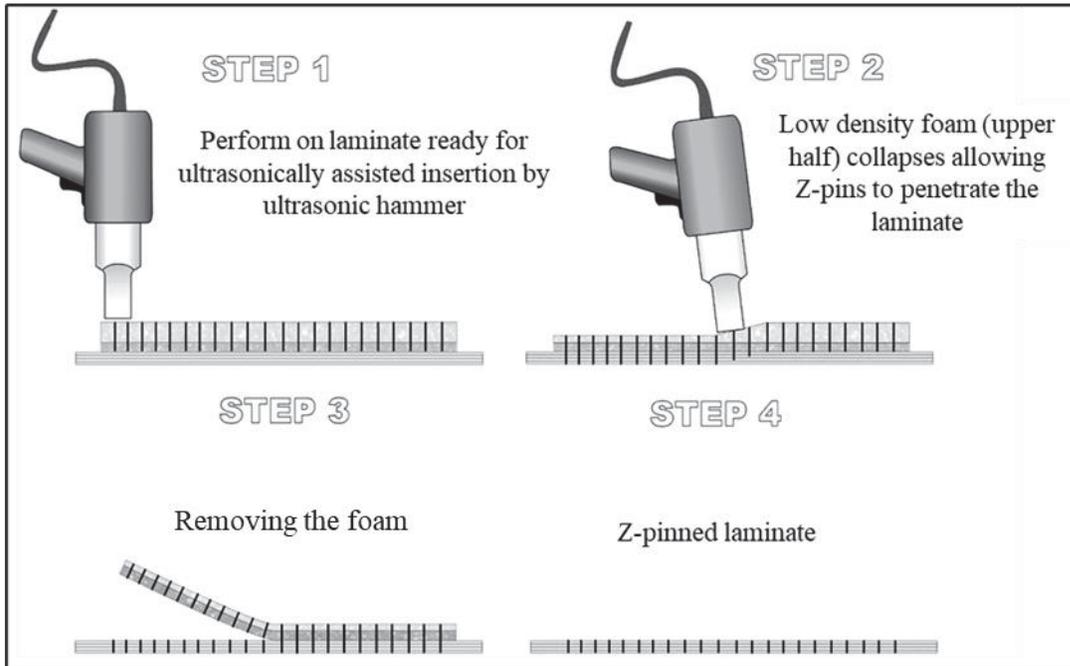
Figure 0.2 Major stages in the insertion of z-pins into uncured composite material taken from Mouritz1et al. (2011)

0.2.3   Stitching

Stitching has become a widely accepted method in several industries, including aerospace, automotive, and sports, for improving the interlaminar fracture toughness, fatigue and impact damage resistance (Dransfield, Baillie, & Mai, 1994; Aymerich, Priolo, & Sun, 2003). By implementing the stitching method, which involves using a strong thread through the thickness of the laminates, it became possible to create 3-D composites with fewer issues related to complexity and cost, providing benefits for both manufacturers and engineers. The stitching method involves sewing high tensile strength yarn through dry fabric plies using an industrial sewing machine. This technique can be categorized into two types: one side stitching and two side stitching. Two side stitching can be done using different stitching processes, such as lock stitching, modified lock stitching, and chain stitching. In one side-stitching, the reinforcement can be inserted from one side using two needles, either straight or curved (see the Figure 0.3).

Each needle passes the thread through the preform, creating one or two loops on both sides of the preform. Research has shown mixed results regarding the impact of stitching on the in-plane mechanical properties of composites. While some studies have demonstrated improved properties, others have found no change or even degradation (Yudhanto et al., 2015; Mouritz, & Cox, 2010). Using two needles to insert fiber through the thickness during stitching may have a greater impact on reducing in-plane mechanical properties than using individual pins in Z-pinning techniques. The effectiveness of stitching can depend on various factors such as the type of yarn, stitch pattern, and spacing, which can lead to inconsistent results if not properly controlled.
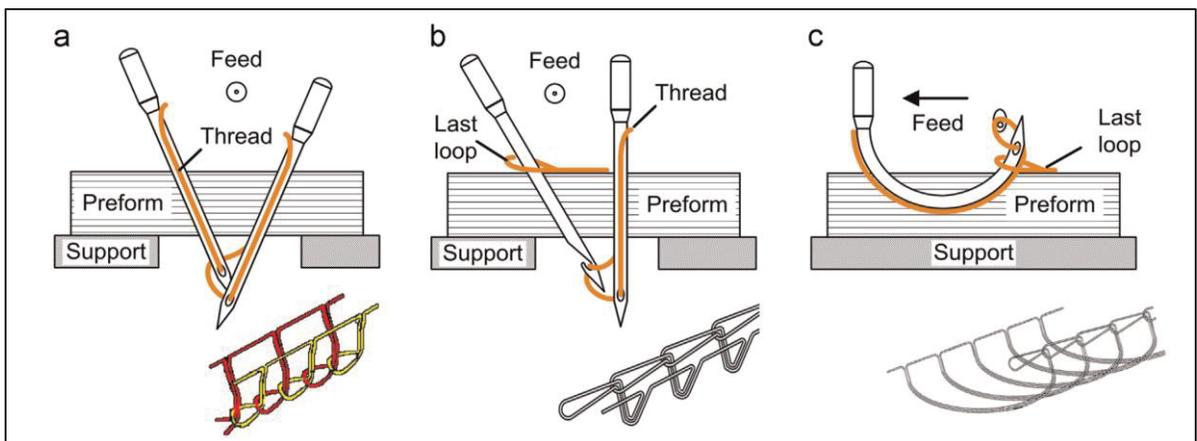
Figure 0.3 Schematic of one side stitching techniques: (a) two straight needles with one loop, (b) two straight needles with two loops, (c) one curved needle with one loop taken from Dell'Anno, Treiber, & Partridge (2016, p. 264)

0.2.4 Tufting

Tufting has a long history in the textile industry, but its use in composite materials began in the early 1990s. Figure 0.4(a) illustrates the process of tufting, which requires access to only one side of the preform. The needle is mounted on a tufting machine and is guided through the material in a specific pattern to create the desired design. The tufting machine also has a pressure foot that holds the material in place and ensures that the tufts are inserted at a consistent depth. Tufts are inserted using a hollow needle, which reduces tension on the surface of the laminate and minimizes voids and defects around each tuft after curing (Dell'Anno,

Treiber, & Partridge, 2016). There are two different ways to carry out the tufting process. The first method is referred to as "Global-tufting" or "fully inserted tuft", where the tufts penetrate the entire thickness of the preform and the loops can be seen at the bottom of the fabric. Partial-tufting is the other way of implementing the tufting process, where the tufts are not completely contained within the laminate. Figure 0.4(b) illustrates the distinction between these types of tufting. Reinforcing composite laminate through the thickness by tufting technique is considered to be more efficient and simpler than stitching techniques, which require a second thread for locking. Tufting only requires access to one side of the preform, making it a simple and efficient process. Obviously, the tufting process is quite similar to the z-pinning principle but is originally used to reinforce dry fabrics.
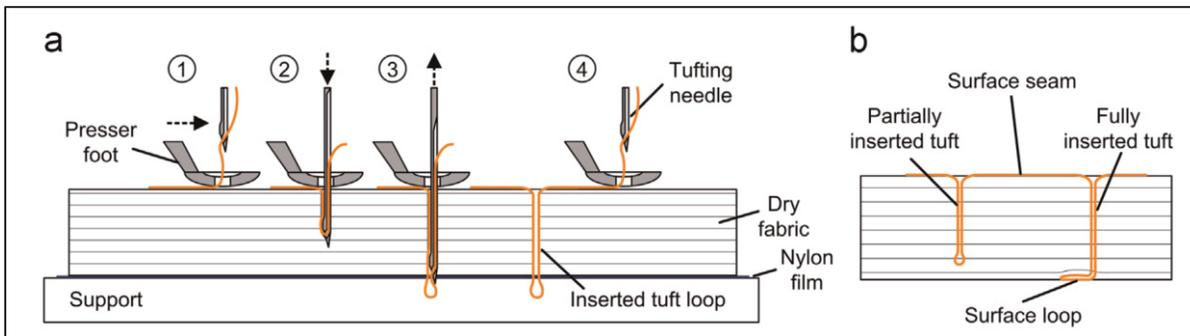
Figure 0.4 Schematic of tufting technique: (a) tufting processing (b) partial and fully-inserted taken from Dell'Anno, Treiber, & Partridge (2016, p. 264)

0.3   The importance of tufting

Tufting is a textile manufacturing process that has several advantages over other techniques like z-pinning, stitching, and 3D weaving. These benefits are outlined as follows:

- High damage tolerance and strength: This technique has superior mechanical properties compared to Z-pinning with large pins and it is less likely to produce defects and voids in the material due to utilizing a hollow needle to insert high-strength yarn or thread tufts through the layers of dry fabric [Mouritz, 2007].

- Cost-effective: Tufting is a relatively low-cost manufacturing process, as it does not require highly specialized equipment or labor-intensive techniques. This makes it an attractive option for different industries

- Versatility: Loop constructions (i.e., loop-less and with loop tufting geometry) achieved through tufting can indeed result in a wide range of textures and designs.

- Speed: Tufting is a fast process that can produce textiles quickly, especially compared to stitching and 3D weaving. This makes it an ideal choice for time-sensitive projects.

0.4   Thesis organization

The structure of this thesis consists of four main chapters. **Chapter 1** provides a comprehensive overview of the research objectives and the scope of the study. **Chapter 2** presents an overview of recent research on tufted composite laminates. This literature review covers both numerical and experimental studies. The methodology utilized in this study, which includes material processing, tensile testing, and CT-scan performing, is thoroughly described in **Chapter 3**. **Chapter 4** is dedicated to the presentation and discussion of the results. The focus is specifically on the analysis of the failure mechanisms within tufted laminates, taking into account various tufting geometries and laminate sequences. Finally, in **Chapter 5**, a detailed description of a 3D tufted laminate model is provided to detect and predict the failure mechanisms within tufted laminates. This chapter also presents the results obtained from the model and compares them with the experimental findings.

CHAPTER 1

RESEARCH OBJECTIVES AND ORIGINAL CONTRIBUTION

1.1   Research objective

In recent years, there has been a significant increase in the use of composite materials in aeronautics and land transportation systems, resulting in doubling the production of high-performance composite parts. To meet this growing demand, there have been considerable advancements in manufacturing processes and the development of new materials. New types of composites made with 3D textiles or through the thickness reinforced 2D textiles (TTR composites) have recently emerged, offering a wide range of possibilities for structural design that were previously unimaginable. One of the advantages of these new techniques is the ability to produce preforms to reduce production costs and increase the quality of the parts produced. TTR methods have provided a way for scientists and manufacturers to improve the structural performance of composites, as they address the weakness of out of plane properties. Our ability to predict the behavior of the structures made of these new materials is still very limited. Most of the researches focus on reinforcement techniques and the mechanical behaviors of composites, and less studies exclusively on TTR failure response under different fracture modes. This research focuses on tufting as a TTR method, given its reputation for being a more economical and effective option compared to other TTR techniques.

The main objectives of this work are outlined as follows:

- To investigate the effect of tufting geometry, specifically the presence of loops, on the failure mechanisms of tufted laminates under tensile loading.

- To examine the effect of laminate stacking sequences (orthotropic or quasi-isotropic) preform on the failure mechanisms of tufted laminates subjected to tensile loading.

- To identify the best tufted laminates in terms of stiffness, strength and fracture energy under elastic and plastic regimes when exposed to out of plane loading with various tufting geometries and laminate sequences.

- To develop a 3D finite element modeling approach to predict the failure mechanisms of orthotropic tufted laminates under elastic mode.

1.2   Original contribution

Finite element analysis of tufted composites can result in reducing labor and costs. Hence, the main contribution of this study will be to provide answers to the underlying failure mechanisms at the microscopic scale of tufted composites concerning different tufting geometry and laminate sequences under tensile loadings. This will generate ideas on how to model tufted composites in commercial FE software and help engineers to design new composite parts. Ultimately, when reliable tools will exist to model tufted composites, composite parts could be designed to optimize out of plane performance which nowadays is difficult to do. This research aims to use experimental analysis and microscopic imaging of tufted laminates during loading to develop a robust 3D model in Abaqus software. This model will be used to predict the experimental failure mechanism of the tufted laminates under tensile loading.

CHAPTER 2

LITERATURE REVIEW

2.1   Introduction

Despite the various advantages of composite materials, they are prone to delamination, especially under tensile and mode I loadings. As previously mentioned, several methods of 3D reinforcement have been developed to enhance the delamination toughness of polymer composites. However, there is a lack of research into tufted laminates under various loading conditions. The aim of this chapter is to review work on through the thickness reinforcement (TTR) with a specific focus on tufting on the in-plane and out-of-plane properties of composite laminates subjected to different loading. To assess the effectiveness of tufting in enhancing the properties of laminates, the influence of tufting parameters such as materials, geometry, density, and insertion angle is studied for different laminate sequences and materials. The primary emphasis of this chapter is to begin with a general literature review of TTR composite laminates. Subsequently, the focus will shift to a more detailed discussion of important papers that explore the tuft failure mechanisms within composite materials using both experimental and numerical approaches.

2.2   General literature review on TTR composites laminates

The laminate layup and several TTR parameters such as density, insertion angle, thread material, needle diameter and pattern can influence the in-plane behavior of TTR composites (Yudhanto et al., 2015; Mouritz et al., 2010; Dell'Anno et al., 2016; Treiber et al., 2009). Karuppannan et al. (2012) found that tufting results in a 30% and 19% decrease in in-plane tensile and compressive strength of unidirectional carbon composites respectively. They also reported a 3.5% increase in in-plane tensile strength for tufted composites with a quasi-isotropic layup. Verdiere et al. (2009) observed that tufted non-crimp fabric (NCF) laminates with [0/90]3S and [±45]3S layups experience a 13% decrease in tensile strength compared to

untufted samples during tensile testing. Moreover, the incorporation of tufting could potentially improve the interlaminar shear strength (ILSS) of $[0/90]_{3S}$ and $[\pm45]_{3S}$ NCF laminates. The $[0/90]_{4S}$ composite laminate experiences a 10-fold increase in mode I delamination and a 3-fold increase in mode II delamination.In other study, it is observed that the in-plane tensile strength of composite laminates is significantly influenced by the areal tufting density (Treiber, Cartié, & Partridge, 2011). For a tufting density of 0.5%, there is a reduction of 19% in in-plane tensile strength. Nonetheless, an increase in tufting density from 0.5% to 2% does not change the in-plane tensile strength properties.

It has been widely reported that tufting reinforcement can have a beneficial impact on enhancing the fracture toughness under both mode I and mode II loading conditions. Karuppannan *et al.* (2012) focused on unidirectional and quasi-isotropic tufted carbon fiber composites. This study reveals that the inclusion of tufting through the thickness results in a 16-fold increase in mode I fracture toughness. The angle of tuft insertion through the thickness of a composite material can also affect the mode I fracture toughness (Plain, Tong, 2010). The 0º angle stitched laminate enhanced the fracture toughness by 2.35 times compared to unstitched one. Increasing the tufting angle from 0º to 22.5º and 45º reduced fracture toughness at peak load by 12.2% and 20.2%, respectively. that the insertion angle could enhance the fracture toughness by 2.35 times compared to the tufted laminate at the 0º angle. The mode I fracture toughness of tufted composites is evaluated by Pappas *et al.* (Pappas et al., 2018) using a double cantilever beam test, with respect to different tuft density (i.e., distance between two tufts) and geometry (with and without loops). The results indicate that the failure mechanism of tufted composites is significantly affected by their tufting geometry. Tufted laminates without loops tend to experience tuft pulling out as the primary failure mechanism, which can enhance fracture toughness by 65% in comparison to laminates with loops. However, laminates with loops exhibit higher mode I strength compared to those without loops. It is worth mentioning that as the space between tufts decreases from 5mm to 2.5mm, the fracture toughness of tufted composites improves by 3.5 to 6 times when compared to neat composites. Osmiani *et al.* (2016) centered their attention on the behavior of tufted composites and the constitutive model of tuft bridging when subjected to mode I delamination. The researchers

assumed that the tuft acts like a rod embedded in the epoxy, with two ends clamped due to the presence of loops and threads. The accuracy of their constitutive model is verified by comparing it with both experimental and numerical analyses performed using double cantilever beam (DCB) tests. The study's results show that the predicted values of the constitutive model are highly consistent with the experimental results. Bigaud (2016) focused on the behavior of single tufts in composite laminates subjected to mixed-mode loading as four-point bending test. The results of the study show that the presence of tufts significantly increase the fracture toughness of the composite laminates under mixed-mode loading conditions. They also found that the location of the tuft within the laminate has a significant effect on the fracture behavior. Hence, a greater enhancement of fracture toughness can be achieved when the tuft is positioned closer to the crack tip.

The beneficial effects of TTR on the different type of composite structures have been also studied. Different authors have reported an enhancement in impact resistance of glass and carbon through the thickness reinforced sandwich structures under impact loading (S. Samlal et al., 2015; Henao et al., 2014; Lascoup et al., 2006). Stitched sandwich composites exhibit superior impact resistance in comparison to other composite materials. They have the ability to absorb greater impact energy, resist higher impact loads, and exhibit reduced damage area and penetration depth. The stitched sandwich structure with a carbon non-crimp preform demonstrates a substantial enhancement in bending modulus and strength of 278% and 900% respectively under 4-point bending tests (Lascoup et al., 2006). In another study conducted on glass fiber sandwich laminates subjected to impact loading, it is found that reducing the tufting spacing from 50 mm to 12.5 mm and using a 45° tufting angle can result in a 2.5-fold increase in the load of the first significant damage compared to specimens without tufting (Lascoup et al., 2010).

14

2.3 Significant research papers elaborating on the experimental and numerical investigation of failure mechanism within tufted laminates

To fulfill the objective of this study, an in-depth review of six significant papers is presented, focusing on the tuft failure mechanisms within or outside of the tuft materials under various tension, mode I, and mixed mode loading conditions. The discussion provides comprehensive details derived from both experimental and numerical papers, thereby enhancing the understanding of the subject matter.

2.3.1 Improving the non-impregnated tufting mechanisms during tuft insertion under tensile loading during the tuft insertion into the dry preforms

The primary aim of this research done by Chan *et al.*, (2019) is to reduce the degradation of tufting threads during insertion into dry preforms by introducing a new manufacturing technique. To accomplish this goal, the traditional tufting process and its impact on thread degradation are assessed with respect to different tufting densities. Based on the initial findings, the study introduces a new tufting process called the "two-step" to reduce tufting degradation while inserting into dry preforms. To investigate the degradation of non-impregnated tufting threads, a preform consisting of twenty E-glass cross-plies [0/90°] is used. Three types of tufted samples are prepared with different tufting densities (tufting distance): 9 mm, 6 mm, and 3 mm. The properties of the tuft material are outlined in Table 2.1.

Table 2.1 Main Properties of tuft thread taken from Chan et al. (2019, p. 425)

References	Linear density (tex)	Number of filaments	Twist (T/m)
Tenax-J HTA-40	2×67	2×1000	240±16

A tufting device is a machine used in the manufacturing process of tufted textiles or composite materials. It typically consists of several systems, including a tufting system, a presser foot system, a feeding system, and a frame (Dell'Anno, Treiber, & Partridge, 2016). This machine aids in pushing the needle through the dry textile, resulting in the formation of a looped tuft in the preform. Figure 2.1 illustrates the tuft thread degradation for non-inserted and inserted tufts

through dry preform with three different tufting densities (9mm, 6mm and 3mm). The degradation occurs due to the insertion of the threads, which is a result of the initial friction between the threads and the preform as they traverse the tufting path. Given Figure 2.1, there is an increase in the amount of tuft degradation as the tufting density increases from 9mm to 3mm.
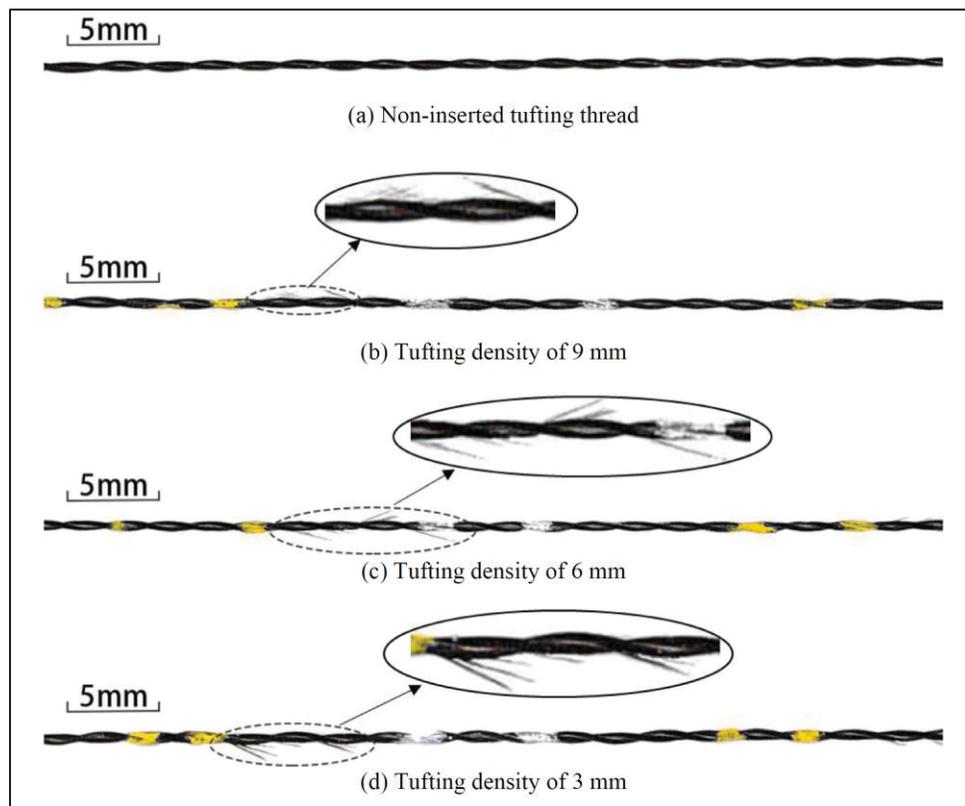
Figure 2.1 Image observation of non-inserted and inserted tufting threads with different density taken from Chan et al. (2019, p. 426)

To confirm this observation, additional analysis of the tufting threads degradation is carried out through tensile characterization tests. Each type of sample undergoes five repetitions of the tensile test to obtain an average value. The length of the tested thread is 250mm, and the crosshead speed is set at 5 mm/min. Figure 2.2 shows the load-strain curves for both the non-inserted and inserted tufting threads under the tensile test. It can be observed that the maximum tensile loads before tuft failure are $121 \pm 2N$, $112 \pm 3.9N$, and $109 \pm 0.9N$ for the samples with

tufting density of 9, 6, and 3 mm, respectively. These values represent a degradation of 14%, 21%, and 23% compared to the maximum tensile load of non-inserted thread (141 ± 4.3 N). The strain at break shows a degradation of 4%, 10%, and 15% for the tufting densities of 9, 6, and 3 mm, respectively in the comparison with non-inserted tuft strain failure.
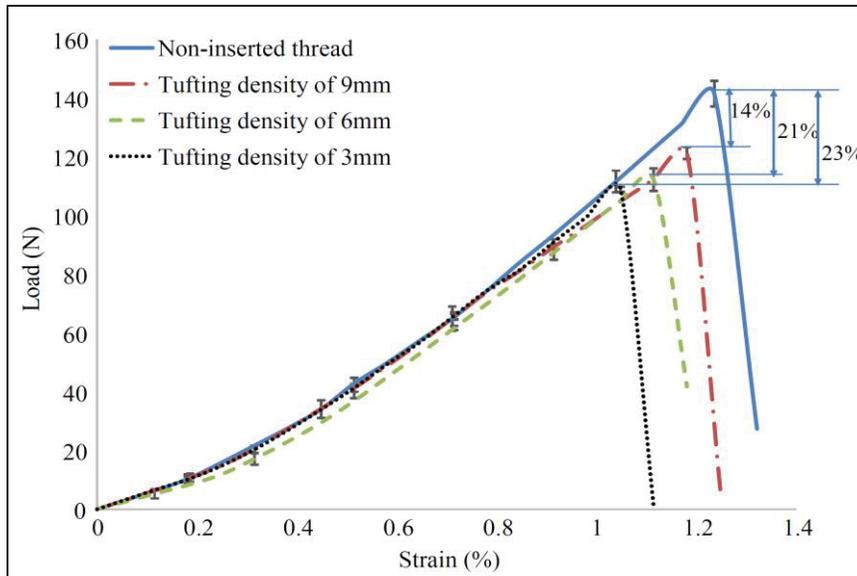
Figure 2.2 Tensile load-strain curves of the non-inserted and inserted tufting threads taken from Chan et al. (2019, p. 427)

To minimize degradation, a second needle that closely resembles the tufting needle but without a thread is suggested to serve as a guide needle (as can be seen in Figure 2.3). The improved tufting process involves two steps. Firstly, the guide needle without threads is inserted into the preform (as shown in Figures 2.3(a-b)), and then the tufting needle with the tufting threads is inserted into the preform through the same path as the guide needle (as shown in Figure 8c). The guide needle creates a space-room reducing the effect of friction between the threads and the preform, which in turn decrease the lateral contact and transverse compaction of the inserted threads (Figure 2.3(d)). The two-step process helps to reduce thread degradation and improve the tufting process. It's worth noting that the guide needle has a slightly smaller diameter than the tufting needle. This is because the inserted threads rely on friction and lateral contact to stay in place and prevent them from coming out of the preform.
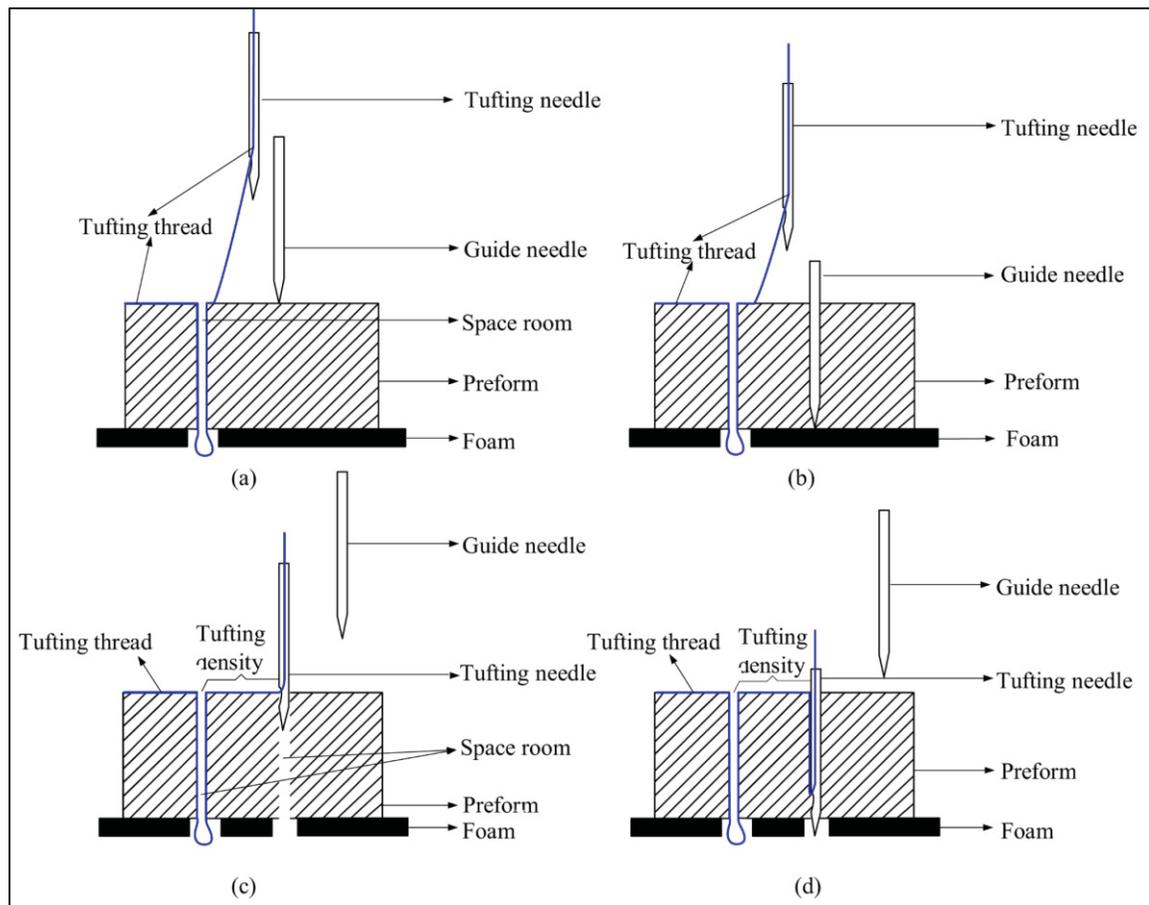
Figure 2.3 Schematics of two-step tufting process taken from Chan et al. (2019, p. 428)

Figure 2.4 displays the load-strain curve of a single inserted thread in the two-step tufting process. The maximum tensile load of the inserted thread in the two-step tufting is 128 ± 1.9 N for 9mm tufting density, which is only degraded by 9% compared to the non-inserted thread. Additionally, the breaking strain of the inserted thread in the two-step tufting is 1.24% for 9mm tufting density, which is not degraded compared to the non-inserted thread. Consequently, this technique suggests that the use of the guide needle in the two-step tufting process effectively reduces the degradation of the inserted threads and improves their tensile performance. Overall, the use of a guide needle during the two-step tufting process lead to a decrease to 0%, 4% and 10% for 9, 6 and 3 mm tufting densities for tufting densities of 9, 6, and 3mm, respectively. Moreover, compared to the conventional tufting method, the two-step tufting with

a guide needle results in an improvement of breaking strain of 5.7%, 6.0%, and 6.3% for tufting densities of 9, 6, and 3mm, respectively.
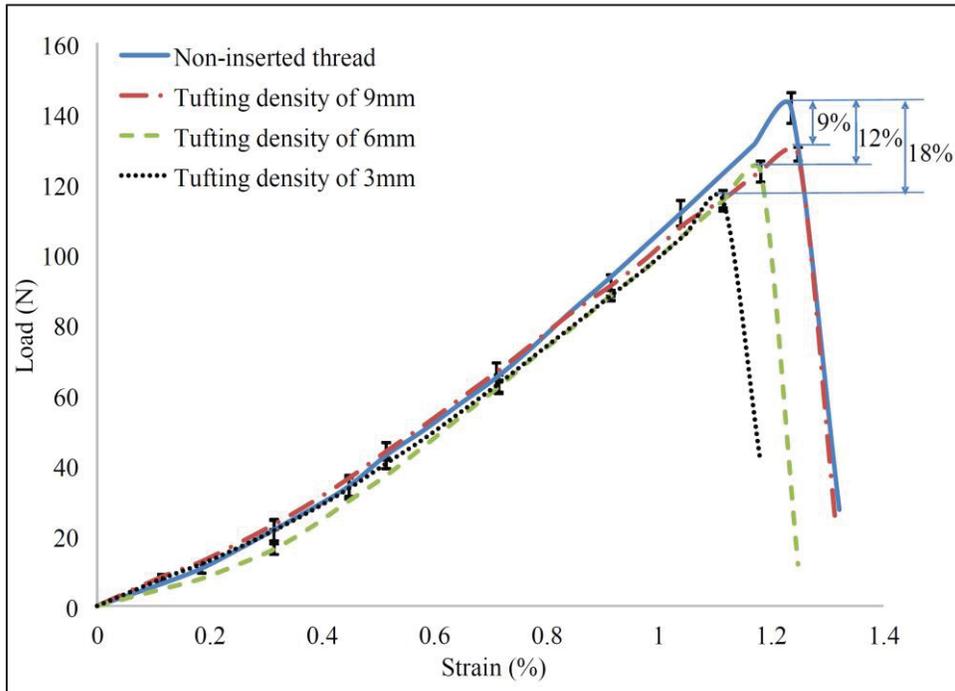
Figure 2.4 Tensile load vs. strain curves of the inserted tufting threads in two-step tufting taken from Chan et al. (2019, p. 429)

2.3.2 The influence of tufting geometry and pattern on delamination of fiber-reinforced composites under mode I

Pappas *et al.* (2018) studied the effect of tufting pattern (tufting density) and geometry (with and without loop) on woven glass fiber reinforced composites (GFRP) subjected to mode I. In order to examine the failure response of carbon tufts and ply delamination in GFRP composite laminates, a Mode I experiment is carried out on specimens with and without tufts, utilizing the double cantilever beam (DCB) method. To investigate how the delamination mechanism of GFRP specimens is affected by the tufting pattern and geometry, six distinct types of regions are created in the preforms. These included: i) neat (Nt) GFRP regions, ii) Nt GFRP regions with a mid-plane release film, iii) tufted regions with a 5 mm squared (5-SQ) pattern (4 tufts/cm2), iv) 5F-SQ pattern with mid-plane release film, v) tufted regions with a 4 mm

squared (4-SQ) pattern (6 tufts/cm2), and, vi) tufted regions with a 5 mm staggered (5-ST) pattern (7.2 tufts/cm2) as shown in Table 2.1 Moreover, the impact of tuft geometry on delamination resistance is also studied in this study. To achieve this, some plates are milled down on both sides to produce loop-less tufted laminates. The final thickness of the milled down plates is 5.85 ± 0.06 mm for all investigated patterns whereas for standard one, it is approximately 7.5 ± 0.5 mm. The width and length of DCB laminates are 25mm and 250mm respectively. The initial interlaminar pre-cracks in the samples have a length of approximately 65 ± 7mm. These cracks are positioned at a distance of around 10–20mm before the first row of tufts. This arrangement allows for the development of a natural crack initiation before reaching the tufted regions.

Based on the preliminary experiments conducted on the tufted composite, it has been observed the arms of the material tend to bend and fail before complete separation or breakage of the tufts occurs. Therefore, to address this problem, it is necessary to reinforce and stiffen the arms. This reinforcement is achieved by bonding two symmetric polymethyl methacrylate (PMMA) beams, with a thickness of 14.6 ± 0.2mm for the standard series and 11.6 ± 0.15mm for the milled-down ones, and a certain width. Equations 2.1 present an approach for experimentally measuring the Energy Release Rate (ERR). This equation describes the Modified Compliance Calibration (MCC) method, where the reaction load (P), compliance (C), and crack length (a) are all recorded to determine ERR. In this equation, $G_{I,i}$ represents the initial fracture toughness, while $G_{i,b}$ describes the contribution of crack bridging phenomena (tow/ply and tuft) to the fracture resistance.

$$G_{total} = G_{I,i} + G_{i,b} = \frac{P^2}{2B}\frac{dC}{da} \tag{2.1}$$

Table 2.2 presents the ERR values for all the specimens analyzed in this study. The data in this table indicates that using tufts with different geometries (with or without loop) and patterns (5-SQ, 4-SQ, 5-ST) can improve the fracture toughness of GFRP by 2-10 times. As illustrated in Figure 2.5(a), increasing tuft density from 5-SQ, 4-SQ to 5-ST can enhance the resistance and energy rate of composite structures under mode I. Additionally, surface machining of the tufted

GFRP provides loop-less tufts that behave differently in comparison with the standard tufts during delamination. The milling down of both sides of standard tufted GFRP (5-SQM, 4-SQM, 5-STM) series alters the failure mechanism in tufted composites. Tuft rupture is the main failure mechanism in with-loop tufts while frictional pull-out occurs in loop-less one. As a result, pulling out of tufts in comparison with rupturing almost doubles EER during delamination (see Figure 2.5(b)).

Table 2.1 DCB specimen description and nomenclature taken from Pappas et al. (2018, p. 926)

Pattern/density	Schematic	Name	Description	Number of specimens
Non-Tufted	-	Nt	Neat GFRP with and without release film at mid-plane,	3
		Nt PMMA	Neat GFRP with PMMA	2
5mm squared (4 tufts/cm2)	$B=25mm$ $\ell=5mm$	5-SQ	5mm squared (standard tuft)	3
		5F-SQ	5-SQ with release film at mid-plane	3
		5-SQM	5-SQ, with loop-less tufts (milled-down)	3
		5F-SQM	5F-SQ, with loop-less tuft (milled-down)	3
4mm squared (6 tufts/cm2)	$\ell=4mm$	4-SQ	4mm squared pattern (standard tufts)	3
		4-SQM	4-SQ, with loop-less tufts (milled-down)	3
5mm staggered (7.2tufts/cm2)	$\ell=5mm$	5-ST	5mm staggered pattern (standard tufts)	3
		5-STM	5-ST, with loop-less tufts (milled-down)	3
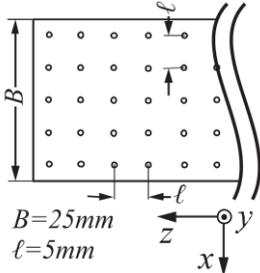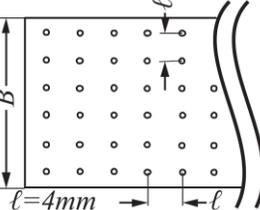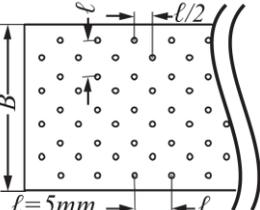
Table 2.2 Mean experimental ERRs at steady-state taken from Pappas et al. (2018, p. 930)

Specimens	Nt	5F-SQ	5-SQ	4-SQ	5-ST
ERR/Exp.	0.90±0.10	1.90±0.15	3.10±0.30	5.35±0.30	5.15±00.30
ERR/Est.	-	-	2.80	3.75	4.30
Specimens	Nt-PMMA-M	5F-SQM	5-SQM	4-SQM	5-STM
ERR/Exp.	-	3.35±0.40	5.05±0.15	8.50±0.35	9.2±0.3
ERR/Est.	0.75	-	4.1	5.75	6.75
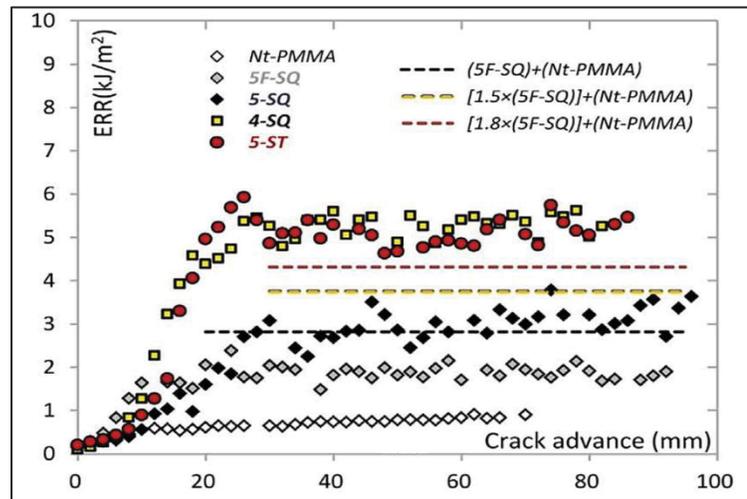
(a)
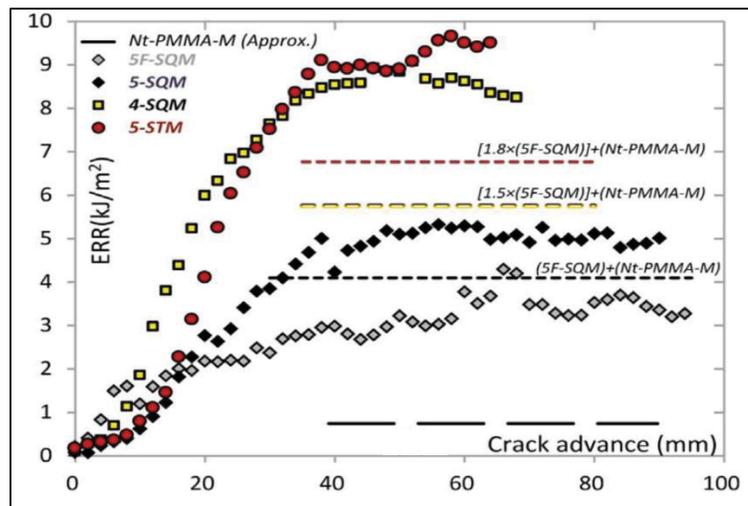
(b)

Figure 2.5 Experimental average ERR-curves: (a) standard and (b) loop-less tufting samples taken from Pappas et al. (2018, p. 933)

22

2.3.3   Determination of crack bridging laws in tufted composites under mode I and mixed mode

The researcher conducted a study on the crack bridging behavior of tufted composites under different loading conditions (Treiber et al., 2009). They investigated the effect of different types reinforcement (unidirectional (UD), woven and non-crimp fabrics (NCF)) and tufts (glass, carbon, stretch carbon) on the crack bridging behavior of tufted composites. The study is conducted under mode I and mixed-mode loading conditions. Table 2.3 displays the preform and tuft material utilized in this study. Their findings indicate that the resistance of tufted composites under mode I is primarily dependent on the mechanical properties (stiffness and strength) of the tufts. However, the bridging laws in tufted composites under mixed-mode shearing is heavily influenced by both the mechanical and geometrical properties of the composite laminate.

Table 2.3 Material description of the preforms and tufts taken from Treiber et al. (2009)

	Brief Name	Description
Preform	Twill	Carbon 2x2 twill woven fabric
	NCF	Carbon 0°/90° non-crimp fabric
	UD	Carbon unidirectional fabric
Tuft	C-Tuft	Tenax® carbon sewing thread
	C-Stretch	Schappe carbon stretch broken filament thread
	G-tuft	EC 9 68 x 3 S260 T8G Saint Gobain Vetrotex Glass Thread

Figure 2.6 provides a schematic of the mode I and mixed-mode loading setups using tensile and shear jigs, respectively. In mode I, the specimens are secured by bonding each sample between two vertically loaded steel t-tabs using cyanoacrylate. On the other hand, in mixed mode, the specimens are attached between two shear arms, with a consistent crosshead speed of 0.25 mm/min. Figure 2.7 shows the force-crack opening displacement diagrams of the specimens under mode I delamination. The curves for all tufted laminates exhibit an elastic behavior in the initial section. Afterward, the axial stress reaches the material's final strength, and the tufts start to break down at the maximum point. Figure 2.7(a) shows that the UD

laminate with a single carbon tuft displays the greatest reaction force and the lowest crack opening displacement before failure, causing a decrease in energy dissipation. On the other hand, the NCF laminate has a higher load compared to the twill laminate (with woven preform), but both laminates exhibit almost the same frictional pull-out. Figure 2.7(b) indicates that substituting a glass tuft for a carbon tuft in the NCF preform results in a reduction in the amount of tensile load. However, the frictional pull-out remains the same.

(a)   (b)
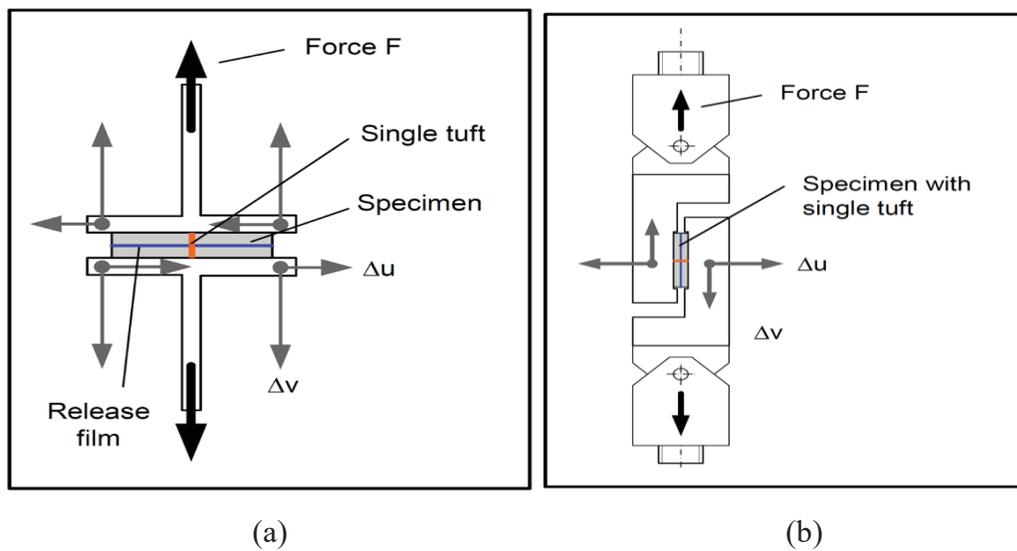
Figure 2.6 Experimental set-up for different fracture modes: (a) mode I and (b) mixed mode taken from Treiber et al. (2009)

Figure 2.8 depicts the tuft bridging laws subjected to mixed mode in terms of both crack opening and crack shear displacement. The amount of crack shear displacement is greater than the crack opening displacement in mixed-mode loading conditions. To assess the impact of the surrounding laminate geometry on the shear behavior, single tufts in NCF and UD laminates are tested in two directions: parallel (0^0) and orthogonal (90^0) to the tuft direction. Figure 2.8(a) and (b), indicate that the amount of bridging load has increased by altering the reinforcement direction from parallel (0^0) to orthogonal (90^0) to the tuft. Nonetheless, this increase in UD laminates is significant when compared to NCF laminates. Moreover, changing the fiber orientation from 90° to 0° in relation to the tuft direction leads to the expansion of the plastic regime in force-shear curves resulting in an increase in fracture energy. Upon comparing Figure 2.8(a) and Figure 2.7(a), in mode I loading as opposed to the mixed mode condition,

the UD and NCF laminates have a larger elastic behavior (ultimate strength) with a reduced extent of plastic deformation.

(a)   (b)
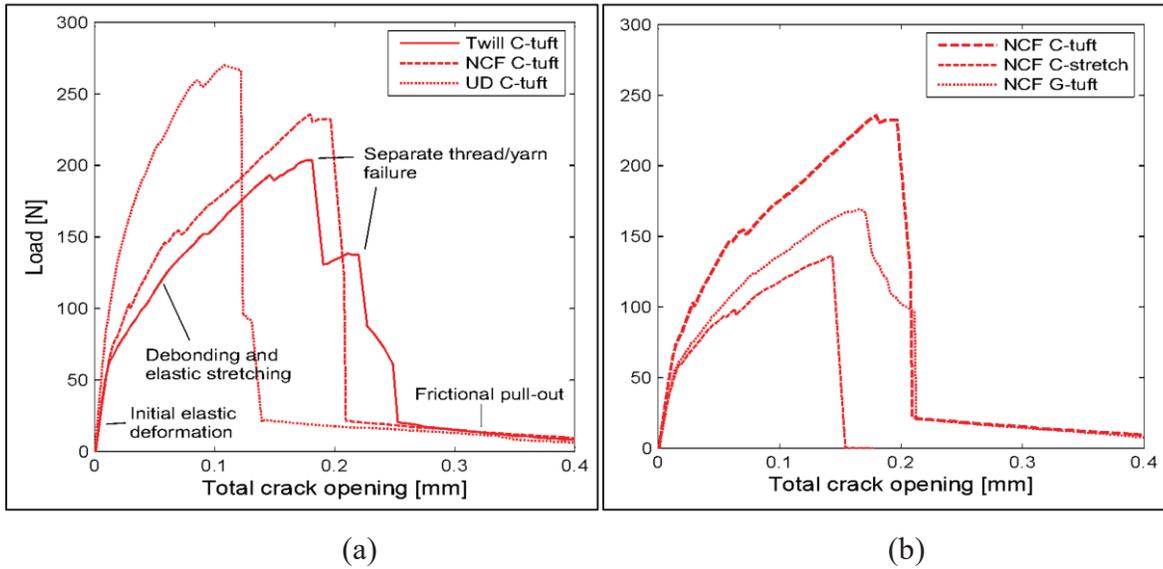
Figure 2.7 Experimental mode I bridging laws with different tuft materials and preform layups taken from Treiber et al. (2009)

(a)   (b)
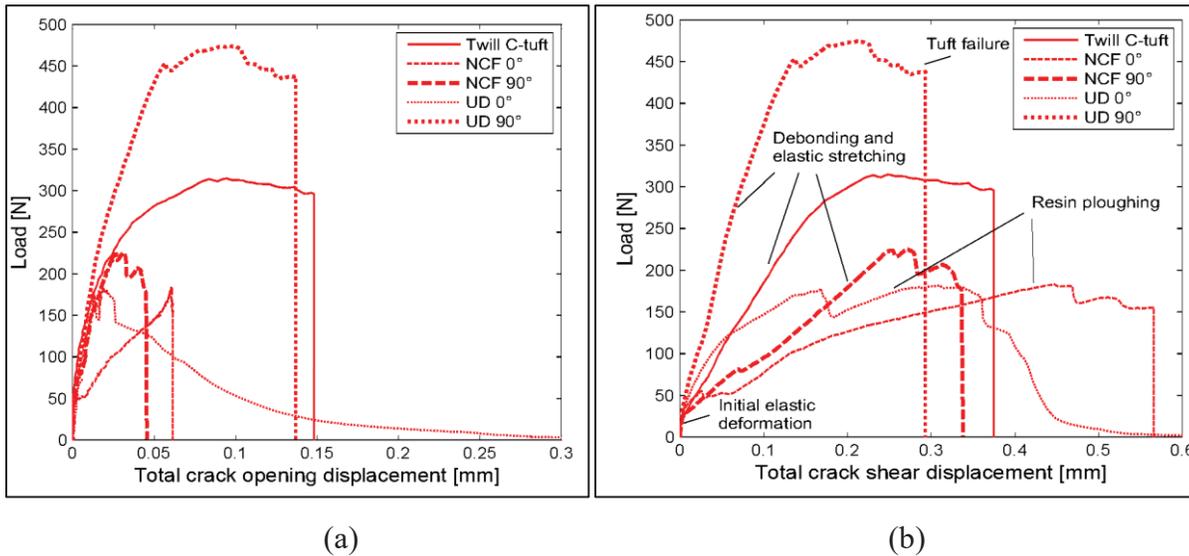
Figure 2.8 Experimental mixed mode bridging laws for carbon tufted laminates: (a) crack shear component and (b) crack opening component taken from Treiber et al. (2009)

Figure 2.9 displays a comparison of the pull-out bridging laws of the tufted NCF laminate with an intact and removed loop. The shaded area indicates the energy dissipated during the pull-

out of the tuft with the removed thread loop. The frictional pull-out of the NCF laminate with the presence of a loop-less tuft enhances the dissipated energy by 83% to 100 N.mm for a pull-out length of 2.2 mm.
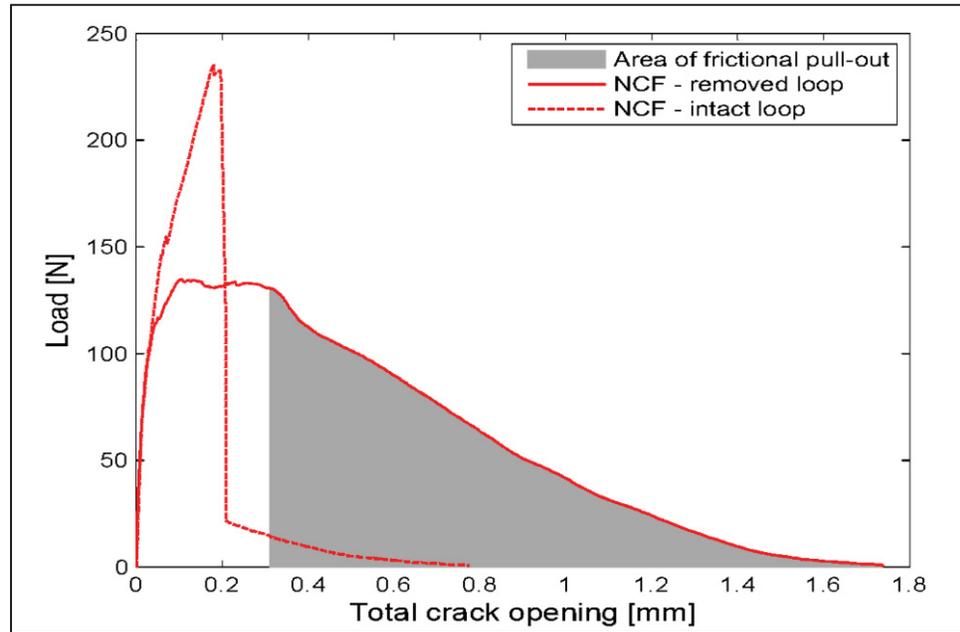
Figure 2.9 Experimental mode I load-displacement response of tufted NCF laminate with respect to loop-less and with loop tufting geometry taken from Treiber et al. (2009)

2.3.4 Double cantilever beam (DCB) modelling of tufted composite respect to tuft geometry and density

This study focuses on modeling techniques and experimental results of TTR glass reinforced laminates delamination subjected to DCB experiments (Pappas et al., 2017). In the DCB simulation, the damages can be propagated at the laminate level and in the tufts. Cohesive elements are used to simulate delamination while 1D connector elements are applied to introduce tufts properties. The mechanical properties of these two elements are derived through an inverse scheme that utilizes experimental strain measurements from DCB tests conducted on untufted composites, as well as the force-separation relationships obtained from tensile experiments performed on tufts. In 2D DCB modeling, connector elements are used to simulate tufts as a row. To accurately model the tuft behavior, the force-separation response of a single

tuft under tension is needed. To obtain this information, standard and loop-less tufted samples with 9 tufts through the thickness are tested in tension and then normalized per single tuft (see Figure 2.10). Figure 2.10(a) depicts the force-displacement curve for the standard tufts, highlighting four significant regions identified between points O and D. Each region corresponds to distinct fracture mechanisms. The characterization of these four sections is recognized by utilizing knowledge of composite behavior. Path OA *and* OB correspond to the elastic and plastic hardening properties of the tuft material, while point B indicates the tuft ultimate tensile strength. Following point B, the failure of the interface and tuft continues until point D, where the tuft experiences ultimate failure.

Figure 2.10(b) depicts the force-displacement relationship for the loop-less tuft series, normalized per single tuft. The failure mechanisms are similar to those observed in the standard tufted geometry up to point B, which corresponds to the ultimate shear strength due to friction at the tuft/GFRP interfaces. From point C to D, the tuft pulling-out process continues until complete failure (point D).
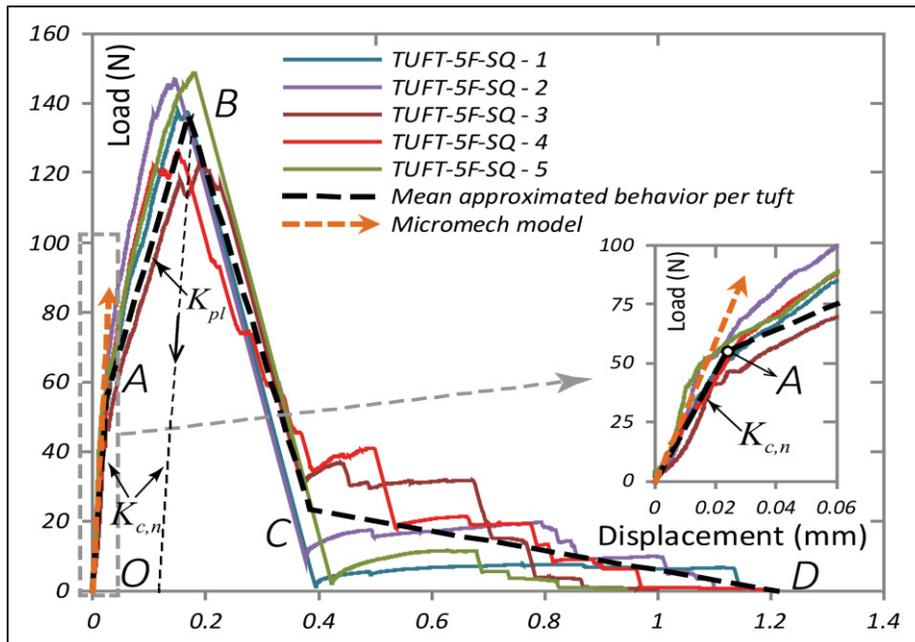
(a)
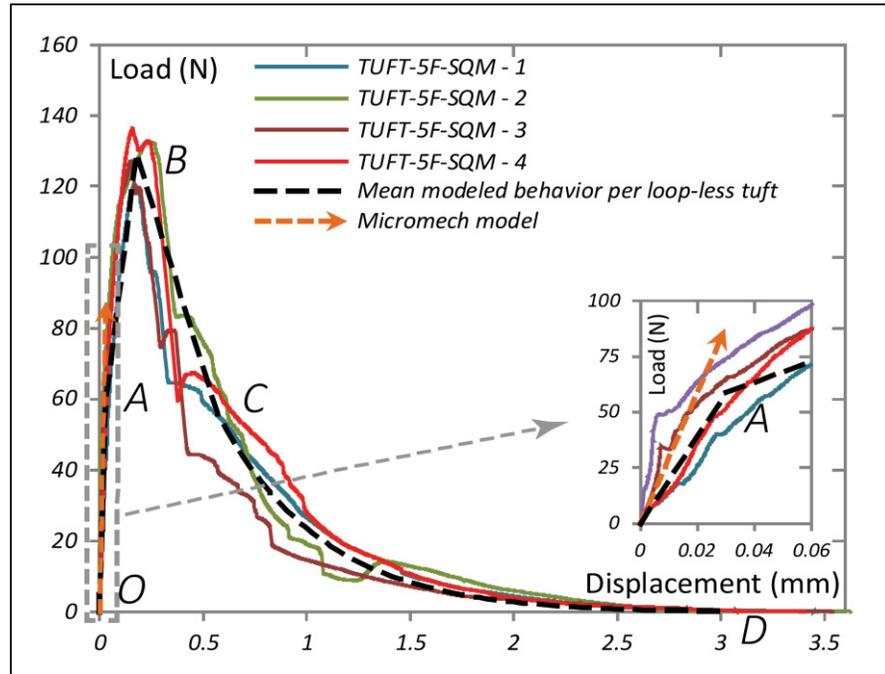
(b)

Figure 2.10 Experimental load-displacement response for different tufting geometry under tensile tests:(a) standard tufts and (b) loop-less tufts taken from Pappas et al. (2017, p. 388)

The cohesive zone is implemented for the tow/ply bridging phenomena. To build up this element, it is necessary to have the traction (σ)-separation (δ) relation of DCB experiments on a neat composite without tufts. The PMMAs are bonded above the composite arms to prevent any bending and damages within the arms during DCB experiment. Figure 2.11 reveals the traction-separation law for the neat GFRP samples reinforced by standard and milled-down PMMA for two different composite thickness obtained by experimental strain measurements. As shown in Figure 2.11(b), there are two significant zone occurring in the tow/ply delamination of GFRP. The first phase occurs when the cohesive zone meets the ultimate strength of epoxy (σ_c) (0 to δ_1) named as processing zone while, the second phase represents the tow/ply bridging zone (δ_1 to $\delta_1+\delta_{max}$). Equations 2.2 and 2.3 establish a correlation between stress (σ) and crack shear displacement (z) for the two mentioned zones, utilizing the numerical representation of the cohesive law depicted in Figure 2.11(a). The ultimate stresses of epoxy and tow/ply bridging are denoted by σ_c and σ_{max}, respectively. The initial and maximum shear displacements are represented by z_0 and z_{max} respectively. The softening coefficient is γ, and K_0 represents the elastic stiffness of resin.

$$\text{(Processing zone)}$$

$$\sigma_{pz}(z) = \sigma_c - \frac{\sigma_c - \sigma_{max}}{z_0} z, \qquad 0 \leq z < z_0 \tag{2.2}$$

$$\text{(Bridging zone)}$$

$$\sigma_b(z - z_0) = e^{-\gamma(z-z_0)} \left(\sigma_{max} - \frac{\sigma_{max}}{z_{max} - z_0}(z - z_0) \right) \; for \; z_0 \leq z < z_{max} \tag{2.3}$$

Equation 2.4 presents the overall ERR (J_{total}) combining two zones of J_{pz} (processing zone) and $J_{I,b}$ (tow/ply bridging) as described in Figure 2.11(b), where the crack shear displacement (z) is substituted with the crack opening displacement (δ). Equation 2.5 presents the formulation for establishing the traction-separation (σ-δ) response of GFRP tow/ply bridging by incorporating a damage factor of D (δ) varied in value along the traction-separation curve. The definitions of the parameters utilized in this equation are provided in Figure 2.11(b).

$$J_{total-SS} = J_{PZ} + J_{I.b} = \int_0^{\delta_1} \sigma_{PZ}(\delta)d\delta + \int_{\delta_1}^{\delta_1 + \delta_{max}} \sigma_b(\delta) \, d\delta \tag{2.4}$$

$$\sigma = \left(1 - D(\delta)\right)K_0\delta \quad with \; D(\delta) =$$

$$\begin{cases} 0, \; \delta \in [0, \delta_C] \\ \frac{\delta_1(\delta + \delta_C)}{\delta(\delta_1 - \delta_C)}, \quad \delta \in (\delta_C, \delta_1], \; \delta_1 = \delta_C + (1 - \frac{\sigma_{bmax}}{\sigma_c})(\delta^d - \delta_c) \\ 1 - \frac{\sigma_b(\delta)}{K_0\delta}, \; \delta \in (\delta_1, \delta_{max} + \delta_1] \end{cases} \tag{2.5}$$

Figure 2.12 displays a comparison between the results of load-displacement obtained from DCB tests and FEM results. The DCB test configuration and results are discussed earlier in section 2.3.2. The tests are conducted with a square reference pattern of tufts, with full-length mid-plane release film (5F-SQ), and without the release film (5-SQ). In Figure 2.12(a), the modeled response of 5F-SQ is very close to the experimental one with a slight underestimation. The load-displacement curve predicted by FEM for the 5-SQ configuration is slightly underestimated compared to the experimental results by approximately 10%, as shown in Figure 2.12(b). The underestimation can be attributed to the 2D nature of the model, where each connector's failure represents the failure of one complete row of tufts, while in the experiments, a combination of 2-3 rows of tufts contribute to the failure.
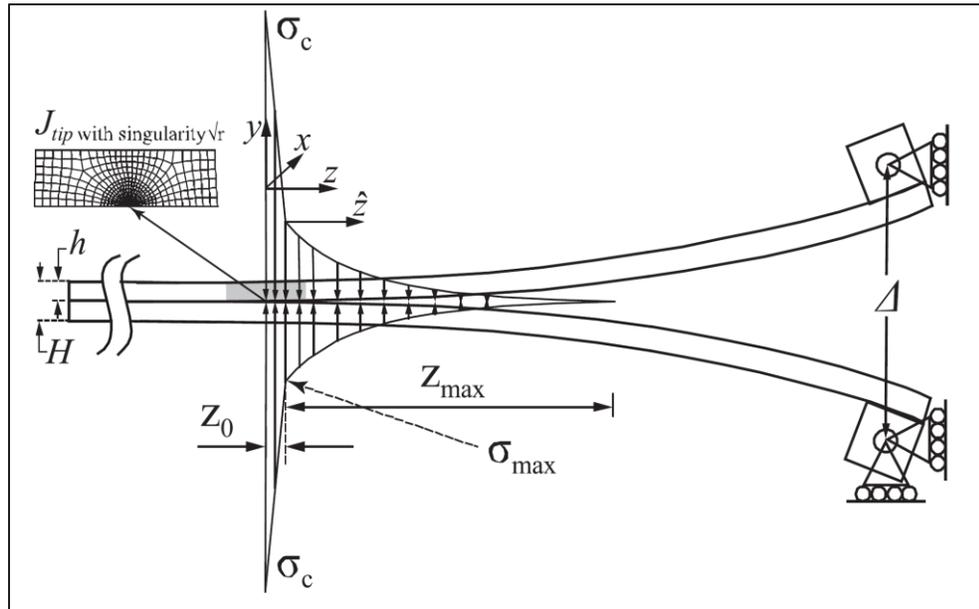
(a)
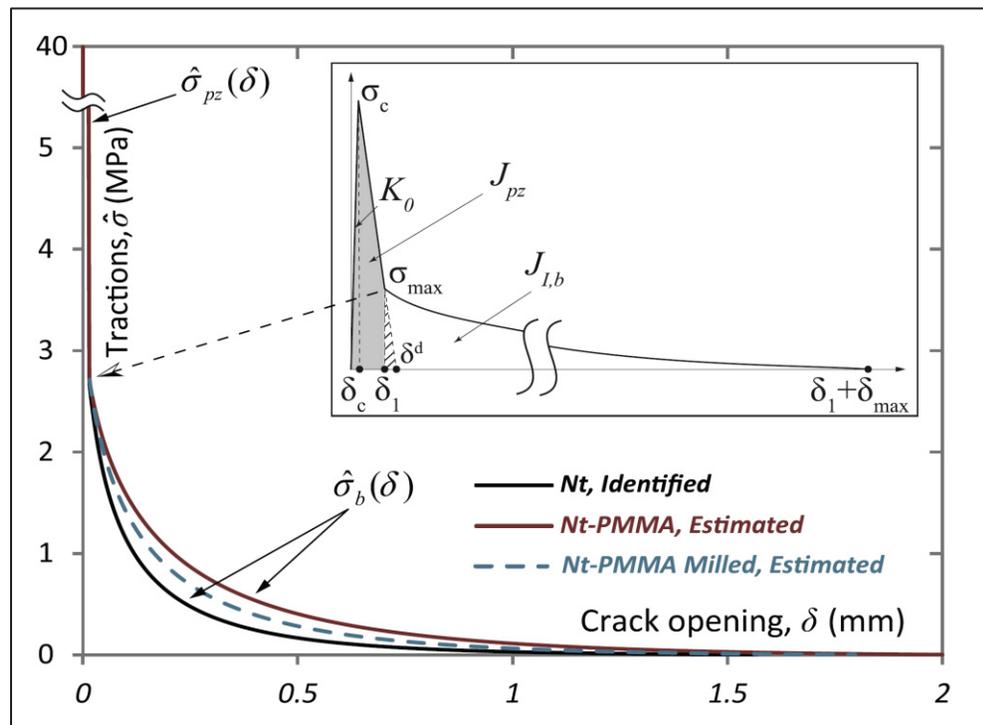
(b)

Figure 2.11 Traction-separation relations for neat GFRP laminate: (a) numerical scheme and (b) experimental cohesive law taken from Pappas et al. (2017, p. 384)
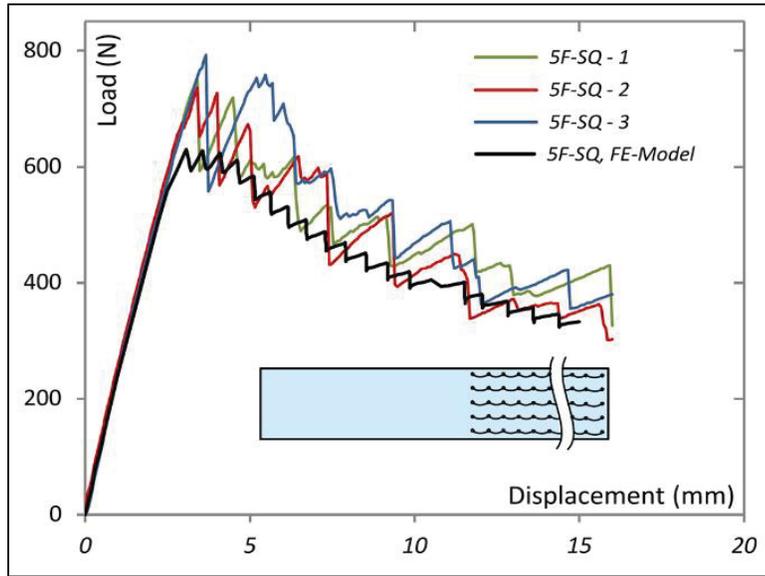
(a)
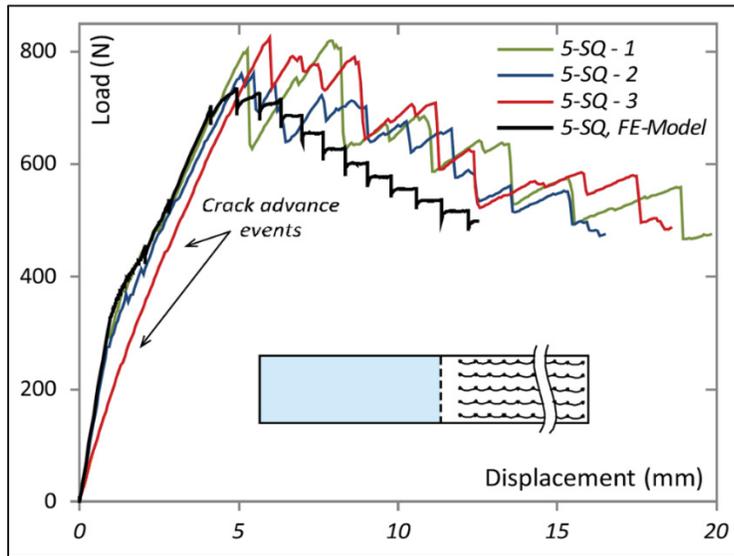
(b)

Figure 2.12 Experimental load-displacement curve and numerical prediction: (a) 5F-SQ and (b) 5-SQ taken from Pappas et al. (2017, p. 387)

The modeling technique described is employed to simulate samples with different tufting patterns of 4-SQ and 5-ST configurations. The load history predictions are illustrated in Figure 2.13(a) and (b). A very good fit at the beginning of linear part involving initial tow/ply bridging phenomena before the tuft bridging initiates is demonstrated in Figure 2.13(a) and (b). The

occurrence of tufting and tow/ply bridging result in a 30% and 20% underestimation of the predicted load-displacement curves for the 4-SQ and 5-ST samples, respectively, compared to the experimental results. This underestimation between predicted and experimental DCB load history can be attributed to the changes in the patterns of tufting (4-SQ and 5-ST), assuming that the tow/ply bridging phenomena is not affected. To address this underestimation, increasing $F_{C,B}$ of standard tuft ultimate load in Figure 2.10 (a) by approximately 35% (equivalent to a 21% increase in fracture toughness) lead to good agreement between simulations and experimental results suggesting that tuft strength is influenced by tufting patterns. The force-displacement curve shown in Figure 2.14 illustrates the predicted delamination behavior of the 4-SQM (without loops) pattern with experimental results. However, the FEM shows a lower magnitude compared to the experimental results by approximately 20%. It is recommended to double the value of J_{total} (energy toughness) in the cohesive zone when transitioning from the 5SQM tufting pattern to the 4SQM tufting pattern. The results indicate that increasing the fracture energy of cohesive elements yields outcomes that resemble the experimental results more closely than before, though there is still underestimation.

(a)

32
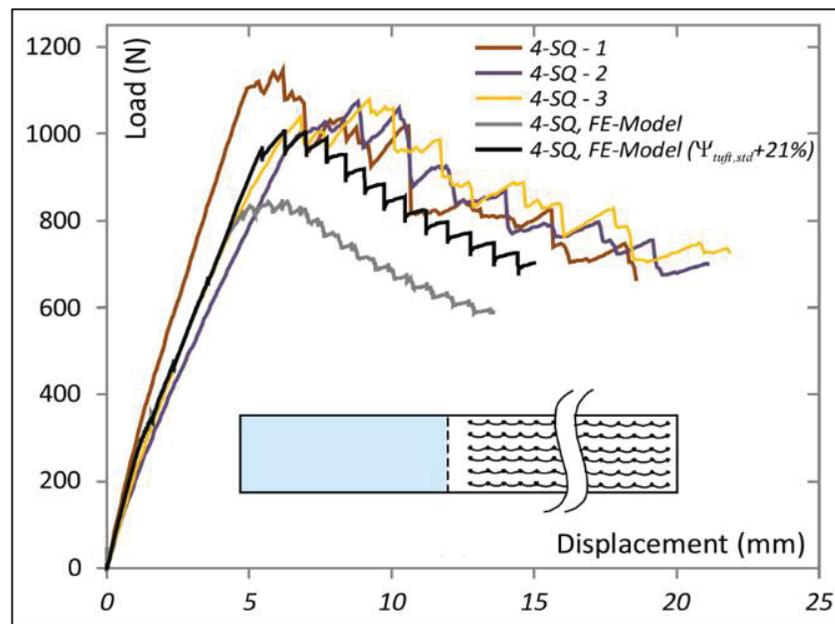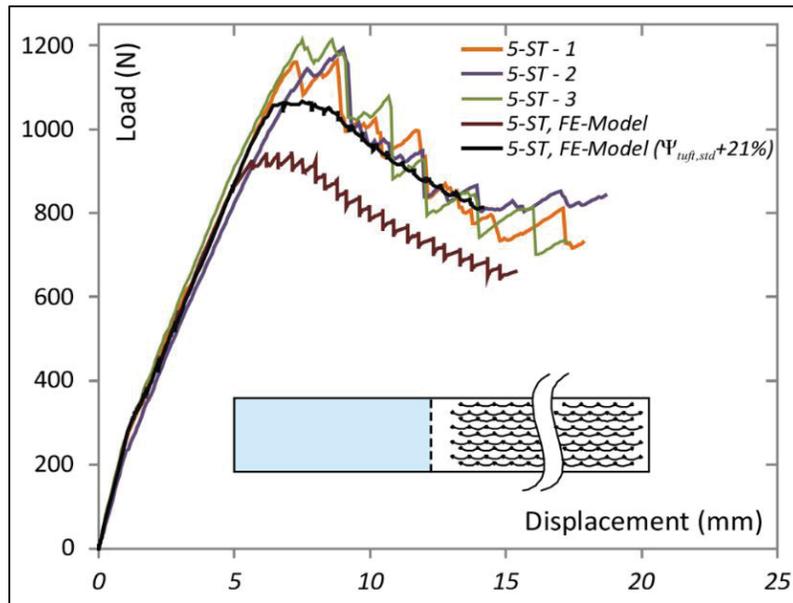
(b)

Figure 2.13 Experimental load-displacement curve and numerical prediction: (a) 4-SQ and (b) 5-ST taken from Pappas et al. (2017, p. 388)
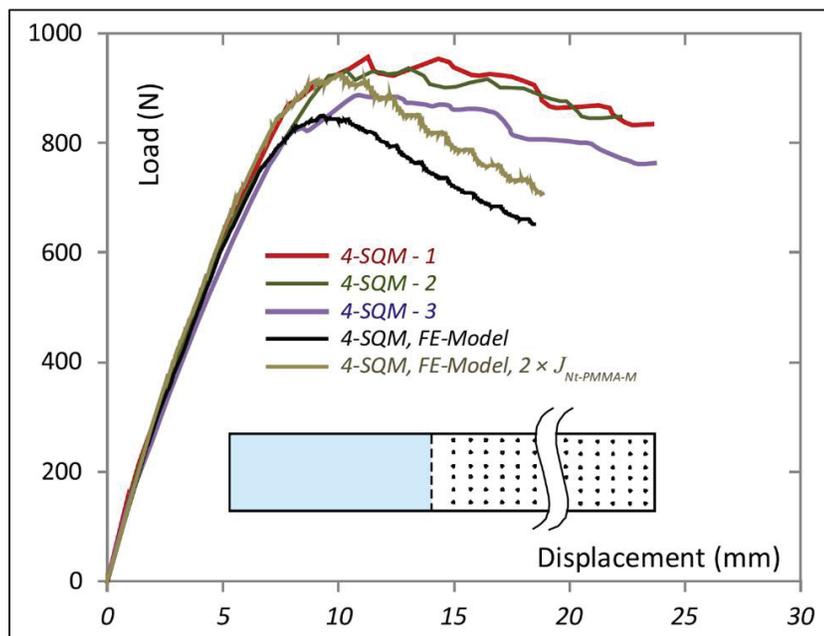
Figure 2.14 Experimental load-displacement curve and numerical prediction of 4-SQM taken from Pappas et al. (2017, p. 389)

2.3.5 Finite element modelling of through-thickness reinforced composite laminates under tension

This study developed an efficient and accurate finite element simulation for predicting the failure response of a single through the thickness reinforcement (Z-pin) under tensile quasi-static conditions while considering a frictional contact between the TTR and matrix (Meo et al., 2005). In a TTR/matrix pull-out test, the TTR is progressively pulled out experiencing three different stages: elastic deformation where the TTR/matrix interface is fully bonded; initial debonding of interface and frictional sliding where the TTR is fully debonded from the matrix (see Figure 2.15).
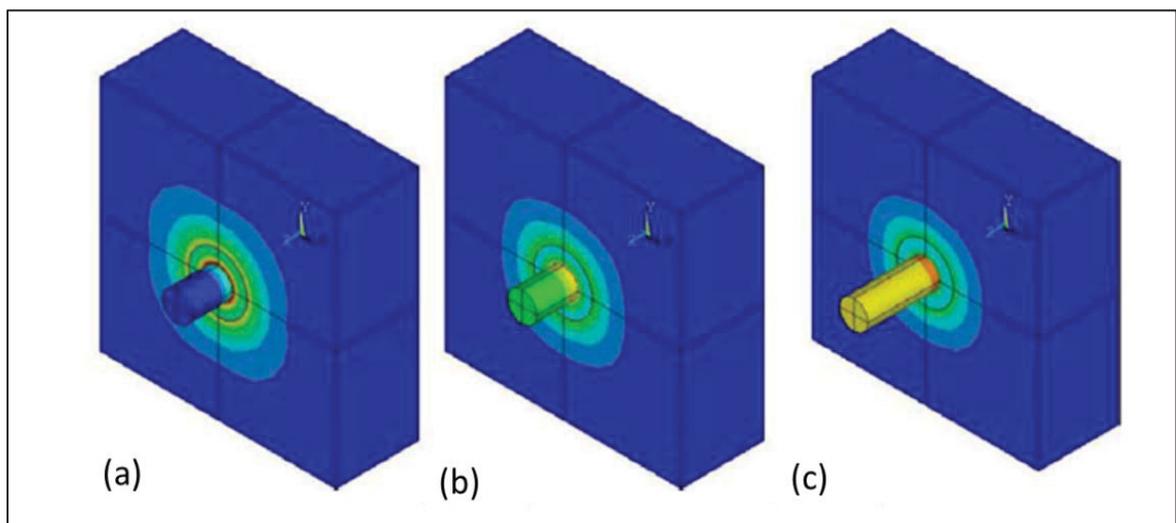
Figure 2.15 Snapshot of material deformation under tension: (a) elastic stretching, (b) initial debonding and (c) frictional sliding taken from Meo et al. (2005, p. 386)

Figure 2.16 shows that the representative tufted laminate for modelling comprises three distinct materials representing the laminate, matrix, and TTR. The laminate is 4 mm long and wide, with a height of 1.4 mm. The TTR is a cylinder with a radius of 0.25 mm and a height of 1.68 mm. The matrix area is assumed to be an empty cylinder with an external radius of 0.5 mm and an inner radius of 0.25 mm. The material properties of the matrix, TTR, and laminate are listed in Tables 2.4 and 2.5. While the article does not provide a detailed description of the laminate, it can be deduced from the material tables that the laminate is orthotropic, with equal

values for the longitudinal and transverse elastic moduli (*Ex=Ey*). Additionally, based on the available information, the tuft has twice the stiffness of the laminate.

Table 2.4 Properties of matrix and fiber taken from Meo et al. (2005, p. 384)

Properties	Matrix properties (isotropic)	Fiber properties (isotropic)
Young modulus, E_x	7.5 GPa	102 GPa
Poisson's ratio, v_{xy}	0.3	0.2

Table 2.5 Properties of laminate taken from Meo et al. (2005, p. 384)

Young modulus $E_x=E_y$ (GPa)	47
Young modulus E_Z (GPa)	14
Shear modulus $G_{xy}= G_{xz}$ (GPa)	6
Shear modulus, G_{yz} (GPa)	3.7
Poisson's ratio, $v_{xy}= v_{xz}$	0.25
Poisson's ratio, v_{yz}	0.45
Density p (kg/m^3)	1600
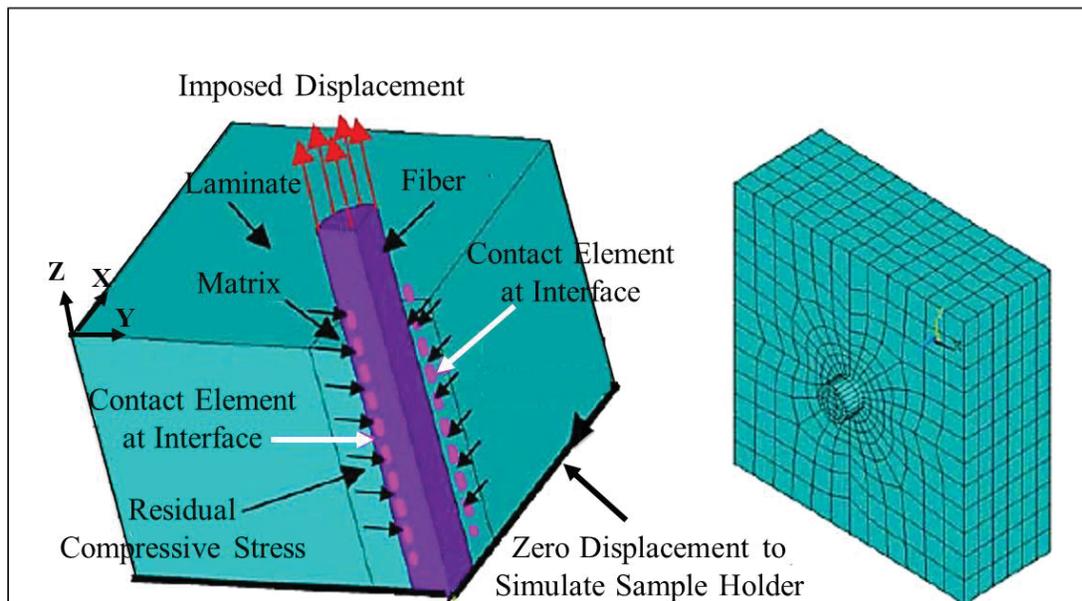
Figure 2.16 Finite element mesh and boundary condition taken from Meo et al. (2005, p. 384)

When a single TTR is pulled out, its propagation can be viewed as a frictional contact issue between the fiber and matrix. Therefore, in finite element simulation, contact elements are incorporated at the interface between the TTR and matrix. As shown in Figure 2.16, surface-to-surface contact elements are employed to depict the contact between the outer surface of the single tuft and the internal hole of the matrix. Furthermore, this figure illustrates the finite element (FE) model, which is composed of 810 elements. A displacement of 1.5 mm is applied in the z-direction to the top surface of the TTR in the simulation. The degrees of freedom at the bottom part of the entire structure is restricted in all directions. Equation 2.6 shows a connection between the maximum shear stress (τ_{max}), which is also known as the sticking shear stress, and the minimum shear stress that represents the sliding resistance (τ_{min}), along with the normal pressure (σ_n). As can be seen in this equation, a coulomb-type frictional coefficient (μ) is introduced at the contact surfaces. The values used for Equation 2.6 are depicted in Figure 2.17. The modeling results are compared to the load-displacement curve shown in Figure 2.18, obtained from the experiment. The graph illustrates that at the maximum load, complete debonding occurs, leading to a decrease in the pull-out force and subsequent frictional pull-out of the fiber.

Figure 2.19(a) depicts the impact of sliding resistance (τ_{min}) on the pull-out mechanism of TTR under zero normal pressure, revealing that increasing τ_{min} results in larger peak force and debonding area. Moreover, figure 2.19(b) shows that increasing the maximum shear stress (τ_{max}) leads to a rise in load-carrying capacity from 22N to 41N, representing 86% increase. Another important parameter investigated is the ratio of static to dynamic friction, which mainly impacts the peak load. This ratio has no effect on the linear and debonding response, as shown in Figure 2.19(c). Figure 2.19(d) illustrates the influence of the surrounding matrix stiffness (E_m) on the pull-out response. The findings indicate that a higher Young's modulus of the matrix can have a significant impact on the pull-out stiffness capacity and the extent of the debonding region.

$$\tau_{max} = \tau_{min} + \mu\sigma_n \qquad (2.6)$$
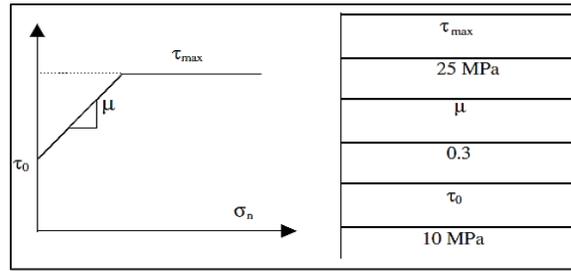
Figure 2.17 The Coulomb friction model for the debonded interface taken from Meo et al.
(2005, p. 385)
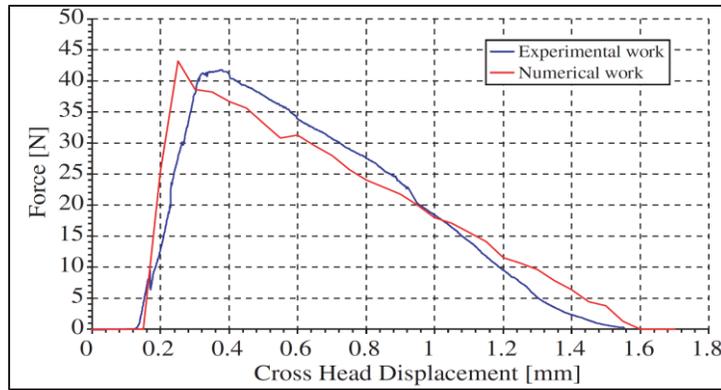
Figure 2.18 Comparison of experimental and numerical load-displacement response taken
from Meo et al. (2005, p. 385)
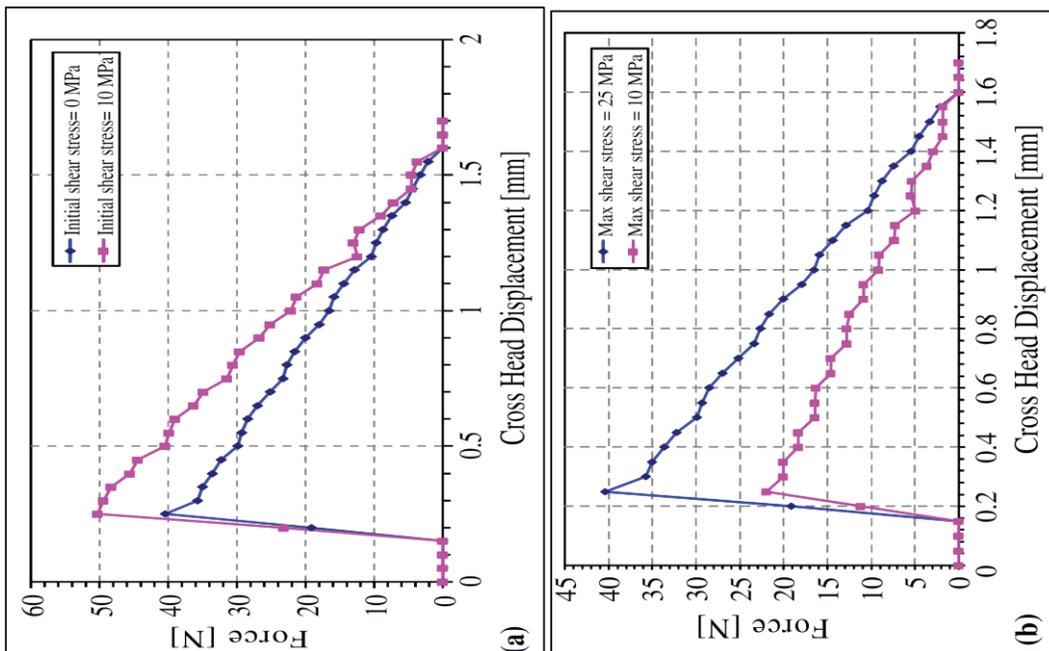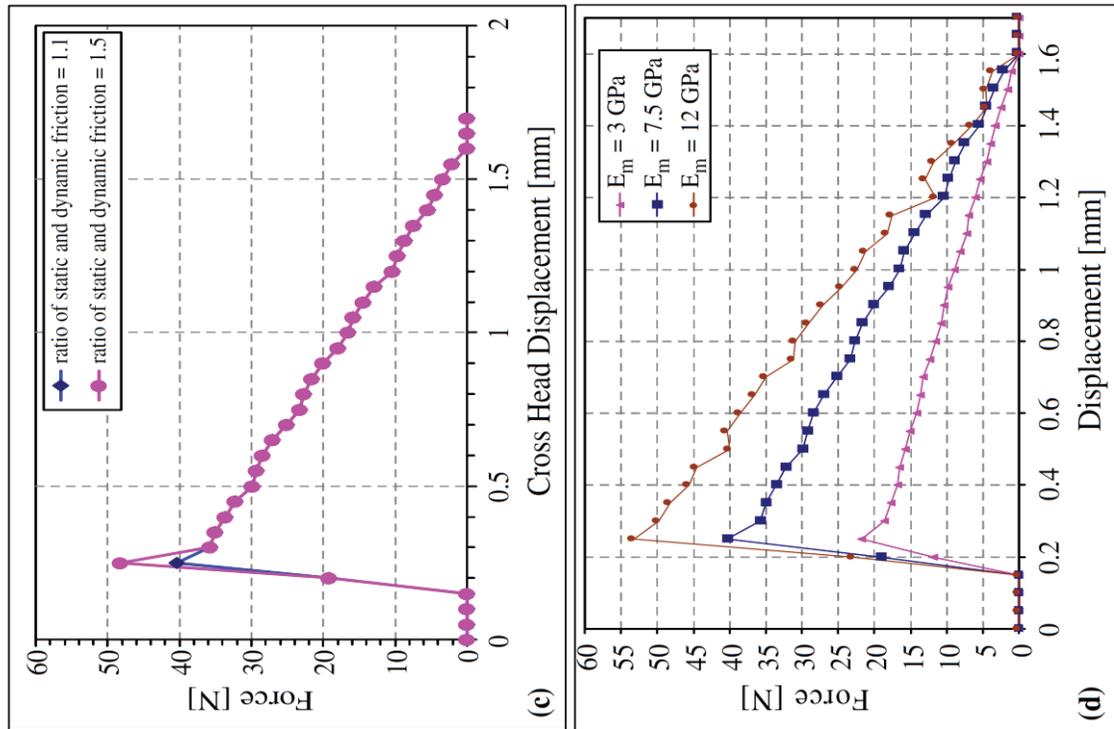
Figure 2.19 Parametric studies of mechanical properties on pull-out response: (a) influence of initial shear stress, (b) max shear stress, (c) ratio of static and dynamic friction and (d) matrix young's modulus taken from Meo et al. (2005, p. 386)

2.3.6   Meso-scale finite element modeling of DCB test

This work developed a micro-mechanical analytical model for a mode I delamination test on a tufted preform using LS-DYNA software (Osmiani et al., 2016). The DCB specimens' dimensions used in this study is shown in Figure 2.20(a). Tufts are inserted in a square pattern with a 5.6 mm × 5.6 mm space, resulting in a tuft areal density of 0.86%. The pattern is positioned at a distance of 15 mm from the end of the pre-crack, and the laminate had a thickness of 4.0 mm and a fiber volume fraction of 56%. The DCB model consists of four layers of biaxial carbon Non-Crimp Fabric (NCF) arranged in a symmetric [(0/90)] layup with a release film in the mid-plane for pre-crack (see Figure 2.20(b)). To prevent flexure failure, two unidirectional laminates of 10 layers of carbon fiber are bonded to both sides of the tufted preform.
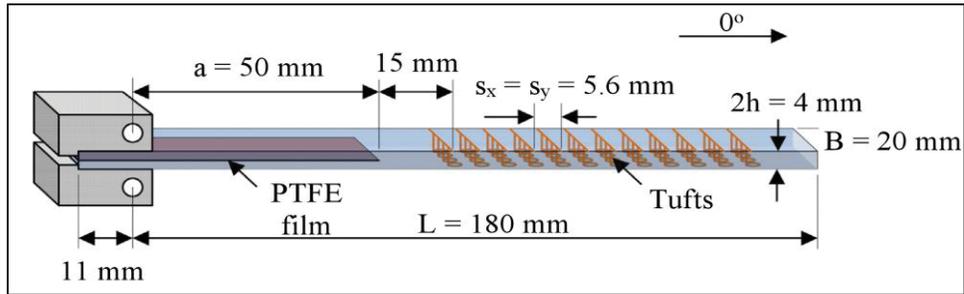
(a)
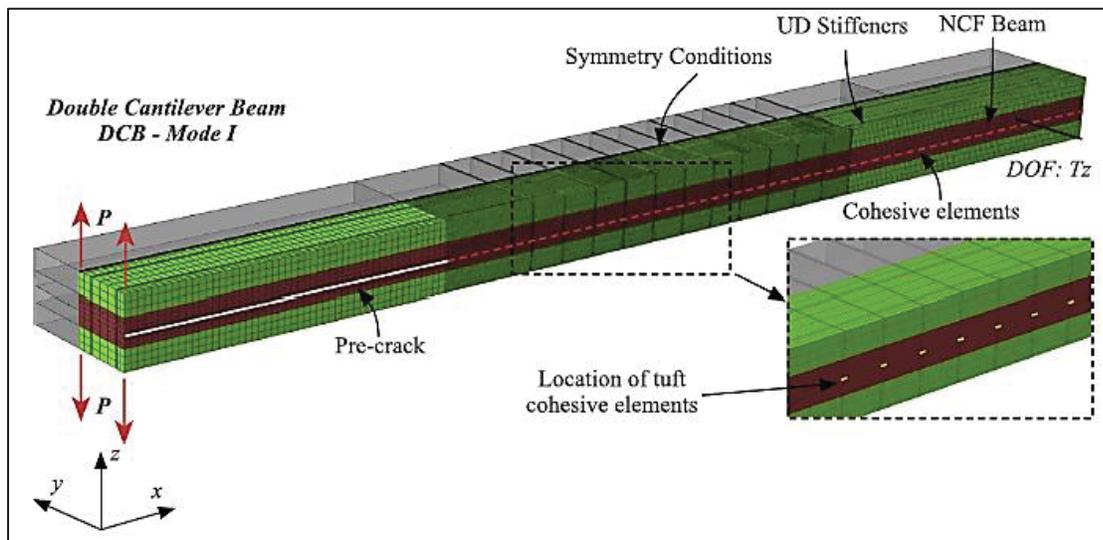
(b)

Figure 2.20 Finite element model of DCB simulation: (a) geometry and dimension and (b) detailed components simulation taken from Osmiani et al. (2016, p. 418)

The authors of the study used a modeling technique called cohesive modeling to simulate mode I delamination in composite laminates. This technique involved creating a cohesive zone and rigid elements that replicated the function of tow/ply bridging and tufts in the Double Cantilever Beam (DCB) (see Figure 2.20(b)). To model tufts, rigid elements are inserted perpendicular to the xz plane at the tuft locations in the simulation. Like in 2.4.1 section, the normalized traction-separation curve is required for both tuft and tow/ply bridging to model the delamination behavior of DCB laminates under mode I. The constitutive law for tuft and tow/ply bridging is shown in Figure 2.21. The mode I matrix fracture toughness value of tuft ($G_I^{C,tuft}$) and tow/ply ($G_I^{C,resin}$) bridging are 130.4 kJ/m^2 and 0.257 kJ/m^2 and respectively.

Furthermore, the maximum traction stress (σ_I^0) of 1020 MPa and 60 MPa are reported for tuft and tow/ply bridging.
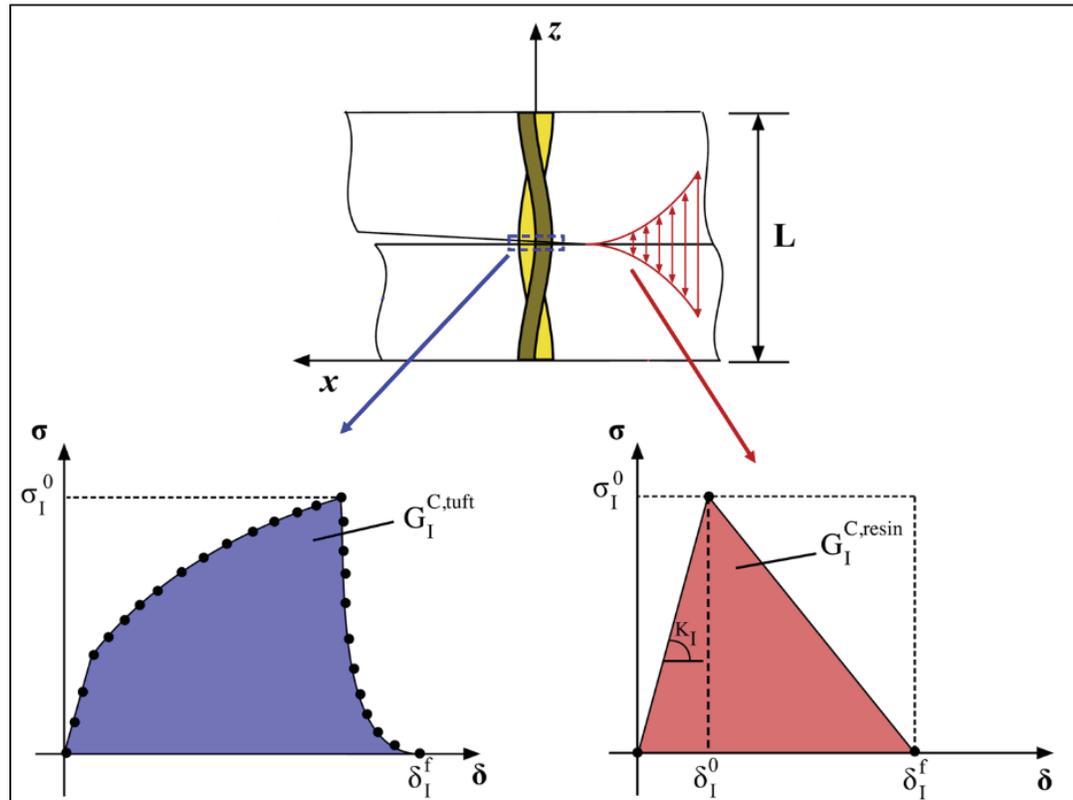
Figure 2.21 Traction-separation laws of localized tuft and of pure resin employed in cohesive elements taken from Osmiani et al. (2016, p. 417)

Figure 2.22 compares the predicted and experimental results of a DCB (Double Cantilever Beam) test, considering a tufted areal density of 0.86%. The numerical curve is obtained by implementing a calibrated analytical traction-separation law in the constitutive cohesive zone. Despite some slight underestimation in the saw-tooth pattern, the simulation aligns well with the experimental data. Moreover, the graph clearly demonstrates that the delamination initially propagates through the untufted region until it reaches the first row of tufts. At this point, the localized bridging effect of the tufts causes a significant increase in the load, reaching nearly 130%.
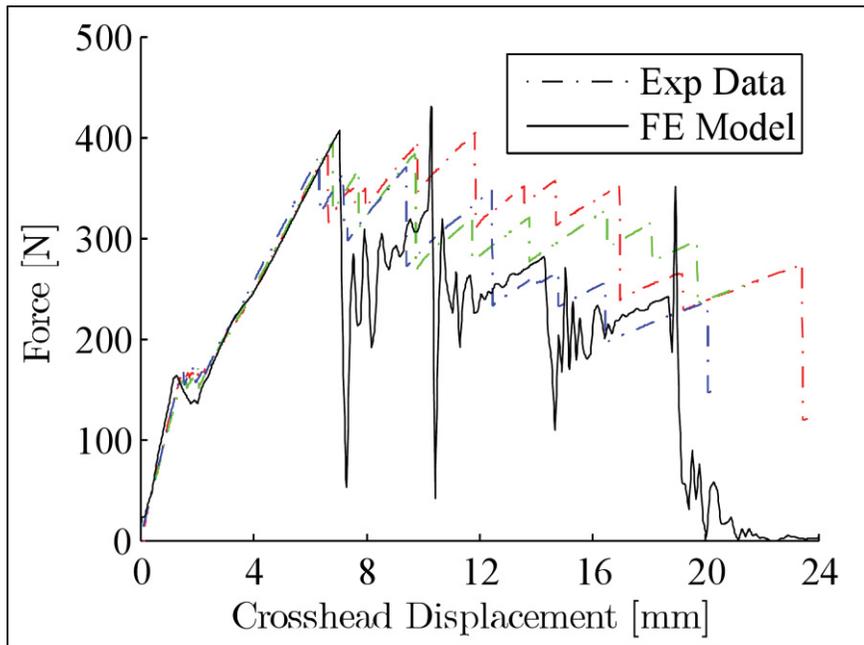
Figure 2.22 Comparison of FEM and DCB result in term of force-displacement curve taken from Osmiani et al. (2016, p. 418)

CHAPTER 3

METHODOLOGY

3.1   Introduction

Research methodology ensures that the study follows a systematic process, leading to reliable and valid results. A well-defined methodology allows the researchers to replicate the study, contributing to the advancement of knowledge in the field. Hence, this section describes the research methodology considered for this study to gather data relevant to the research objective. In this study, the experiments are specifically designed to gain a deeper understanding of how the laminates fail and to comprehend the underlying mechanisms responsible for these failures. First, this chapter primarily focuses on the manufacturing process of tufted laminates, with respect to different tufting geometries and stacking sequences for the laminates. Then a clear explanation of the setup for conducting tensile and CT-scan experiments is given.

3.2   Materials and specimens

3.2.1   Manufacturing tufted laminate

As mentioned earlier, the tufting technique is employed in this study to reinforce the laminates through the thickness. The tuft is a coiled 2 × 1k-67TEX Tenax® HTA-40 carbon fiber thread which is vertically inserted using a KSL (Keilmann Sondermaschinenbau GmbH) RS 522 tufting head (Pappas et al., 2018). As illustrated in Figure 3.1, the tufting head has two main parts: the needle and the pressure foot doing tufting together. According to microscopic images of a dry tuft, there is a complete twist every 4mm, which results in approximately 250 twists per meter (see Figure 3.2). The tuft coil angle is also measured to be 8.2 degree. Table 3.1 provides an overview of the main parameters of the tuft. These properties are employed to anticipate the mechanical characterization of tufts in the subsequent chapters.
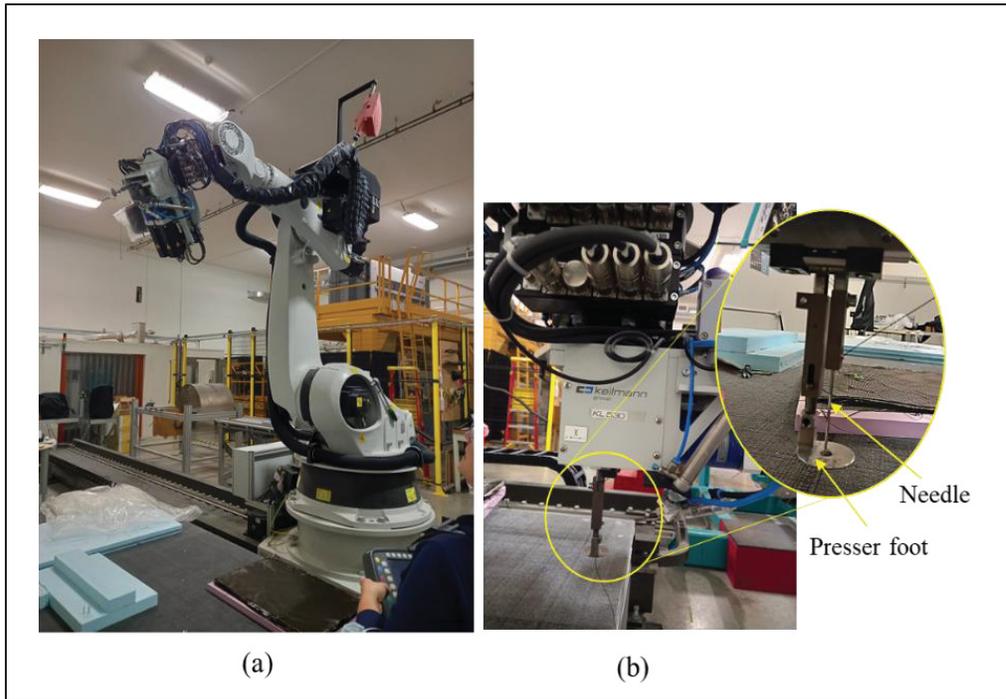
Figure 3.1 Tufting device components: (a) robots and (b) head (taken from CCT group)
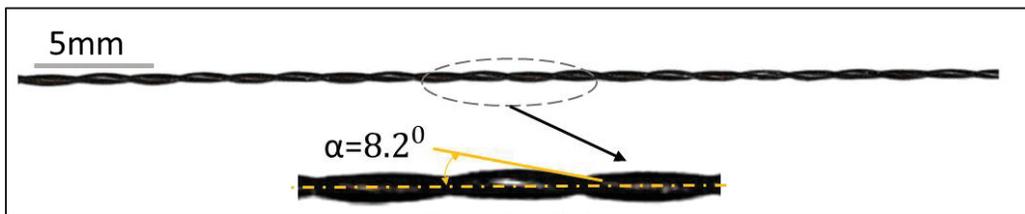
Figure 3.2 Microscopic view of a dry thread with two twisted yarns

Table 3.1 Main parameters of the tufting thread

Reference	Linear density (tex)	Number of filaments	Twist (T/m)	Coil angle (degree)
Tenax®-J HTA-40	2×67	2×1000	250	8.2

In the following, four 55×185 mm2 flat textile preforms are produced with twill 2/2 woven E-glass fabrics (TG-09-T (305 g/m2)) sourced from Texonic (see Figure 3.3). The tufting process is conducted by CTT GROUP, a textile research center situated in Québec, Canada. During the fabric layering procedure, a full-length release film is positioned at the mid-plane.

This arrangement is implemented to ensure that only the tuft plays a role in bearing the load when the laminates are subjected to tensile force. The tufted preforms are composed of 30 plies that are organized into either an orthotropic layup, with consecutive layers of 0° and 90°, or a quasi-isotropic layup, with consecutive layers of 0°, 90°, and ±45°. The arrangement of these plies can be seen in Figure 3.3. To produce small tufted specimens with dimensions of 10 mm × 10 mm, tufting points are uniformly distributed across the preforms. These points are spaced at a distance greater than 20 mm between each other ensuring an adequate spacing between tufts for cutting purposes.

Following the tufting process, the loops in the tufted preforms are trimmed down to a length of 2-3mm using a trimming device. This trimming step is performed to minimize any potential effect on the final thickness of the laminates. Figure 3.4 illustrates the resin infusion process used to impregnate and consolidate the preforms. Huntsman's Araldite® LY 8615/Aradur® 8615 epoxy, in a mass ratio of 100:50, is infused into the preforms at a temperature of 40°C (used epoxy data sheets, 2016). To ensure uniform thickness, facilitate proper resin flow, and minimize surface imperfections in the final laminate, a caul plate is employed on top of the preform (Pappas et al., 2018). A flow mesh and peel ply are utilized to help evenly distribute the resin throughout the preform and absorb any excess resin during the vacuum infusion process. After infusion, the tufted laminates are cured at 40°C for 24 hours, followed by post-curing at 180°C for 3 hours.

Figure 3.3 Layering processing of tufted orthotropic and quasi-isotropic laminates

Figure 3.4 Infusion processing

The process of creating loop-less specimens is illustrated in Figure 3.5. In this process, standard flat laminates are milled on both sides using a 3-axis CNC milling machine. The milling is done at a cutting speed of 180 m/min using a 4-flute, diamond-coated, solid carbide end-mill. The standard parts have a final thickness of 7.5 ± 0.5 mm, while the milled down parts have a reduced thickness of 6 ± 0.06 mm. After curing, the orthotropic and quasi-isotropic laminates are cut into desired cross-sections, each containing a single tuft through the thickness with respect to different tufting geometries (see Figure 3.6). This cutting process is accomplished using a diamond-coated disk saw.
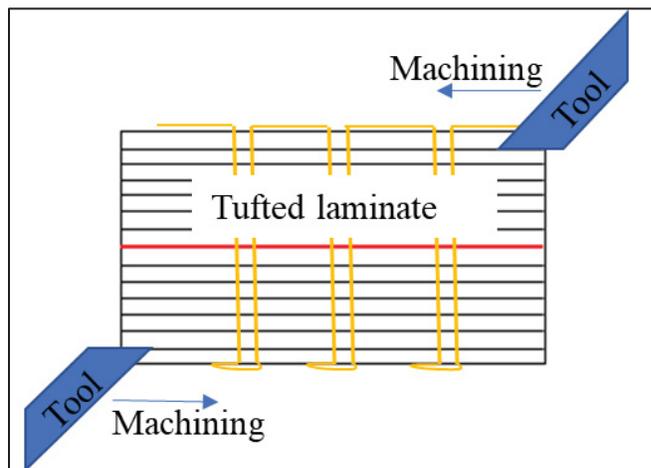
Figure 3.5 Milling-down of the tufted laminate
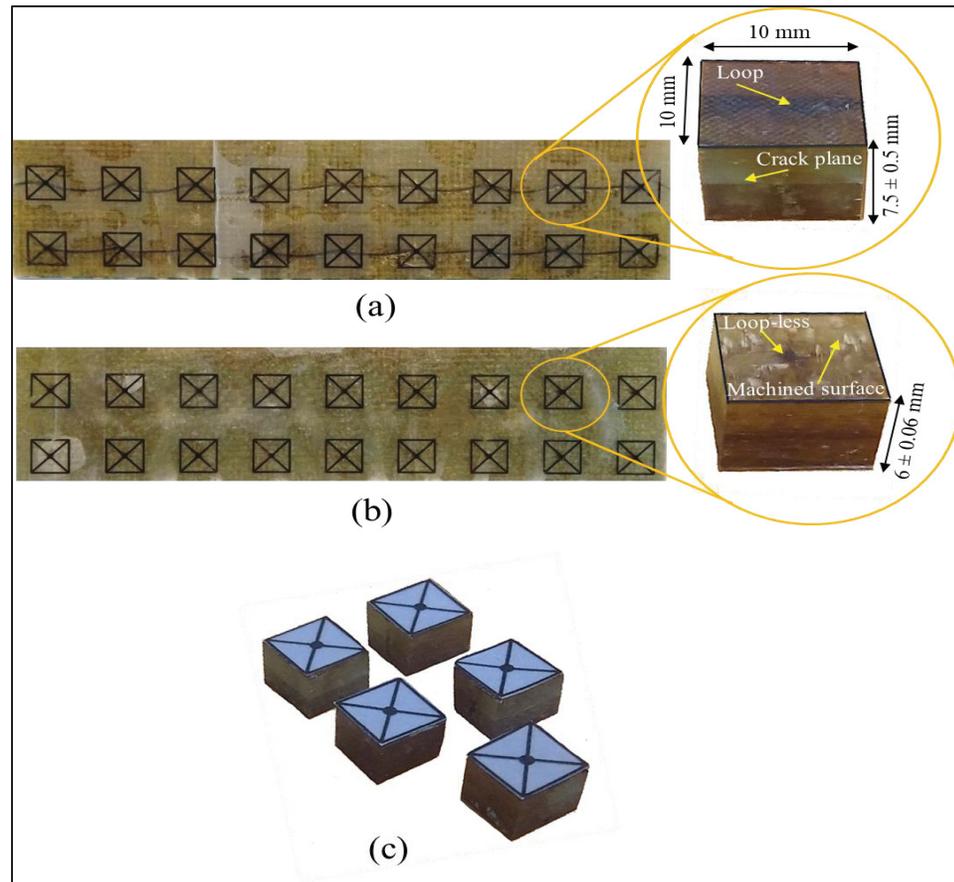
Figure 3.6 Tufted laminate plate with (a) loop and (b) loop-less tufting geometry and (c) tensile test specimens

3.2.2 Specimen nomenclature

Table 3.2 provides a summary of the sample classifications based on tufting geometry, laminate sequences, and the number of specimens required for pulling experiments and CT scan analysis. The specimens are identified with the labels S-ortho, M-ortho, S-iso, and M-iso. The terms "ortho" and "iso" are assigned to represent the two different laminate stacking sequences used in this study. The prefixes "S" and "M" in the sample labels refer to the two different tufting geometries, specifically standard or milled-down. As stated in Table 3.2, within each category, four samples are prepared specifically for tensile tests, while three samples reserved for CT scanned experiments. This allocation ensures that an adequate number of samples are available for both types of analyses, allowing for a comprehensive investigation of failure mechanisms in tufted laminates.

46

Table 3.2 Tufted specimen description and nomenclature

Name	Number of tests	Nomenclature		
S-ortho	4 (Tensile test) 3 (CT scan)	**Tufting Geometry** S: Standard samples		M: Milled down samples
M-ortho	4 (Tensile test) 3 (CT scan)	X -Y-Z	Test number **Laminate type**	
S-iso	4 (Tensile test) 3 (CT scan)	ortho: Orthotropic laminate sequences of 0/90		0/90 0/90
M-iso	4(Tensile test) 3 (CT scan)	iso: Isotropic laminate sequences of 0/90 with ±45		0/90 ±45
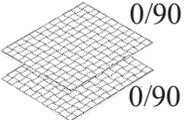
3.3　Tensile experiment set-up

The primary aim of conducting tensile experiments is to initially assess the failure mechanisms in TTR composites. The results obtained from the tensile tests are also utilized for microstructural failure analysis using CT scans and to support finite element modeling. This section provides a detailed description of the methodology employed for conducting uniaxial pulling tests using a tensile machine equipped with a 5 kN load cell. The tests are carried out under quasi-static conditions with displacement control, applying a constant rate of 0.5 mm/min (Pappas et al., 2017). Figure 3.7(a) illustrates the setup for the pulling tests, where two opposing aluminum T-shape supports are mounted on the tensile machine. These supports play a crucial role in maintaining the proper alignment during the tension test and preventing any bending issues. By ensuring the correct alignment of the supports, the accuracy of the pulling tests is preserved, allowing for reliable results. Using a positioning jig (as shown in Figure 3.7(b)), the samples are firmly affixed to the centers of two aluminum T supports using glue (epoxy paste adhesive syringe glue 25 mL). This method involves applying the adhesive to one of the aluminum supports mounted on the tensile test machine and allowing it to cure.

Following that, adhesive is applied to the opposite surface of the sample, and the upper aluminum support is gradually lowered until a force of 10 N is applied. The assembly is then allowed to cure for 15 minutes before testing. Fig. 3.7(c) shows a tensile test conducted on a tufted laminate, displaying the separation of the tuft. Before performing the tensile tests, three tufted samples without release films are also loaded in tension to estimate and deduct the compliance of the testing setup to obtain accurate tuft stiffness properties. Figure 3.8 illustrates the force-displacement diagram, which presents the failure of the adhesive from either the top or bottom of the specimens without a release film in the middle. The adhesive and tensile setup rigidity is determined to be K=4497 N/mm. To calculate the real displacement causing the laminate opening at crack plane, Equation 3.1 is employed in this study (Pappas et al., 2017). The letter "F" and "D" in this equation refer to the force-displacement curve values obtained directly from the tensile machine during the experiment, while D' and K represent the laminate opening displacement at mid-plane and adhesive rigidity respectively. The number '2' is coming from top and bottom moveable parts connected to laminates.

$$D' = D - 2 \times \frac{F}{K} \qquad (3.1)$$
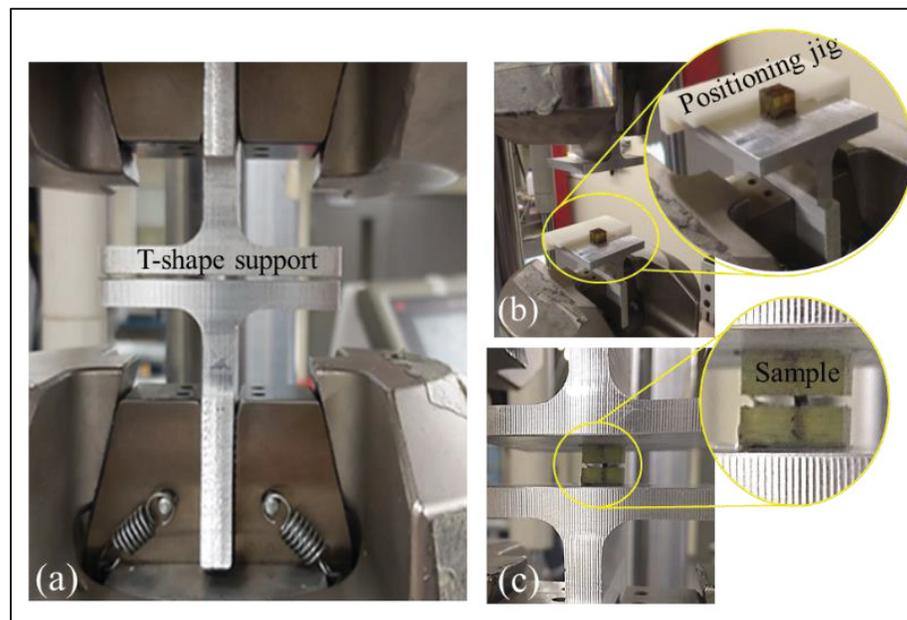
Figure 3.7 Preparation of tensile experiments: (a) parallel mounting of aluminum supports, (b) mounting the specimens on the tensile machine and (c) tensile experiment
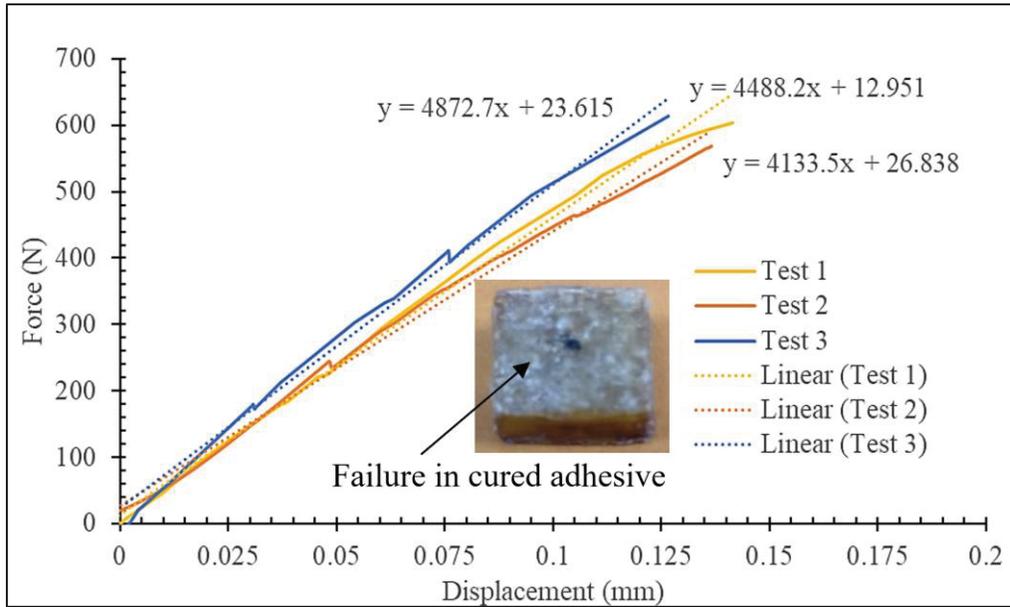
Figure 3.8 Force-displacement response for the laminate without release film

3.4   Tensile jig for CT-scan

To examine the failure mechanisms of the designated specimens during tension testing, a specialized tensile jig is employed to apply incremental displacement to the laminate positioned within the CT-scan device. This configuration enables the observation and analysis of the specimens' behavior and failure progression under tension. The tensile jig used in this study, depicted in Figure 3.9, consisting of two plastic T-shaped components that firmly hold the samples in place with adhesive. The setup uses four plastic bolts (M5-0.8-25mm) that are tightly fastened through the threads of the T-shaped components. By precisely adjusting these bolts to a specific position, the upper T-shaped component can be raised, resulting in different tensile displacements applied to the pre-crack layer of the samples. This enables controlled and incremental displacement during the tension test. To avoid any bending issues, it is important to measure and ensure that the distances between the T-shaped components on all four sides are equal using a caliper before and after each increment displacement. It is worth noting that the process of applying displacement and measuring it on the jig takes place externally to the CT-scan device. Different incremental tensile displacements corresponding different locations

on the force-displacement diagrams discussed in next chapter are applied to the tufted laminates with the designed CT-scan tensile jig. These displacements are outlined in Table 3.3.
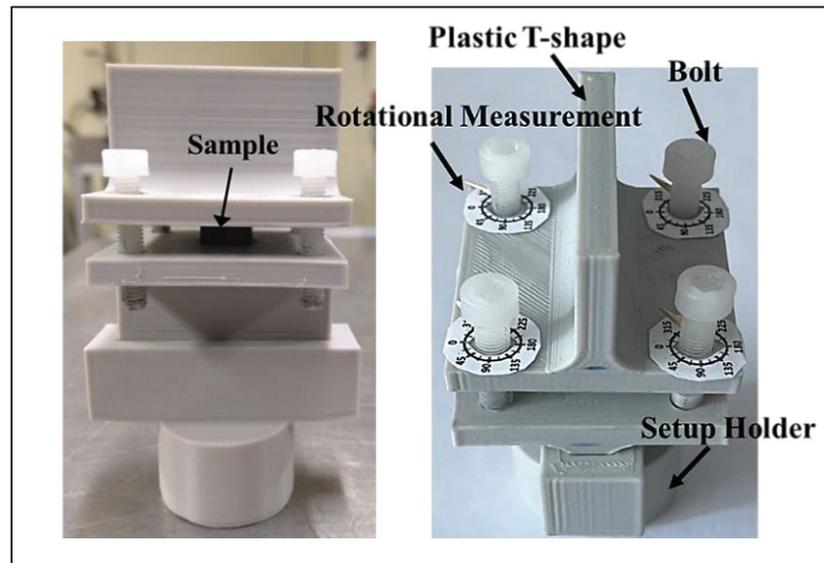
Figure 3.9 CT-scan jig for applying the incremental displacements

Table 3.3 Incremental displacement for the all type of specimens under study

Sample	O	0-A	A-B	B-C	C-D
S-ortho	0	0.025	0.1	0.30	0.60
S-iso	0	0.025	0.1	0.25	-
M-ortho	0	0.025	0.1	0.45	2.80
M-iso	0	0.025	0.1	0.40	2.50

3.5   Image processing and measurement tool of CT-scan pictures

In this study, image processing techniques are utilized to enhance the clarity of the CT-scan pictures. The objective is to improve the visibility of different components within the laminates, including glass fibers, tufts, epoxy, and voids. To achieve this, the dragonfly and 3D CT-pro software are employed. These software applications assist in precisely recognizing and differentiating various components of interest by employing threshold techniques to identify distinct components according to their density. Additionally, the measurement of geometrical parameters on the CT-scan pictures is performed using the ImageJ software.

3.6 Minimizing the number of voids within the laminate

Figure 3.10 demonstrates the distribution of voids within the laminate, particularly in the zone of interest, which includes the tuft and interface (highlighted in red). In order to mitigate the impact of voids on the mechanical properties and ensure the integrity of composite parts, and CT-scan is conducted to classify samples based on the void content within the zone of interest. The purpose of this CT-scan is to obtain a detailed internal image of the composite sample, allowing for the identification and quantification of voids within the specific zone of interest. By analyzing the CT-scan results, the samples can be categorized according to the voids volume fraction. Therefore, prior to conducting the tensile test, the samples are positioned on the CT-scan holder, as depicted in Figure 3.11, to evaluate the void content and select samples with almost same void contents. For estimating the rough proportion of voids volume within a laminated structure, a cylindrical section with a 1mm diameter located in the center of the laminate is predominantly examined. This section encompasses voids, tuft, and resin. Through the application of a thresholding technique, the voids are isolated and their quantity is measured to fall within the range of 4% to 8% within the specified cylindrical segment.
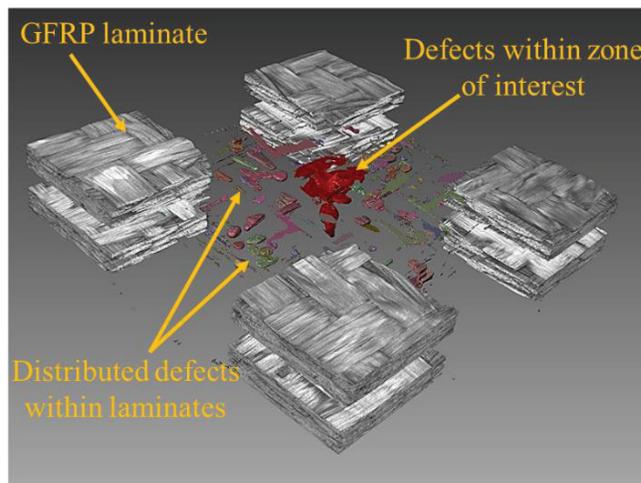
Figure 3.10 Distributed defects within the tufted laminates
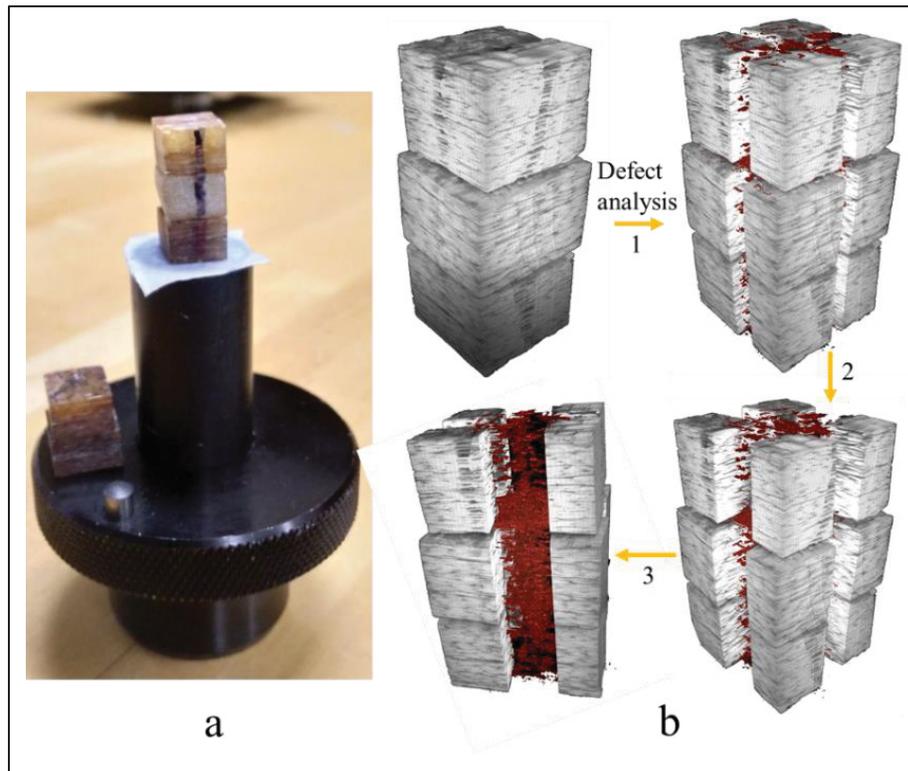
Figure 3.11 CT-scan performing on the samples before failure: (a) mounting the samples on the CT-scan holders and (b) defect analysis (1 to 3)

CHAPTER 4

EXPERIMENTAL INVESTIGATION OF FAILURE MECHANISM IN TUFTED LAMINATES SUBJECTED TO TENSILE LOADING

4.1   Introduction

This section focuses on the analysis of failure mechanisms in tufted laminates with regards to varying tufting geometries and laminate sequences. First, the fractured surface and force-displacement results obtained from tensile tests are analyzed to evaluate the impact of these factors on the failure mechanisms of tufted laminates. To further support these initial findings, the CT-scan technique is utilized to gain a deeper understanding of how tufted laminates react to failure under tension. This provides a more comprehensive explanation of the force-displacement behavior observed in both linear and nonlinear regimes, considering several primary failure mechanisms such as interface debonding and failure, inter-fiber debonding, tuft rupturing, tuft complete failure, and pulling out. Additionally, the outcomes of this chapter help in determining the most suitable tufted laminates for elastic and plastic regimes, considering different tufting geometries and laminate sequences.

4.2   Tensile experiment results

4.2.1   Fractured surface analysis

Figure 4.1(a-d) displays the fractured surfaces of the specimens that are described in Table 3.2. The findings emphasize the tuft pullout phenomenon that is observed in the damaged laminates. The extent of fiber pull-out length differs based on the type of laminates and the tufting geometry employed. In Figure 4.1(a), S-ortho (orthotropic layup) specimens depict the tuft failing inside the composite with a relatively small amount of pull-out. In contrast, for S-iso (quasi-isotropic layup) specimens (Figure 4.1(c)), the tuft fractures directly at mid-plane. As shown in Figures 4.1(b) and 4.1(d), loop-less specimens are more prone to complete tuft pullout from the laminates instead of breaking inside the composites.
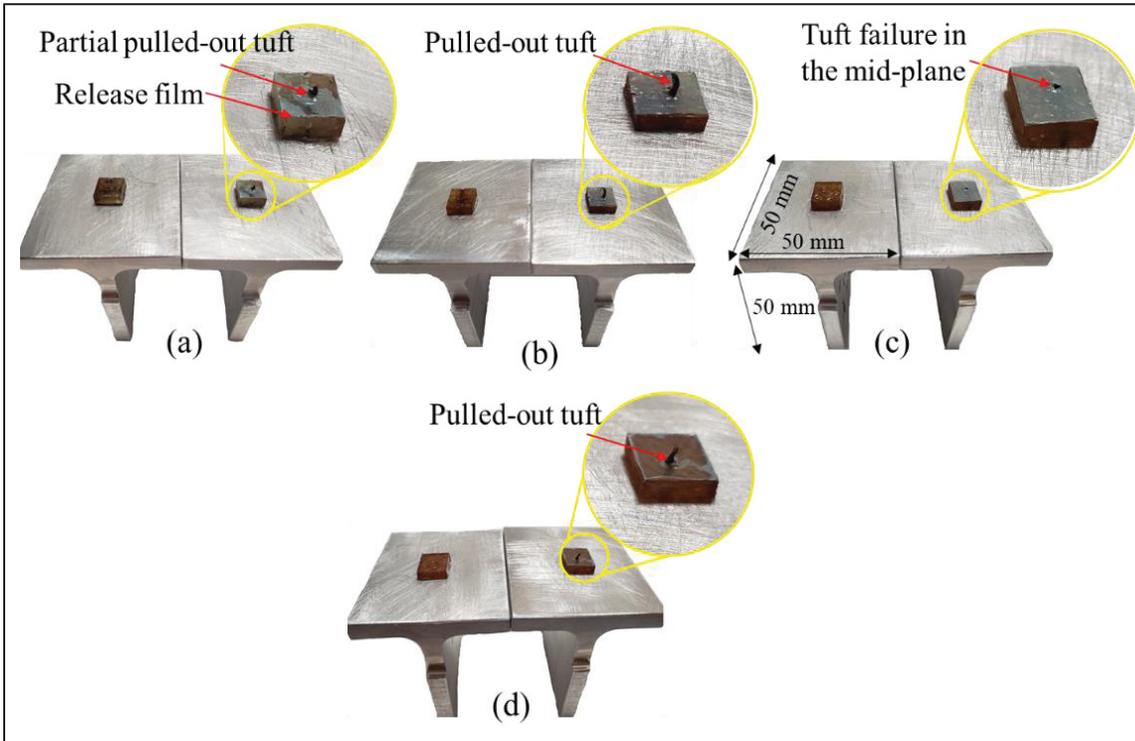
Figure 4.1 Mid-surface fracture morphology of tufted laminates: (a) S-ortho, (b) M-ortho, (c) S-iso and (d) M-iso

4.2.2   Force-separation response

Figures 4.2 and 4.3 depict the force-separation diagrams derived from the pulling tests conducted on the laminate with different tufting geometry and laminate sequences (see Figure 3.7 for test setup). To provide a comprehensive overview of the force-separation behavior, average approximate curves are included for each type of sample. To accomplish this, interpolation techniques are implemented using the MATLAB software with 2000 displacement points. However, due to the numerous minor fluctuations present in the average curve generated by these techniques, which aim to predict the entirety of the experimental error range, the number of displacement points was reduced to 50 to ensure a smooth overall appearance of the curve. Based on force-separation response, the diagrams are divided into four sections (*OA*, *AB*, *BC*, and *CD*), each associated with specific failure mechanisms observed within the specimens [Pappas et al., 2017]. A general observation of Figure 4.2n and

Figure 4.3 shows that the tufting loops and laminate sequences clearly influence the failure mechanisms in the laminates along the defined sections of the *OD* path. Figure 4.2(a) displays the force- displacement curves of the standard tufted orthotropic laminate (S-ortho). During the *OA* path, the tuft exhibits an elastic behavior followed by different slope of AB before reaching its maximum tensile strength at point B. Subsequently, the tuft's stress significantly decreases during the *BC* route, followed by a moderate reduction until point *D*, where the tuft becomes completely detached from the composite. The *OB* path is almost identical for both tuft geometries, with and without loops, except for the maximum load value at point B, as illustrated in Figure 4.2(a) and (b). Hence, the standard tufted laminates exhibit a slightly higher ultimate tuft strength compared to the loop-less tufted laminates.

The presence of loops primarily impacts the nonlinear force-separation behavior during the *B* to *D* path. As shown in Figure 4.2(b), the M-ortho specimen experiences a smaller decrease in slope after point B compared to the S-ortho specimens. This disparity can be attributed to the occurrence of pulling-out phenomena within the loop-less specimens, which significantly enhances the fracture energy. The complete separation of the tuft takes place at a greater tensile displacement at point *D* in the M-ortho specimens (2.8 mm) compared to the S-ortho specimens (1.27 mm).
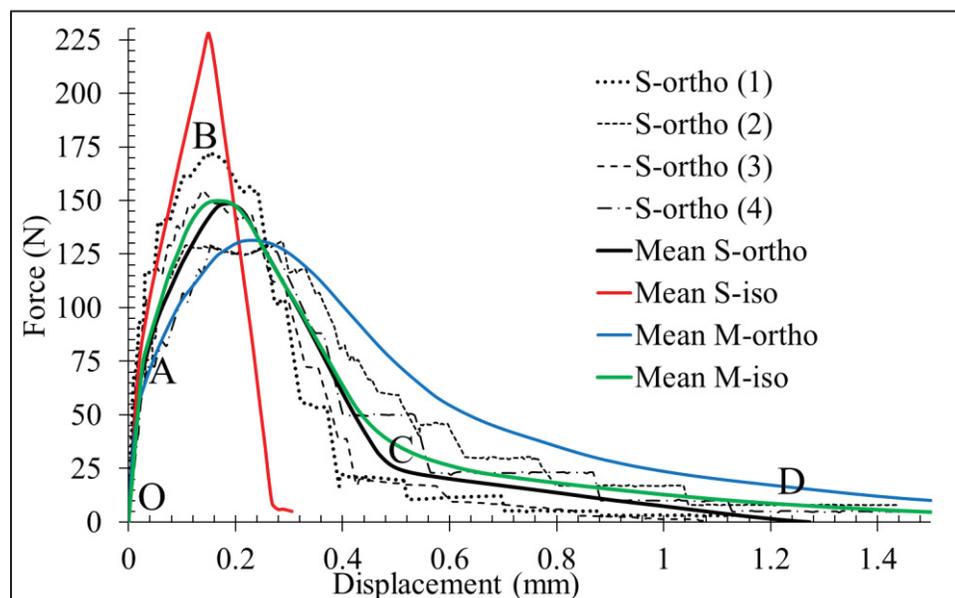
(a)
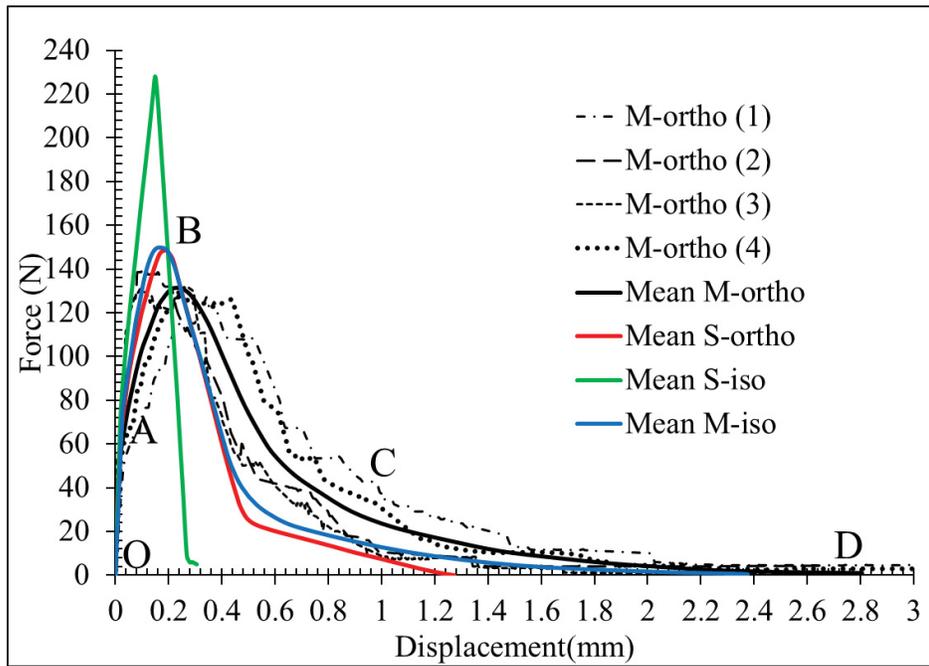
(b)

Figure 4.2 Force-displacement curve of (a) S-ortho and (b) M-ortho laminates

Based on the mean curves of the two different laminate types shown in Figure 4.3(a), the S-iso specimens exhibit higher tuft stiffness and ultimate strength in comparison to the S-ortho specimens. Following point *B*, the S-iso diagram demonstrates a sharp reduction in force until point *C*, where the tuft fails completely almost in the middle of laminates (as shown in Figure 4.1(c)). Due to the tuft breaking relatively close to the pre-crack layer, there is small tuft pulled-out observed in S-iso laminates.

As a result, changing the laminate type to S-iso leads to a lower fracture toughness compared to S-ortho laminates. Similar to orthotropic specimens, changing the tufting geometry from standard to loop-less enhances the fracture energy in quasi-isotropic laminates, as can be observed by comparing Figures 4.3(a) and 4.3(b). Furthermore, the rightward shift of the average curve between points *B* and *D* in M-ortho specimens is explained by more tuft pulling in M-ortho samples resulting in more damage dissipation compared to M-iso samples.
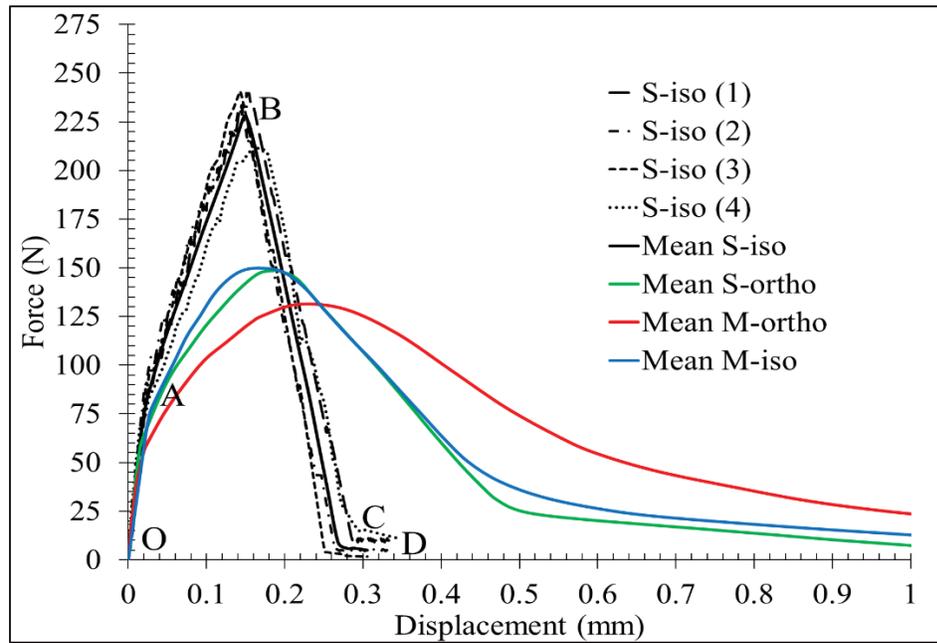
(a)
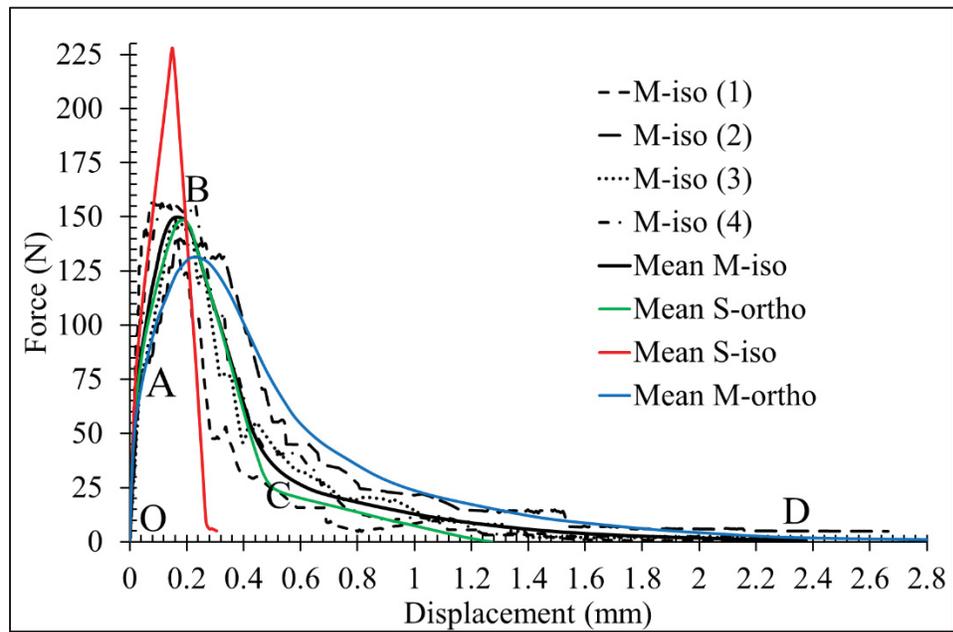
(b)

Figure 4.3 Force-displacement curve of (a) S-iso and (b) M-iso laminates

4.3 CT-Scan results on failure mechanisms of tufted laminates under tension

4.3.1 Failure mechanism in with-loop tufted orthotropic laminates (S-ortho)

Figure 4.4 presents CT scan images within the S-ortho laminate at different levels of tensile displacements. In order to analyze the failure mechanisms in tufted laminates during tension, a vertical cross-section plane is employed to provide a clear side view of the tuft within the laminate at various levels of tensile displacements (as depicted in Figure 4.4(a-e)). At zero displacement (Figure 4.4(a)), various components of the TTR laminate are illustrated, including the glass fiber, epoxy, tuft, voids, and pre-crack. Figure 4.4(b) demonstrates that when a displacement of 0.025 mm is applied, no changes occur in the tufted sample until the end of point A. After point A, inter-fiber and interface debonding initiate within and around the tuft, as depicted in Figure 4.4(c). This corresponds to the changes in slope between the OA and AB lines on the force-displacement curves. As shown in Figure 4.4(d), the interface failure propagates from points B to C, resulting in more damages and rupturing in the tuft and its interface to occur. At point C, the interface degradation and tuft rupture are almost completed, enabling the tuft to be extracted from the composite material (Figure 4.4(e)). This tuft pulling out is accompanied by the breaking of any remaining intact interface and tuft fibers within the composite. It is worth to mention that during the extraction of the tuft from the sample, the pull-out force leads to minor localized interlaminar delamination in the layered epoxy.

4.3.2 Failure mechanism in with-loop tufted quasi-isotropic laminates (S-iso)

The microscopic failure analysis of S-iso laminate is depicted in Figure 4.5. At unloaded state (displacement = 0), the various components within the S-iso laminates are recognized (see Figure 4.5(a)). During the elastic linear segment, as illustrated in Figure 4.5(b), no noticeable changes in the fracture mechanism are observed, and the structure remains in a stable phase. Figure 4.5(c) demonstrates the failure behavior of the tufted laminate during the AB path at a tensile displacement of 0.1 mm. In this path, the interface initiates debonding within the laminate. Additionally, two twisted threads in the tuft start to move, enabling inter-tuft debonding phenomena to occur up to point B, where the ultimate tuft bearing load is reached.

During the *BC* route, as the tuft starts to rupture specifically in the middle area of the laminate, catastrophic rupturing eventually occurs (see Figure 4.5(c)).
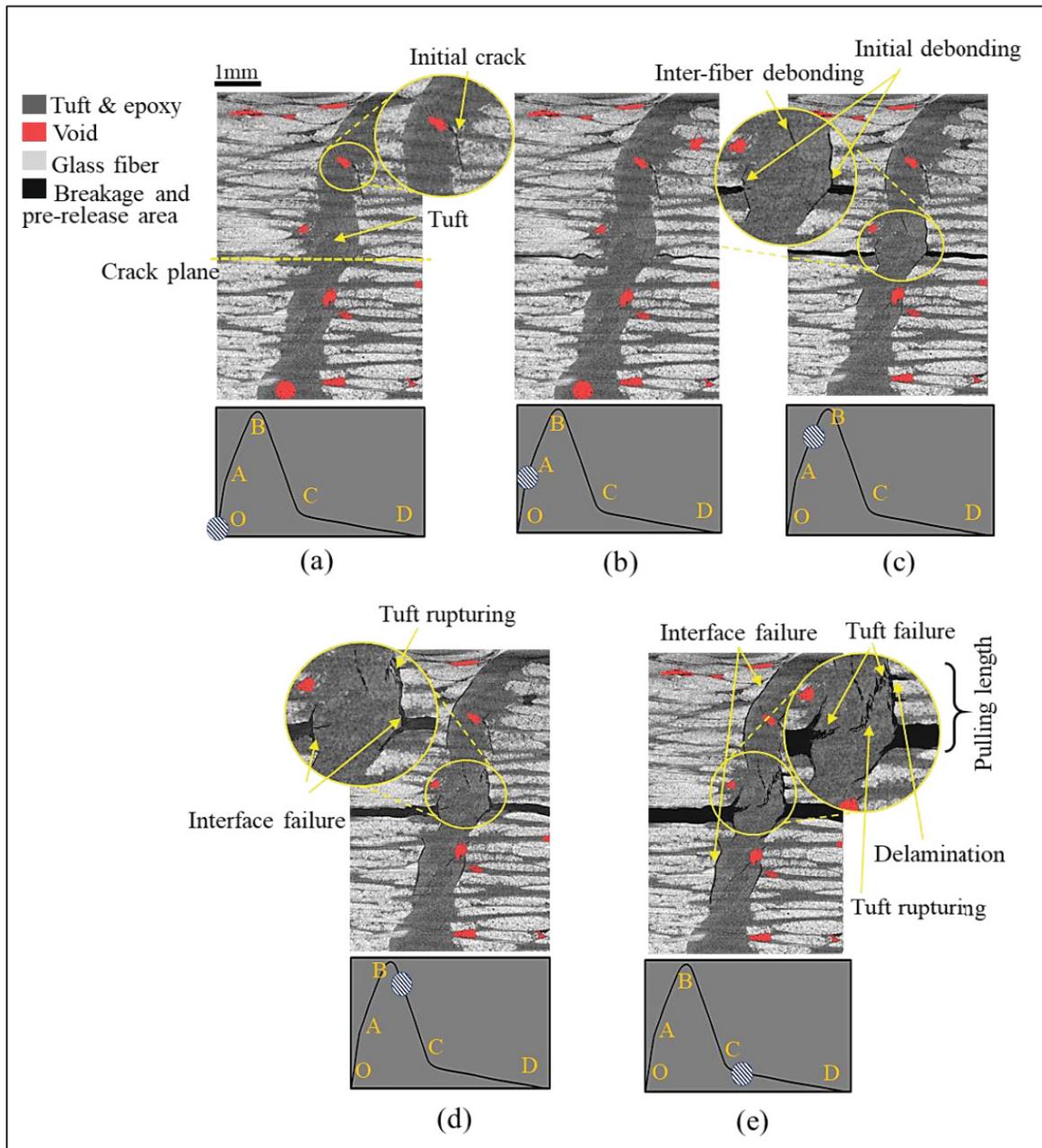
Figure 4.4 CT-scan images of S-ortho at different tensile displacements: (a) zero, (b) 0.025 mm, (c) 0.1 mm, (d) 0.3 mm and (e) 0.6 mm

60

Figure 4.6 and Figure 4.7 show the CT-scan top cross-sectional views of the tufted orthotropic and quasi-isotropic laminates at different heights through the thickness, specifically at 5.2 mm, 3.6 mm, and 2.1 mm. As shown in these figures, there is a significant thickness of epoxy surrounding the tuft in orthotropic laminate at various heights compared to quasi-isotropic in which the tufts are well maintained in laminate with a tiny layer of epoxy around the tuft. The large epoxy thickness around the tuft in orthotropic laminate is attributed to the sizable gaps created by the tufts during their insertion into the dry 0/90 twill preforms. These gaps are subsequently filled with epoxy during the later stage of infusion. The greater amount of epoxy present in the S-ortho laminates accounts for reduction in material stiffness compared to S-iso laminates. Additionally, the existence of a resin-rich pocket surrounding the tuft in S-ortho laminates results in slower and more extensive matrix damages around the tuft area. This considerable pocket provides a pathway for damage propagation and dissipation, explaining the higher level of damage dissipation observed in S-ortho specimens compared to S-iso specimens.

4.3.3   Failure mechanism in loop-less tufted orthotropic and quasi-isotropic laminates (M-ortho and M-iso)

Figures 4.8(a) and (b) provide a schematic comparison of tufting geometries with and without loops and their impact on the failure behavior of tufted laminates under tension. In Figure 4.8(a), the loops offer enhanced anchoring of the tufts at the top and bottom of the laminate free surfaces, resulting in the tuft to withstand loads during the elastic phase followed by higher ultimate load bearing capacity, as demonstrated by the force-separation responds which discussed earlier. When loops are absent in the tufting geometry, as depicted in Figure 4.8(b), the tufts are not anchored at the laminate free surfaces. This lack of anchoring allows for shear forces to be activated on the loop-less tuft surfaces along their helical paths, facilitating easier tuft pull-out [Pappas et al., 2017]. In contrast, tufts with loops experience pure tension due to the tight holding by the loops. This distinction is illustrated by the red arrows as loading directions in Figure 4.8(a) and (b). Based on these findings, it can be inferred that in loop-less tufted laminates, point *B* corresponds to the ultimate shear strength of the interface, whereas

in tufted laminates with loops, point *B* represents the ultimate tensile strength of the tuft. The subsequent microstructural failure analysis provides strong support for this hypothesis.
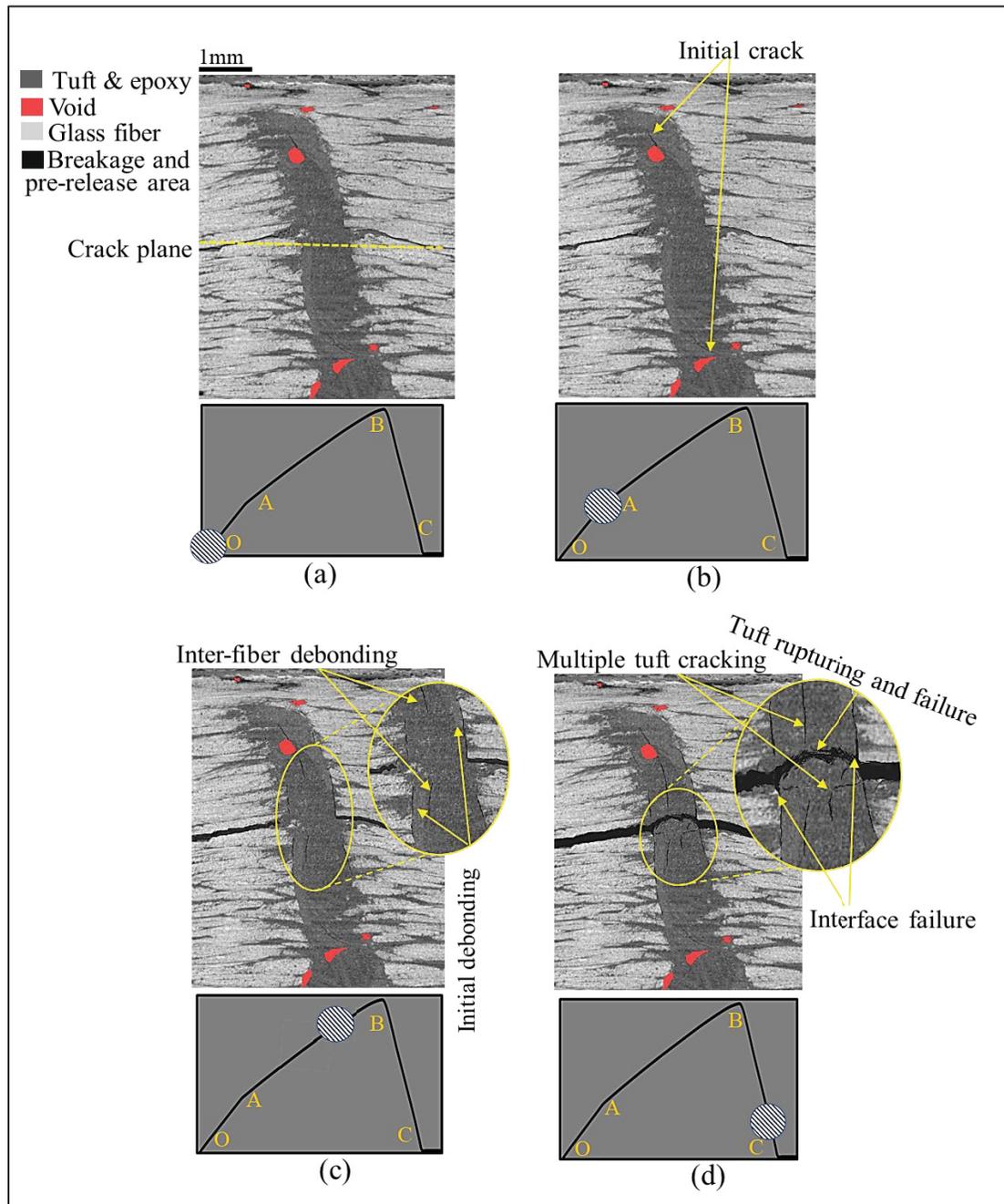

Figure 4.5 CT-scan images of S-iso at different tensile displacements: (a) zero, (b) 0.025 mm, (c) 0.1 mm and (d) 0.26 mm
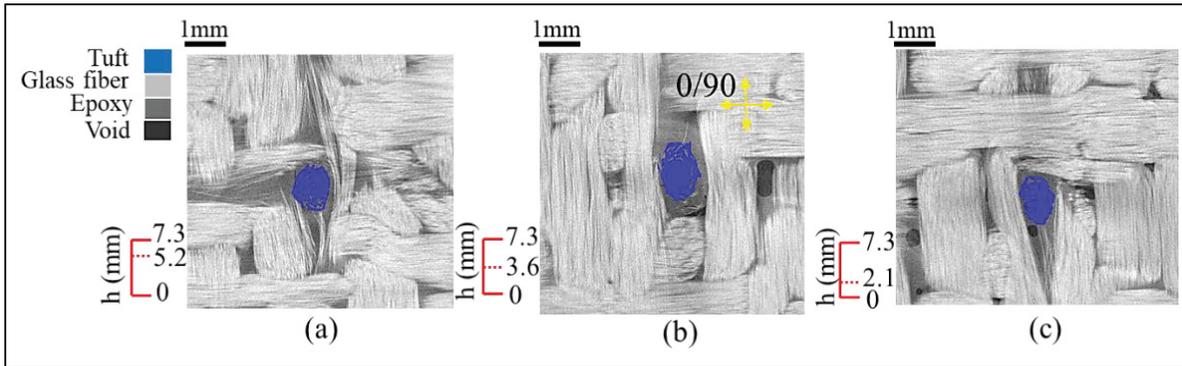
Figure 4.6 Top cross-view section of S-ortho at different heights: (a) 5.2 mm, (b) 3.6 mm and (c) 2.1 mm
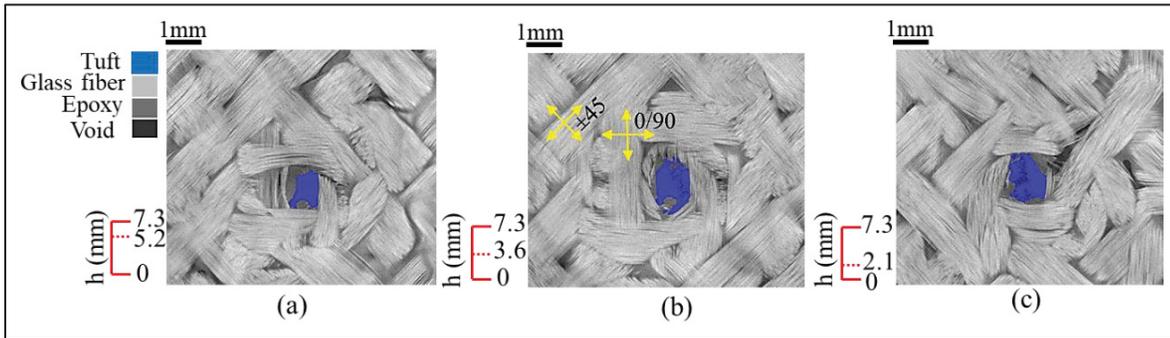
Figure 4.7 Top cross view section of S-iso from different heights: (a) 5.2 mm, (b) 3.6 mm and (c) 2.1 mm
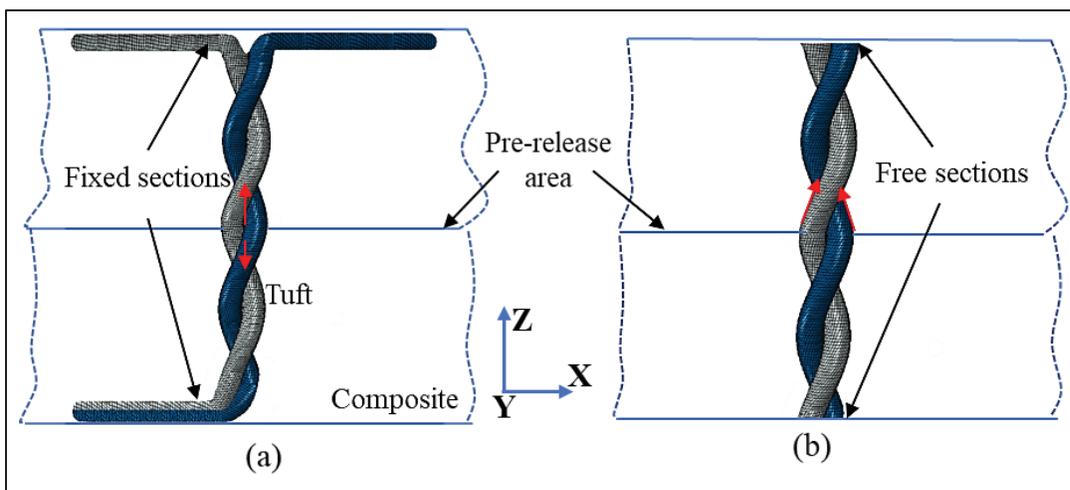
Figure 4.8 Effect of tufting geometry on loading direction (red arrows) of tufted laminate: (a) with loop and (b) loop-less geometry

Figures 4.9 and 4.10 provide CT scan results depicting the progressive failure mechanisms of M-ortho and M-iso laminates at different levels of tensile displacement. Similar to with loops tuft, when M-ortho laminate undergoes a 0.025 mm tensile displacement, no notable changes are reported under elastic strain (Figures 4.9(a)-(b)). However, as the displacement increases to 0.1 mm along the *AB* path, initial debonding occurs, primarily near pre-released area (see Figure 4.9(c)). The debonding process continues until the interface fails at point *B*, leading to tuft pull-out of the laminate during the *BD* path (see Figure 4.9(d)). Once tuft splitting is completed up to point *C*, the tuft begins to be pulled-out by applying lateral force to the interface from the side where the amount of fracture within the interface is greater. Figure 4.9(e) illustrates a substantial volume of the tuft being removed and pulled out from the laminate. This tuft pull-out is accompanied by loading stress in the load-bearing plies, which leads to a local delamination, particularly close to the crack plane.

The failure performance observed in the M-iso laminate (Figure 4.10) is similar to that of the M-ortho specimen, with the dominant failure mechanism being tuft pull-out. Figure 4.10(a) displays the CT scan result of the M-iso laminate in an unloaded condition. Upon stretching the M-iso specimen to 0.025 mm during the *OA* path (Fig. 4.10(b)), no visible deformation is observed in the laminate within the elastic range. However, as the laminate is further stretched up to point *B* along the *AB* path, the tuft starts loading the interface, initiating a debonding failure mechanism along the helical path of the interface, particularly at the top section (Figure 4.10(c)). In Figure 4.10(d), with the debonding progressing in the interface failure between points *B* and *C*, partial tuft pull-out occurs near the top region.

The movement of the tuft inside the quasi-isotropic laminate is more difficult compared to the orthotropic laminate, resulting in the occurrence of cracks within the tuft. These cracks hinder the complete pull-out of the tuft causing portion of the tuft remaining embedded within the laminate during the *CD* path (Figure 4.10(e)), while in the M-ortho laminate (Figure 4.9(e)), the tuft could be almost completely pulled out. The increased extent of tuft pull-out contributes to the improvement of fracture energy, particularly in the M-ortho laminate compared to the M-iso laminate (see Figure 4.3).

64
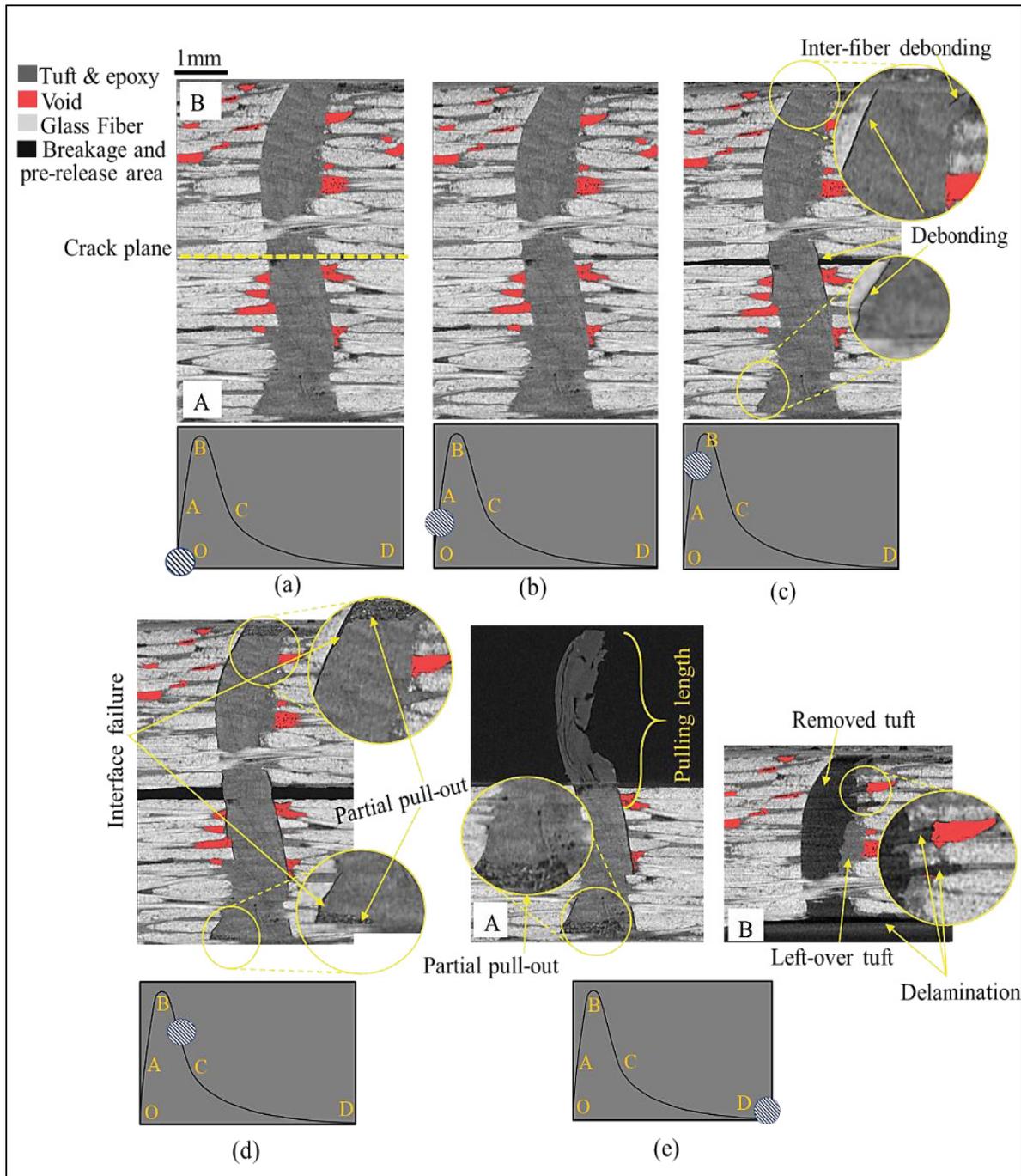
Figure 4.9 CT-scan images of M-ortho at different tensile displacements: (a) zero, (b) 0.025 mm, (c) 0.1 mm, (d) 0.45 mm and (e) 2.8 mm

65
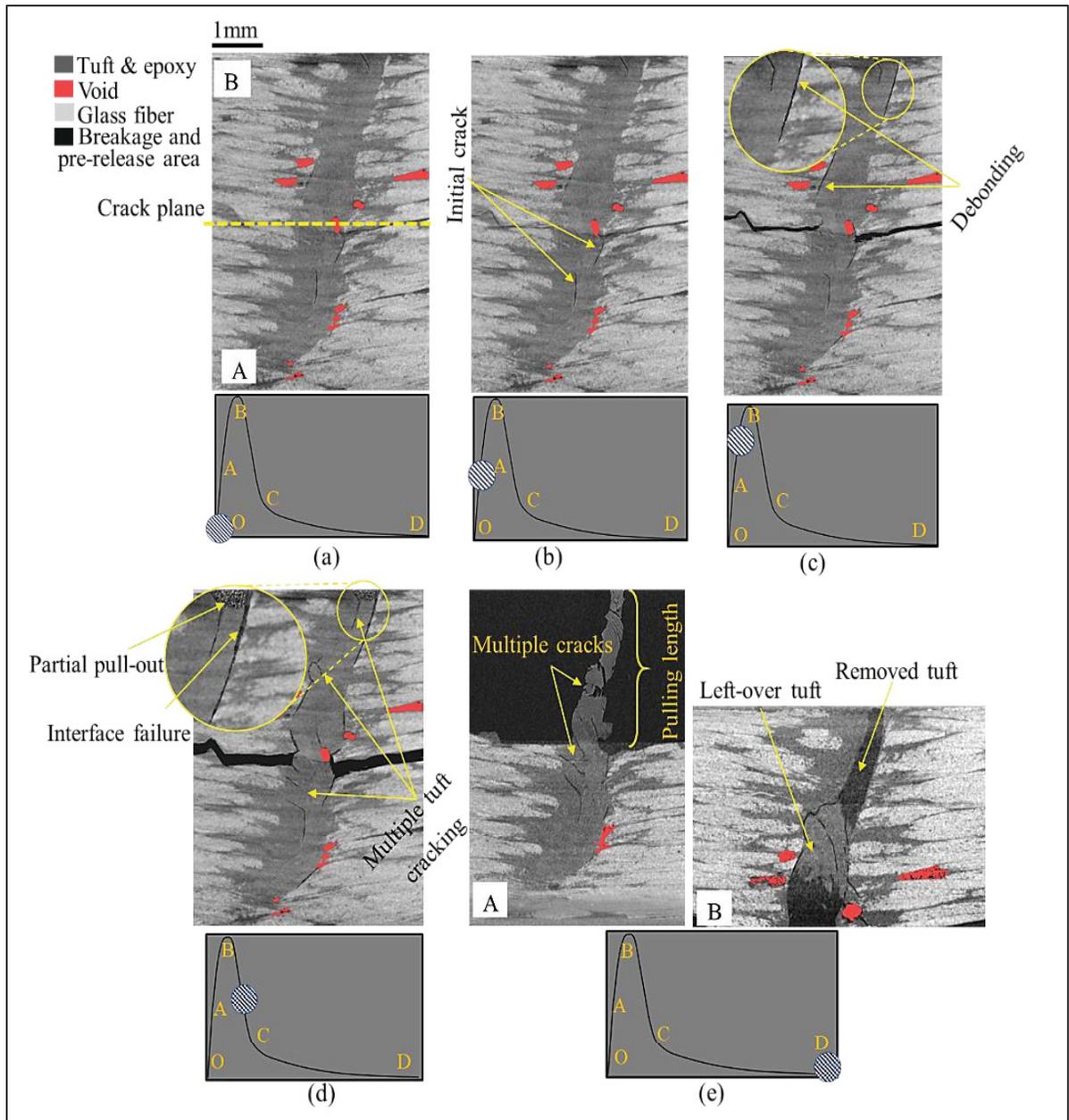
Figure 4.10 CT-scan images of M-iso at different tensile displacement: (a) zero, (b) 0.025 mm, (c) 0.1 mm, (d) 0.4 mm and (e) 2.5 mm

CHAPTER 5

MICRO-MECHANICAL MODELING OF TUFTED COMPOSITES SUBJECTED TO OUT-OF-PLANE LOADING

5.1   Modeling and geometry description

To simulate tufted laminates under traction loading, a novel micro-mechanical model is proposed. The modeling is conducted using Abaqus finite element (FE) software (version 2022). The CT scan images of the laminates, as described in chapter 4 and literature [Pappas et al., 2017; Osmiani et al., 2016], serve as valuable references for accurately defining the dimensions of the simulated parts in the model. Figure 5.1 depicts the various components involved in the modeling of orthotropic tufted laminates. These components include the tuft, the interface, and the composite material. To reduce the processing time, the modeling approach in this study takes advantage of the symmetry plane so only half of the laminate is simulated. Referring to the CT scan observations and investigations conducted by Pappas *et al*. [Pappas et al., 2018], the tuft is composed of two twisted threads with a diameter of 0.48 mm per thread and a length of 3.6 mm. A tiny layer of helical epoxy surrounding the tuft is considered in FE micro modeling which yields external diameters of 0.64 mm within orthotropic laminates. The value is measured by ImageJ software from multiple top view cross-section of the laminates captured at different thickness (see Figures 4.6). The cylindrical and cubic parts of the laminates are simulated with a diameter of 1.6 mm and dimensions of 8 mm × 8 mm, respectively, as illustrated in Figure 5.1. Moreover, Figure 5.1 provides the details of the boundary and loading conditions applied to model. The cross-section of the tuft in the crack-plane remains fixed, while a linear displacement equivalent to the tuft failure displacement is applied to a reference point coupled to the top surfaces of the laminate. To enhance the accuracy of the modeling, a nonlinear geometry analysis is used with maximum time increments of 10^7. All components of the model utilize an 8-node brick element with reduced integration (C3D8R). This choice of element is made to prevent excessive stiffness while also decreasing computation time. A fine mesh is employed for both the tuft and epoxy interface as the zone of interest, with an element size of 0.06mm, to ensure accurate results and

convergence. During the convergence analysis, four element sizes of 0.02, 0.05, 0.06, and 0.08 were tested, and it was observed that results below the 0.06 element size became constant, indicating that further refinement did not significantly affect the outcomes. The composite parts are modeled with larger element sizes ranging from 0.1mm to 0.4mm.
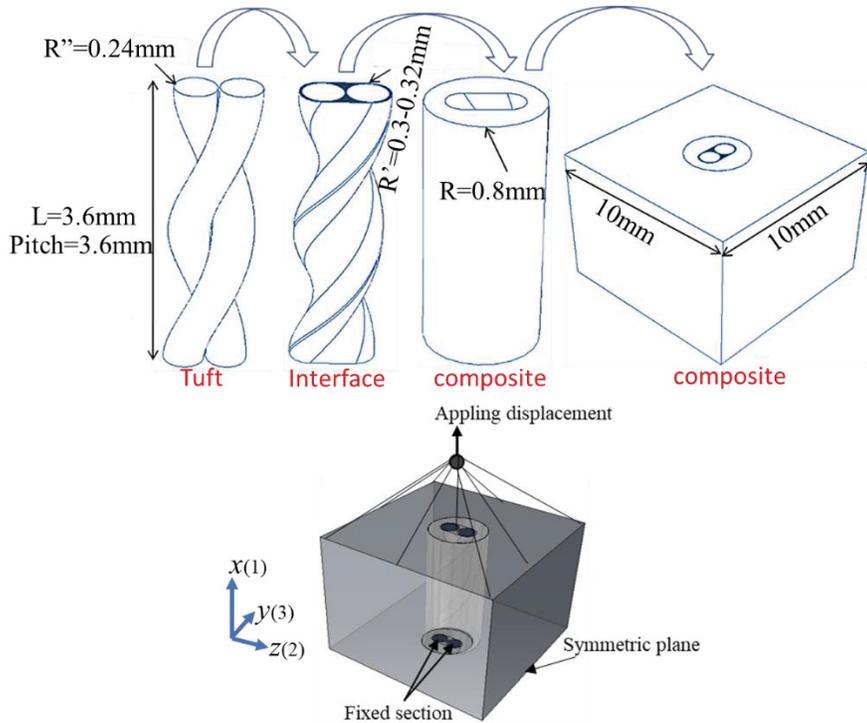
Figure 5.1 Geometry and boundary condition of symmetry tufted laminate

5.2　　Material properties

The mechanical properties of the simulated parts are summarized in Table 5.1 where x indicates the thickness direction. The elastic constants of 0/90 GFRP are obtained by Pappas *et al.* [Pappas et al., 2018] which are the same material used in this study. The fiber volume fraction of a single thread inserted in this laminate is determined to be 21.3%, based on the geometry and the fiber count per thread [Pappas et al., 2017]. Since the tuft consists of two twisted threads, the estimated fiber volume fraction is considered to be 42.5% in this current study. The necessary mechanical properties of a cured tufting thread are determined by employing fiber volume fraction (42.5%), manufacturing data sheets for non-impregnated tuft and resin

[tuft data sheets, 2016; epoxy data sheets, 2016] as long as rule of mixture formula [Isaac & Ori, 1994]. Moreover, the Halpin-Tsai micromechanical semi-empirical correction is utilized to account for the complementary characteristics [Isaac & Ori, 1994]. However, in each tufting thread, there are a pair of twisted yarns positioned at approximately ±8.2 degrees [Pappas et al., 2017; Chan et al., 2019] (as obtained from Chapter 3). The properties of the cured tufting thread at this angle are calculated using the classical laminate theory formula [Isaac & Ori, 1994]. These properties are summarized in Table 5.1 which are assigned to the tuft through material orientation technique tool in the model. The epoxy properties are also outlined in Table 5.1.

Table 5.1 Material properties of model components

GFRP properties								
E_x (GPa)	E_y (GPa)	E_z (GPa)	ν_{xy}	ν_{xz}	ν_{yz}	G_{xy} (GPa)	G_{xz} (GPa)	G_{yz} (GPa)
11.6	24.9	24.9	0.2	0.15	0.12	6.4	6.4	5.5
Tuft properties								
E_x (GPa)	E_y (GPa)	E_z (GPa)	ν_{xy}	ν_{xz}	ν_{yz}	G_{xy} (GPa)	G_{xz} (GPa)	G_{yz} (GPa)
67	5.4	5.4	0.48	0.48	0.41	1.8	2.93	2.93
Matrix properties								
E (GPa)			ν			σ_{yield}		
2.9			0.35			42		
Hashin criteria								
X^T (MPa)	X^C (MPa)	Y^T (MPa)	Y^C (MPa)	Z^T (MPa)	Z^C (MPa)	S ($Sxy=Sxz=S$) (MPa)		
802	400	40	90	40	90	47		
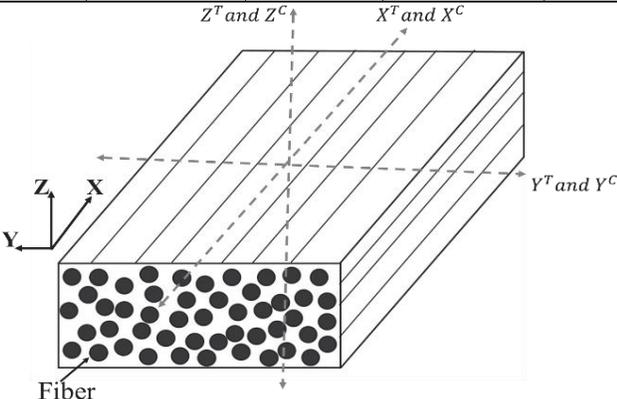
Based on CT scan observations of the laminates, it was found that failure predominantly occurred in the tuft and its surrounding region. As a result, damage properties are applied specifically to the tuft and its interface, while the composite parts (GFRP) experience only elastic deformation. The accurate prediction of damage initiation in tufts, which comprise both carbon fiber and matrix components, relies on the implementation of a composite failure criteria. Several failure criteria have been proposed and developed to predict the initiation of damage in composite laminates, including the maximum stress/strain, Hashin, Hoffman, Tsai-Hill, and Tsai-Wu criteria [Liu et al., 2014]. Among these criteria, the Hashin failure model has been identified as the most suitable for identifying the detailed failure mode in carbon fiber (tuft) within the laminate. Table 5.2 provides a comprehensive summary of the material degradation rules of the tuft based on the full 3D Hashin damage criteria [Liu et al., 2014; Tserpes et al., 2002]. This table outlines the specific parameters and criteria used to determine the damage progression and failure in the tuft. The Hashin failure criterion involves four failure modes: fiber tension (F_f^t), fiber compression (F_f^c), matrix tension (F_m^t), and matrix compression (F_m^c). The parameters X^T and X^C represent the axial tensile and compressive strengths in fiber direction. while Y^T and Z^T correspond to the transverse tensile strength and Y^C and Z^C the transverse compressive strengths (see Table 5.1 for more information). Furthermore, S ($S=Sxy=Sxz$) represents the axial and transverse shear strengths of the tuft/epoxy material. The prefixes 1, 2, and 3 of σ parameter represent the principal direction of unidirectional tuft material, respectively. These coordinate systems follow the helical path of tuft material through material orientation tools in Abaqus. Similarly, σ_{12}, σ_{23}, and σ_{13} represent the shear stresses occurring in specific planes. Noted that, the state variables (SDVs) are numerical instrumental in monitoring and analyzing the failure mechanisms that occur within the tuft itself or matrix in the model employing the Hashin damage criteria as a theoretical framework (see Table 5.2). According to the principle of material degradation using four distinct Hashin failure criteria in Table 5.2, when fiber failure occurs due to both tension and compression, nearly all mechanical properties tend to approach zero [Tserpes et al., 2002]. Because of the epoxy's influence in improving the transverse properties of the composite, the failure of the matrix under tension results in the in-plane Young's modulus (Ey) and Poisson's ratio (vyz) approaching zero [Tserpes et al., 2002]. Additionally, the fiber subjected to tension and compression, as well as

the matrix experiencing tension, display sudden failure characteristics, causing the degradation of the material to occur rapidly. Due to the matrix's progressive failure under compression and its tendency to exhibit some shear characteristics [Fiedler et al., 2001], the failure indices for compression and shear become intertwined, as detailed in Table 5.2. Consequently, within this particular failure index, the in-plane and shear aspects of mechanical properties degrade toward zero, driven by decreased coefficient values outlined in Table 5.2.

Table 5.2 3D Hashin-type failure criteria and material property degradation rules for tuft

Failure mode	Failure criteria	Material property degradation rule
Fiber tension and compression failure	$\text{SDV2} = F_f^t = \left(\frac{\sigma_1}{X^T}\right)^2, F_f^c = \left(\frac{\sigma_1}{X^C}\right)^2$	*Ex=0.0001Ex, Ey=0.0001Ey, Ez=0.0001Ez, vxy=0.0001vxy, vxz=0.0001vxz, vyz=0.0001vyz, Gxy=0.0001Gxy, Gxz=0.0001Gxz, Gyz=0.0001Gyz,*
Matrix tension failure	$\text{SDV3}=F_m^t = \left(\frac{\sigma_2+\sigma_3}{Y^T}\right)^2$ $+ \frac{\sigma_{12}^2 + \sigma_{13}^2 + \sigma_{23}^2 - \sigma_2\sigma_3}{S^2}$	*Ey=0.0001Ey, vyz=0.0001vyz*
Matrix compression and shear Progressive failure	$\text{SDV4} = F_m^c = \frac{1}{Y^C}\left[\left(\frac{Y^C}{2S}\right)^2 - 1\right](\sigma_2 + \sigma_3) + \left(\frac{\sigma_2+\sigma_3}{2S}\right)^2 + \frac{1}{S^2}(\sigma_{23}^2 - \sigma_2\sigma_3) + \frac{1}{S^2}(\sigma_{12}^2 + \sigma_{13}^2)$	*Ey, Ez, Gxy, Gxz, Gyz* are degraded progressively by reduced coefficients listed below 0.94,0.77,0.70,0.64,0.580.532,0.48 ,0.43,0.39,0.36,0.33,0.30,0.27,0.24 ,0.22,0.20,0.18,0.16,0.15,0.14,0.12 ,0.11,0.10,0.09,0.08,0.0009,

Additionally, the epoxy interface is modeled using an elastoplastic material property, incorporating plastic strain-stress values outlined in Table 5.3 [Fiedler et al., 2001; Pappas et al., 2017]. These values define the behavior of the epoxy interface under plastic deformation, allowing for a more realistic representation of its mechanical response. To facilitate the simulation process, the user-defined field (USDFLD) subroutine is employed. This subroutine enables the user to define and incorporate customized damage variables as functions for the tuft part [Zhou et al., 2021; Wang et al., 2013]. Figure 5.2 provides an illustration of the

functionality and operation of the USDFLD routine within this simulation. This visual representation aids in understanding the working principles and processes involved.

Table 5.3 Yield stress-strain data for matrix [Fiedler et al., 2001; Pappas et al., 2017]

| Stress level (σ_y)	Plastic strain(ε)
39	0
40	0.005
38	0.0078
26	0.018
12.5	0.027
7	0.04
0.3	0.3
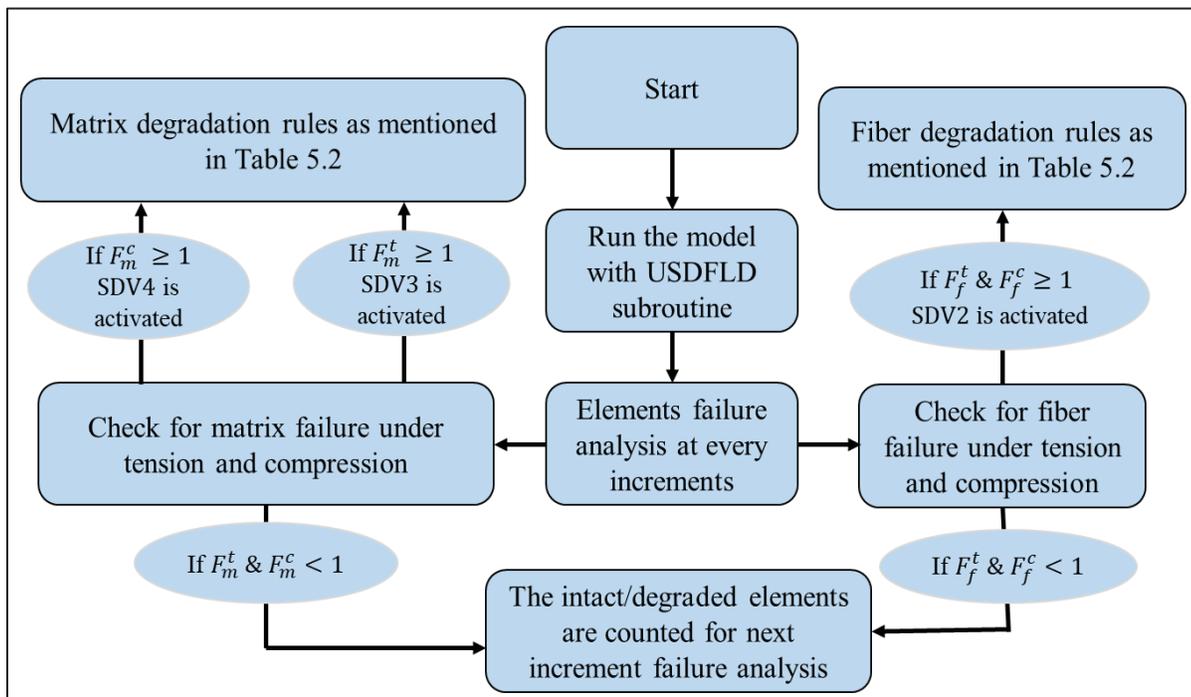
Figure 5.2 Flowchart of the USDFLD

5.3 Simulation results and discussion

Figure 5.3 presents the response of orthotropic tufted laminates in terms of force-displacement curve, comparing it to experimental error band results. The utilization of the USDFLD and

elastoplastic damage criteria for the tuft and interface, are respectively employed in FEM nonlinear geometry simulation. This modeling approach aims to predict the failure mechanism within the laminate when subjected to tensile loading. The model reaches a point where the incremental time step becomes approximately constant around 105N, preventing it from advancing further and representing the rest of the *AB* route. The Finite Element results exhibit a favorable agreement with the experimental data, with a slightly stiffer behavior. This can be attributed to the absence of void modeling in the current simulated parts, as observed in the CT-scan observations. The voids present in the actual material can contribute to a softer response, resulting in a deviation from the simulated stiffness.
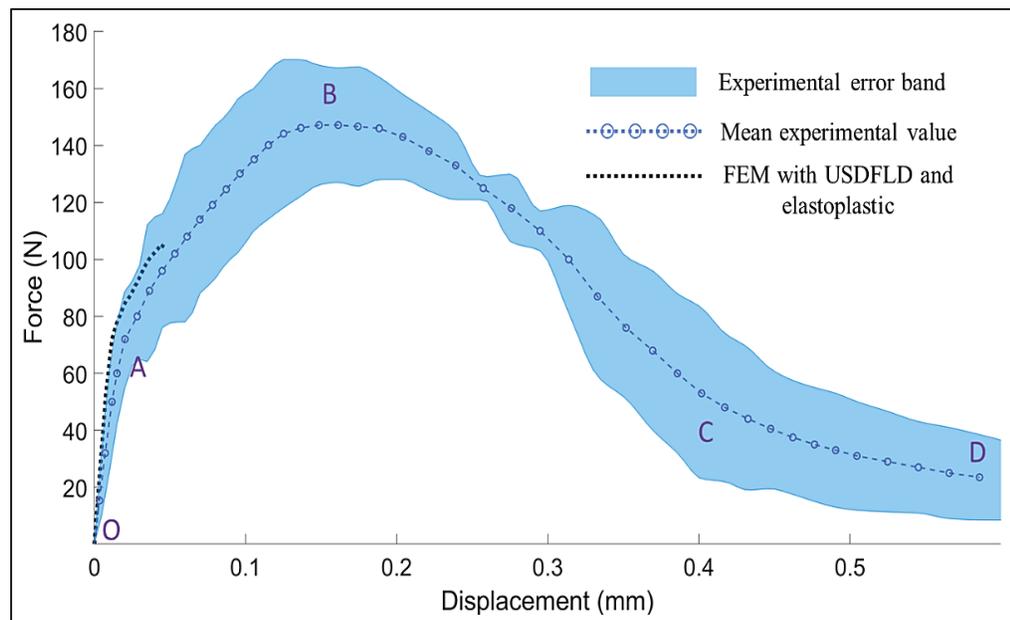
Figure 5.3 FE and experimental force-displacement response comparison utilizing damage criteria for both tuft and tuft interface

The dominant failure mechanism within the laminate up to a load of 110N is depicted in Figure 5.4, showing the damage distribution within the interface. As depicted in this figure, the FEM model does not report any failure within the interface during first slope up to 60N. This finding is further supported by CT-scan observations conducted under the elastic mode during *OA* path of force-displacement respond (see figure 4.2 in chapter 4). The plastic strain (PE) is activated at around 60N within the interface showing that the initial change in slope is primarily due to

the failure of the interface in close proximity to the pre-crack layer. This result is further confirmed by CT-scan images, which provide clear evidence of initial debonding within the interface of the tufted laminates during elastic regime (see figure 4.4 in chapter 4). Furthermore, as the tension amount is increased, the damages occurring within the interface advance from the mid-plane towards upward. (see Figure 5.4). As previously mentioned in Table 5.2, the impregnated tuft damages are influenced by three different state variables (*SDV*) as specified by the Hashin failure criteria utilized in the USDFLD (see Figure 5.2 For more comprehensive information). As depicted in Figure 5.5, the state variable 2 (*SDV*2) represents the fiber failure under both tension and compression. On the other hand, *SDV*3 and *SDV*4 correspond to the matrix failure criteria under tension and compression, respectively. The results presented in Figure 5.5 demonstrate that *SDV*3 and *SDV*4 are primarily triggered at mid-plane region. Additionally, *SDV*2 is activated as a result of the fiber itself experiencing failure. This correlation between the FEM results and the visual evidence from the CT-scan images confirms that the tuft failure corresponds to the actual inter-fiber debonding as the small cracks which were not obvious to detect by CT-scan. Hence, the few numbers of elements triggered by *SDVs* in the model within the tuft indicates that the failure is more crack-like rather than a complete and abrupt failure.
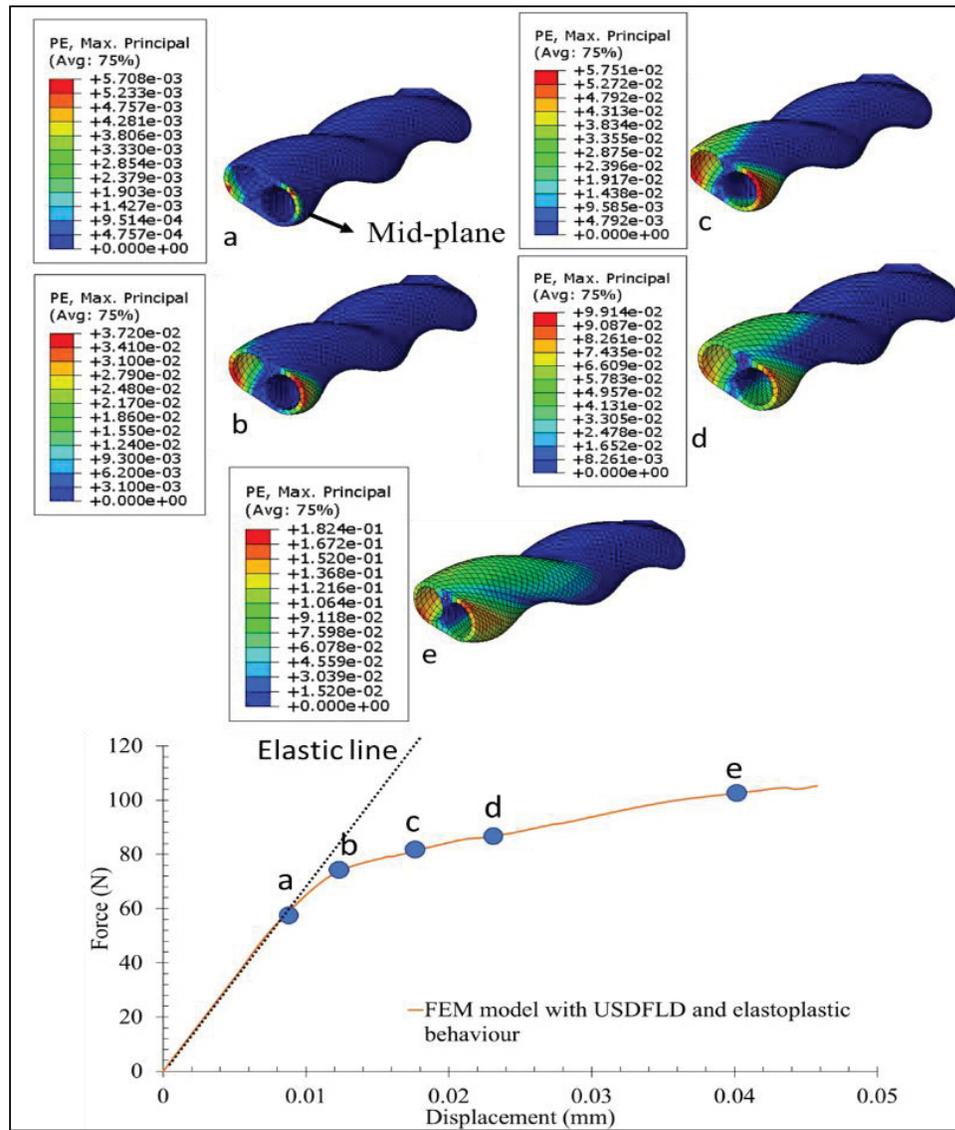
Figure 5.4 Numerical damage distribution within interface part utilizing damage criteria for both tuft and tuft interface
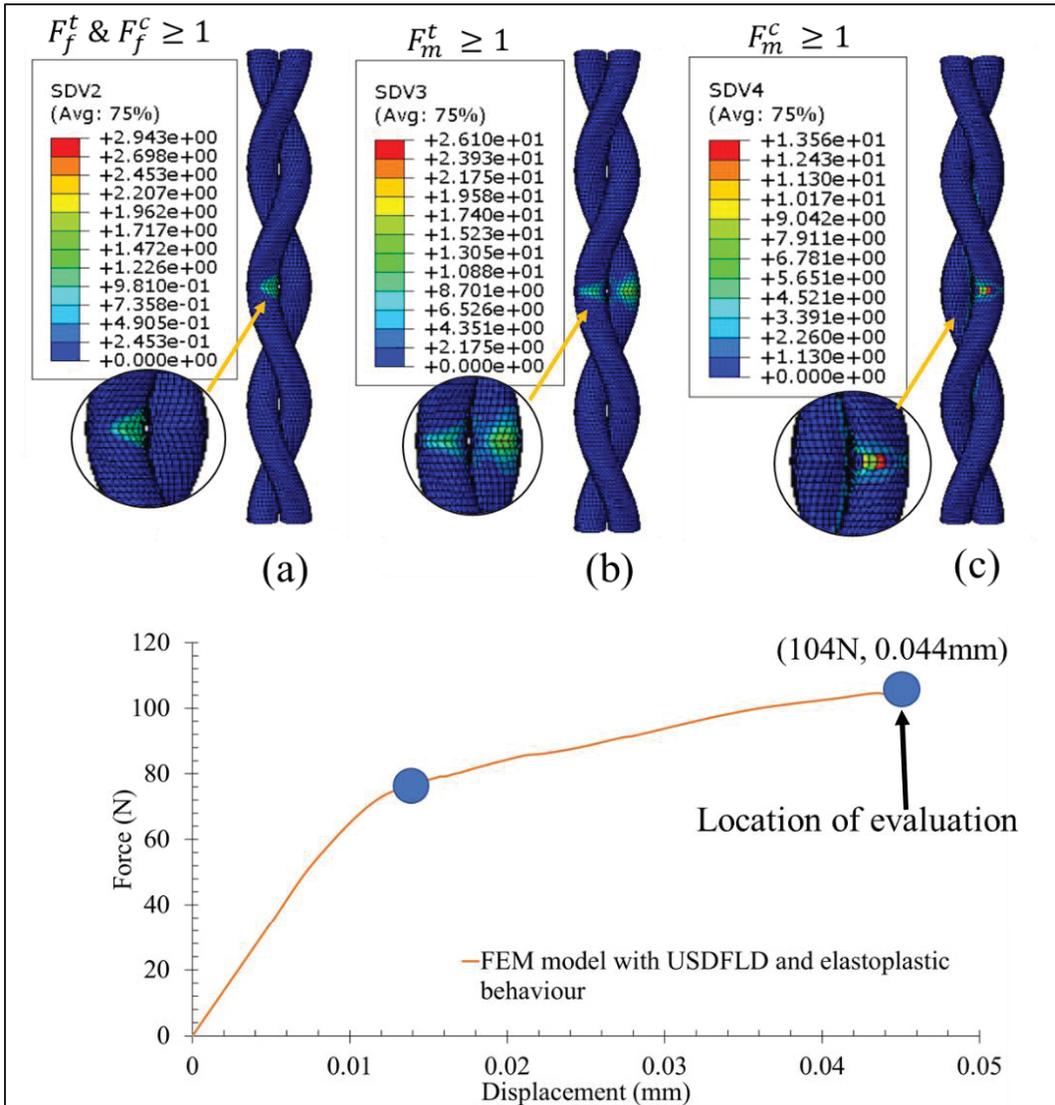
Figure 5.5 Numerical damage distribution within the tuft: (a) for tuft itself under tension and compression, (b) for matrix under tension and (c) compression

To overcome the limitations of the existing model, a revised modeling approach has been adopted. In this updated model, the use progressive damage for the tuft material has been eliminated and only plasticity simulation at the interface is kept. This adjustment is expected to enable the model to approximate the force-displacement response, up to point B. Figure 5.6 presents the comparison between the FEM force-displacement results and the experimental data up to point B. When comparing the two proposed models, one utilizing both USDFLD and elastoplastic techniques, and the other employing only the elastoplastic technique, it

becomes evident that the force-separation curve exhibits slightly greater stiffness in the model with only elastoplastic implemented. This is attributed to the progressive failure occurring the tuft material.
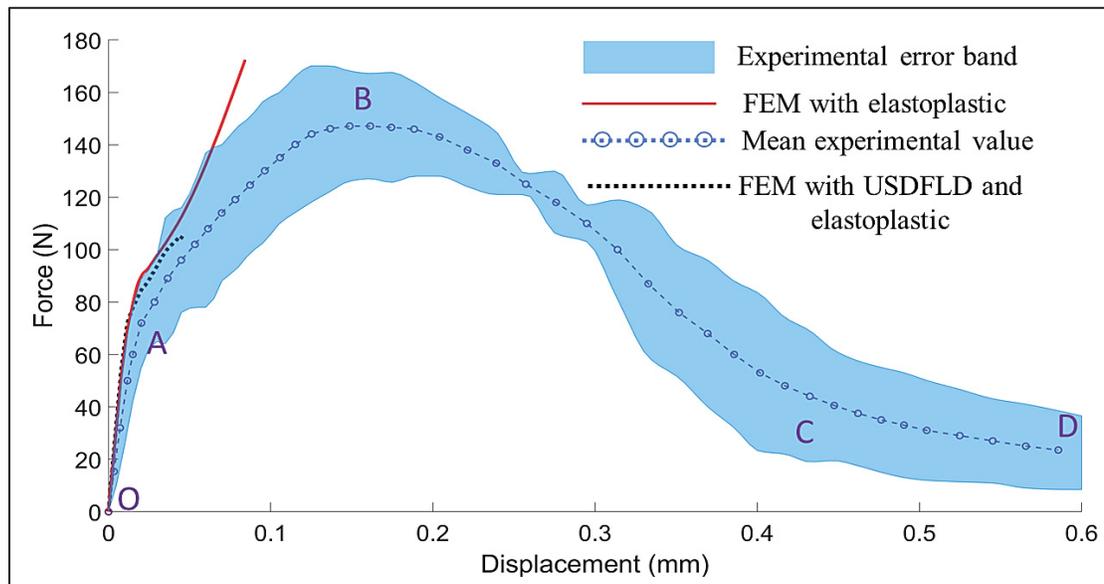
Figure 5.6 FE and experimental force-displacement response comparison, utilizing damage criteria for tuft interface

Figure 5.7 and 5.8 present the distribution of damage and stress levels within the interface and tuft regions. During the transition from the OA to AB slope, the interface undergoes the initiation of damage propagation, which begins from the mid-plane and progresses upwards. Hence, as the tufted laminate approach point B, the amount of plastic strain within the interface expanded (see Figure 5.7). Figure 5.8 illustrates the stress level component, specifically S_{11} (stress under tension), within the tuft material. This stress component reaches the ultimate strength of 802 MPa, as indicated between points A and B on the force-displacement curve. The number of elements present in the mid-plane, where the stress component S_{11} reaches 802 MPa, is not sufficient to cause complete failure of the tuft material. This behavior is observed as a small staircase-like pattern in the experimental force-displacement curve discussed in chapter 4.
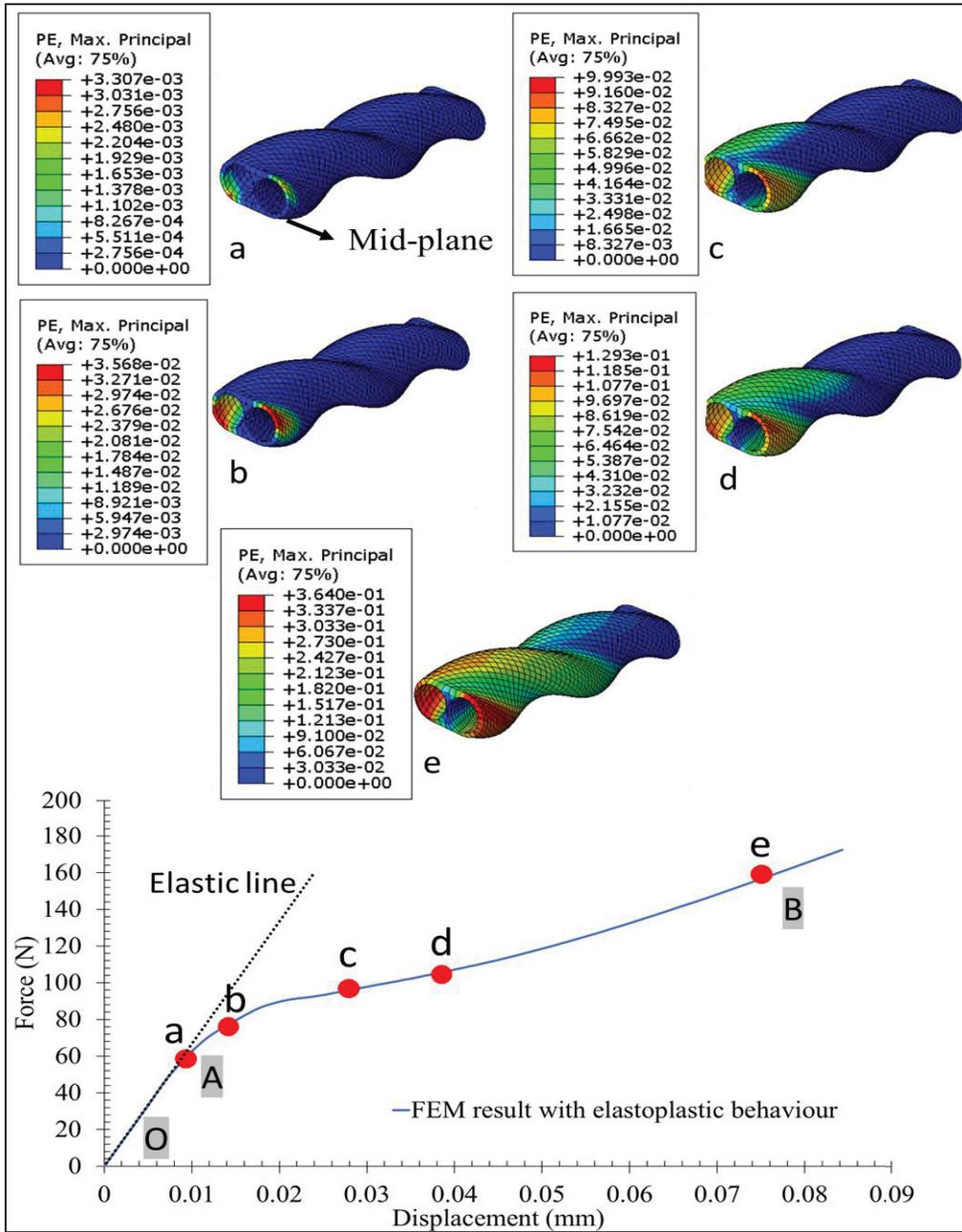
Figure 5.7 Numerical damage distribution within interface when the damage criteria is considered for the tuft interface

Figure 5.8 depicts the presence of three distinct stress zones within the tuft, characterized as failure, approaching failure, and no failure. These zones are determined based on the stress levels of the S_{11} component. At a load level of 160 N, a portion of tuft elements are expected

to fail with high stress concentrations between 802MPa and 1660MPa near the mid-plane region (gray color). This high-stress region leads to the failure of the tuft within the pre-crack layer, accompanied by a relatively small tuft pulling out, as observed in the experimental outcomes. Additionally, the distribution of the S_{11} stress component highlights that contact elements between the two threads poses a higher risk of damage within the tuft with stress level between 480MPa and 802MPa (blue color).
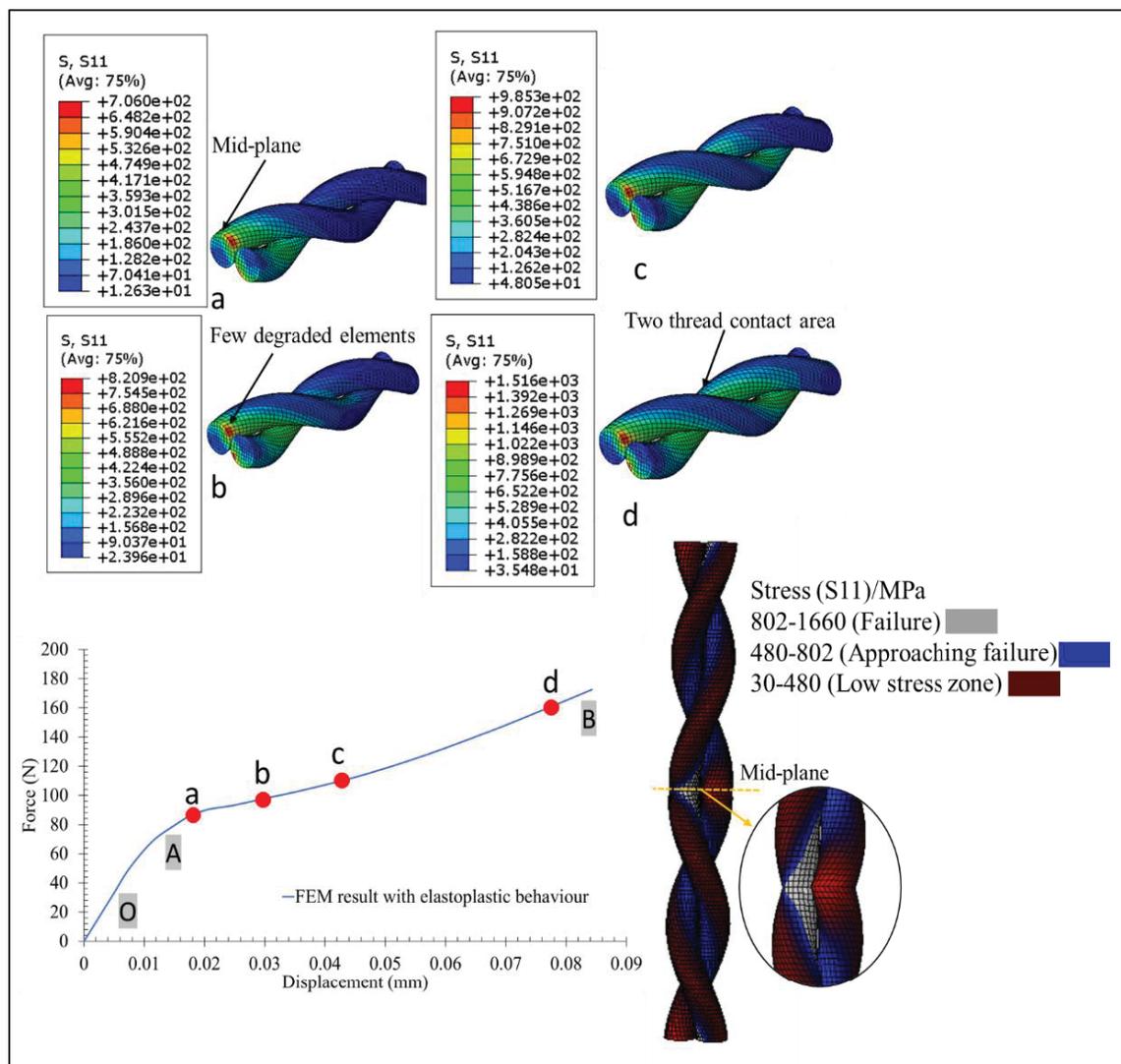

Figure 5.8 Numerical S_{11} stress component distribution within the tuft when the damage criteria is considered for the tuft interface

CONCLUSION

The aim of this study is to investigate how tufting geometry and laminate sequences impact the failure mechanisms in tufted layered woven GFRP composites, considering the presence of a full-length release film at the mid-plane isolate tuft contribution under tension. CT scans are utilized to analyze the failure mechanisms that occur during the tension of the tufted laminates. A micro-scale modeling framework is introduced to predict the failure mechanisms within a single Tuft, and its accuracy is verified using experimental results. Based on findings presented in this study, several conclusions can be drawn.

- The use of loop-less geometry, achieved by milling down the laminates, has shown to enhance fracture toughness. This is attributed to the elimination of loops, which promotes tuft pull-out and facilitates the development of large plastic zones in the force-separation curves of tufts. The results reported a 1.15 to 1.5-fold increase in tensile ultimate strength for tufted laminates with loops compared to loop-less ones, particularly for orthotropic and quasi-isotropic laminate types. The findings presented in this study offer valuable additional insights that complement previous research in this field [Pappas et al., 2017].

- The change in laminate sequences from orthotropic laminates, which consist of consecutive layers of 0/90 layup, to quasi-isotropic laminates with consecutive layers of 0/90 and ±45 preforms has notable effects. Depending on the specific tufting geometry, quasi-isotropic laminates can exhibit a 16% to 34% higher tensile strength compared to orthotropic laminates. Moreover, the fracture energy of tufted orthotropic laminates in which the tuft pull-out is visible on fractured surface is 62% higher than the tufted quasi-iso one. Regardless of the tufting geometry, this result can be attributed to the fact that the epoxy thickness around the tufts in quasi-isotropic laminates is thinner compared to those in orthotropic laminates, resulting in smaller tuft pull-out behavior as opposed to larger tuft pull-out observed in orthotropic laminates. CT scan analysis is used to investigate various failure mechanisms within the tufted laminates by subjecting them to incremental tensile displacements. In the linear tensile regime, the primary failure mechanisms observed are interface debonding and

inter-fiber debonding. Interestingly, the microstructural failure analysis reveals that the failure mechanism within the elastic region remains relatively unchanged, regardless of the laminate type or tufting geometry. In the nonlinear regime, different failure mechanisms occur in the laminates depending on the laminate type and tufting geometry. The primary failure mechanisms encountered include interface failure, tuft rupture, and tuft pulling out. Notably, in loop-less specimens, there is a higher occurrence of tuft splitting at the laminate surface level. This can be attributed to the shear force exerted by the loop-less tuft on the interface, facilitating its pulling out from the free surfaces where there is no loop holding force. On the other hand, with-loop laminates experience more rupture in the middle area of the tuft, accompanied by small-scale tuft pulling out. Moreover, the amount of resin surrounding the tuft significantly influences the tuft failure mechanism when the laminate sequences are changed. In cases where there is a small amount of resin and the tuft is in close contact with the quasi-isotropic laminate, tuft failure at the mid-plane is observed. Conversely, the large amount of resin around the tuft observed in orthotropic laminates promotes fiber pull-out and fracture energy compared to quasi-isotropic ones.

- The second part of this study presents a comprehensive analysis of failure mechanisms using a micro modeling designed to predict the failure of a single TTR (Through-Thickness Reinforcement) laminate under tension. The Hashin damage criteria for the tuft, as well as the elastoplastic response of the tuft interface, are integrated into the modeling process using Abaqus plasticity tools and the user-defined field (USDFLD) method. Although convergence issue did not let the non-linear analysis progress until full failure, the model successfully predicts the experimental failure mechanisms observed in orthotropic tufted laminates in the early stage of tensile test.

APPENDIX I

ARTICLES PUBLISHED IN CONFERENCES

We have presented the main content of this thesis in a conference paper.

"The effect of laminate sequences on tuft bridging in GFRP laminates under tensile loading" which has been accepted in IOP Conference Series: Materials Science and Engineering, Volume 1266, 8th International Conference on Intelligent Textiles & Mass Customisation (ITMC) 18/09/2022 - 21/09/2022 Montreal, Canada

LIST OF REFERENCES

Advanced Materials Huntsman International LLC. (2016). Araldite LY 8615/Aradur 8615/Hardener XB 5173. Technical datasheet. [Online]. http://samaro.fr.

Ansar, M., Xinwei, W., & Chouwei, Z. (2011). Modeling strategies of 3D woven composites. *Composite structures, 93*(8), 1947–1963.

Aymerich. F., Priolo, P., & Sun, C.T. (2003). Static and fatigue behavior of stitched graphite/epoxy composite laminates. *Composite Science and Technology, 63*(6), 907–917.

Bigaud, J. (2016). *Analyse du comportement mécanique de structures composites renforcées par coutures.* (P.h.D Thésis, Université de Technologie de Compiègne).

Bilisik, A. K. (2012). Multi axis three-dimensional woven fabric: a review. *Textile Research Journal,* 82 (7), 725-743

Cartié, D. D. R., Troulis, M., & Partridge, I.K. (2006). Delamination of Z-pinned carbon fiber reinforced laminates. *Composites Science and Technology, 66*, 855-861.

Chan, H., Peng, W. & Xavier, L. (2019). Improvement of tufting mechanism during the advanced 3-dimensional tufted composites manufacturing: To the optimisation of tufting threads degradation, Composite Structures, 220, 423-430.

Chen, X., Taylor, L.W., & Tsai, L.J. (2011). An overview on fabrication of three-dimensional woven textile preforms for composites. *Textile Research Journal*, *81*, 932-944.

Colin, M., Pickett, A. K., Skordos, A.A., & Witzel, V. (2009). Evaluation of the mechanical and damage behaviour of tufted non-crimped fabric composites using full field measurements. *Composite Science and Technology*, *69*(2), 131-138.

Dell'Anno, G., Treiber, J. W. G., & Partridge, I. K. (2016). Manufacturing of composite parts reinforced through-thickness by tufting. *Journal of Robotics and Computer-Integrated Manufacturing, 37*, 262-272.

Dransfield. K., Baillie. C., & Mai, Y. W. (1994). Improving the delamination resistance of CFRP by stitching -a review. *Composite Science and Technology, 50*(3), 305-317.

Fiedler, B., Hojo, M., Ochiai, S., Schulte, K. & Ando, M. (2001). Failure behavior of an epoxy matrix under different kinds of static loading. *Composites Science and Technology, 61*, 1615–1624

Gnaba I., Legrand X., Wang P., & Soulat, D. (2017). Literature review of tufted reinforcement for composite structures. *17th World Textile Conference AUTEX 2017- Textiles - Shaping the Future, 254* (4).

Henao, A., Guzmán, R., Cuartero, J., Carrera, M., Picón, Juan., & Miravete, A. (2014). Enhanced impact energy absorption characteristics of sandwich composites through tufting. *Mechanics of Advanced Materials and Structures, 22, 1016-1023.*

Hui, C., Wang, P. & Legrand, X. (2019). Improvement of tufting mechanism during the advanced 3-dimensional tufted composites manufacturing: To the optimization of tufting threads degradation. Composite Structures, *220*, 423–430.

Isaac, D., & Ori, l. (1994). *Engineering Mechanics of Composite Materials*. Oxford University Press: New York.

Karuppannan, D., Sivaraman, V., Kotresh, M., Ramesh, S., & Ajith, R. (2012). Effect of tufting on mechanical properties of laminated composites. *ISAMPE National Conference on composite Materials*, pp. 2–3.

Lascoup, B., Aboura, Z., Khellil, K., & Benzeggagh, M., (2010). Impact response of three-dimensional stitched sandwich composite, *Composite Structure, 92*, 347–353.

Lascoup, B., Aboura, Z., Khellil, K., & Benzeggagh, M. (2006). On the mechanical effect of stitch addition in sandwich panel. *Composites Science and Technology*, *66*, 1385–1398.

Liu, P. F., Xing, L.J. & Zheng, J. Y. (2014). Failure analysis of carbon fiber/epoxy composite cylindrical laminates using explicit finite element method. *Composites: Part B, 56*, 54–61

Mouritz, A.P. (2007). Review of Z-pinned composite laminates. *Composites Part A: Applied Science and Manufacturing*, *38*, 2383–2397.

Mouritz, A. P., & Cox B. N. (2010). A mechanistic interpretation of the comparative in-plane mechanical properties of 3D woven, stitched and pinned composites *Journal of Composites Part A: Applied Science and Manufacturing, 41*(6), 709-728.

Mouritz1, A. P., Chang, P., & Isa, M. D. (2011). Z-pin composites: aerospace structural design considerations. *Journal of Aerospace Engineering, 24* (4).

Meo, M., Achard, F., & Grassi, M. (2005). Finite element modelling of bridging micro-mechanics in through-thickness reinforced composite laminates. *Composite Structures*, *71*, 383–387.

Osmiani, C., Mohamed, G., Treiber, J. W. G., Allegri, G., & Partridge I.K. (2016). Exploring the influence of micro-structure on the mechanical properties and crack bridging

mechanisms of fibrous tufts. *Composites Part A: Applied Science and Manufacturing*, *91*,409-419.

Pappas, G., Joncas, S., Michaud, V., & Botsis, J. (2017). The influence of through-thickness reinforcement geometry and pattern on delamination of fiber-reinforced composites: Part II – Modeling. *Composite Structures, 181*, 379–390.

Pappas, G., Joncas, S., Michaud, V., & Botsis, J. (2018). The influence of through-thickness reinforcement geometry and pattern on delamination of fiber-reinforced composites: Part I – Experimental results. *Composite Structure, 184*, 924–934.

Plain, K. P., & Tong. L. (2010). The effect of stitch incline angle on mode I fracture toughness – Experimental and modelling Composites Science and Technology. *Composite Structures, 92*, 1620–1630.

Samlal, S., Paulson V., & Santhanakrishnan, R. (2015). Effect of stitching angle on impact characteristics of sandwich panels. *International Journal of Innovative Science Engineering and Technology, 12*(4), 30–34.

Soung Van, H. (2009). *Handbook principles of the manufacturing of composite materials*. United States: DEStech Publications.

Toho Tenax. (2016). Delivery programme for Tenax filament yarn. Technical datasheet. [Online]. http://www.tohotenax.com/products/tenax-carbon-fiber/.

Tong, L., Mouritz, A. P., & Bannister, M. K. (2002). *Handbook on the 3D fiber reinforced polymer composites* (1th ed). Boston, US: Elsevier Science.

Treiber, J. W. G., Cartié, D. D. R., & Partridge, I. K. (2009). Determination of crack bridging laws in tufted composites.

Treiber J., Cartié D. D. R., & Partridge, I. K. (2011). Effects of meso structure on the in-plane properties of tufted carbon fabric composites. *5th International Conference on Composites Testing and Model Simulation*, pp. 2–4

Tserpes, K. I., Labeas, G., Papanikos, P. & Kermanidis, T. (2002). Strength prediction of bolted joints in graphite/epoxy composite laminates. *Composites: Part B*, *33*, 521–529.

Wang, X., Zhang, J., Wang, Z, Liang, W. & Zhou, L. (2013). Finite element simulation of the failure process of single fiber composites considering interface properties. *Composites: Part B, 45*, 573–580

Yudhanto, A., Lubineau, G., Ventura, I. A., Watanabe, N., Iwahori, Y., & Hoshi, H. (2015). Damage characteristics in 3D stitched composites with various stitch parameters under

in-plane tension. *Journal of Composites Part A: Applied Science and Manufacturing*, *71*, 17–31.

Zhou, Y., Xiao, Y., Wu, Q. & Xue, Y. (2021). A multi-state progressive cohesive law for the prediction of unstable propagation and arrest of Mode-I delamination cracks in composite laminates. *Engineering Fracture Mechanics, 248*,1.